Improving analytical utility of Surface Enhanced Raman Spectroscopy through unique lithographic substrate development

A Thesis Presented for the
Doctor of Philosophy Degree
The University of Tennessee, Knoxville

Sabrina Marie Wells
May, 2012

To the instructors, teachers, and mentors who helped foster my
passion for science, discovery, and learning.

Thank you.

Acknowledgements

First, I would like to thank Dr. Sepaniak for giving me the opportunity to join his group several years ago. I have learned so much more about being a researcher, working through problems, and the importance of loving what you do by being a member of this group and seeing how he conducted himself daily. I would also like to thank the other members of the lab, both past and present. This particularly goes to Kasey Hill for her assistance at work and conversations about bad TV and movies out, Deepak Bhandari for his patience and ability to explain concepts so that even I could understand, and Lisa Taylor for our noncompetitive competition that helped push me to become a stronger and more confident researcher.

I would also like to thank Oak Ridge National Lab, particularly CNMS, for allowing me to work out there for the last four years. I have learned so much from every person I worked with out there and it was a pleasure to be invited into the fold with open arms. During my time there, I predominately worked with Scott Retterer, who showed me the ropes and started me in the right direction, and Nickolay Lavrik, who continued to add thoughtful ideas and technical insight for my work. I would not be here without their support.

Finally, I want to thank my family for their support through these past years. I would not have made it this far without my parents, Robin and Barry, who continue to tell me I can do anything. Thanks to Whitney and my “little brother” Jake for all the love and the occasional ear to vent into. Also, I need to thank Roy for always making me smile when I walk in the door, no matter how hard the day was until then. I could not have persevered on without all of your help and love.

Abstract

Surface enhanced Raman spectroscopy (SERS) has the potential to be a useful analytical technique due to large signal enhancements. Unfortunately, SERS has several drawbacks, including a lack of reproducibility, which inhibits it from being a practical option. These large signals often arise from “hot spots” of extremely high enhancement on nanofeatured metallic substrates, the most common being comprised of aggregated silver colloid. It is difficult to reproducibly create these hot spots due to the randomness of the colloid substrates. However, through controlled substrate fabrication, many problems associated with SERS analysis can be overcome. Electron beam lithography (EBL) combined with reactive-ion etching (RIE) was used to fabricate a wide variety of aggregate-like structures that allow for methodically surveying the system to determine if areas of high enhancement are present. Any well performing areas were then recreated consistently to produce areas of similar enhancement.

While the aforementioned “combinatorial” approach has its advantages, simple structures are often easier to fabricate and theoretically model. As such, a single structure consisting of a metal disc on a silicon pillar was created. A variety of tests were performed on these structures to determine the overall utility of the simple pillar system. The system was found to possess extremely high enhancement, making it an ideal system to both theoretically model and test experimentally. The system also has strong enough overall signal to allow for potential analytical implications.

Studies were also conducted to determine the feasibility of using a strong enhancing silicon nanopillar system to make analytical measurements without a metal surface present. A special fabrication process using EBL and RIE was used to created tall, high aspect ratio pillars of known diameters. These nanopillars were then observed to exhibit special optical properties not seen in bulk silicon. Aside from modest Raman enhancement, these structures also demonstrated the ability to enhance the signal of specific analytes similar to SERS. Surface enhanced fluorescence (SEF) was also observed for different analytes, allowing for a variety of potential analytical areas.

Table of Contents

List of Tables

Table Page

List of Figures

Nomenclature

μ	Induced Dipole
α	Polarizability
α_0	Equilibrium Polarizability
E	Initial Energy
E'	Final Energy
E_0	Amplitude of Electromagnetic Wave
$\varepsilon_1(\omega)$	Frequency Dependent Dielectric Function
ε_2	Relative Permittivity of Ambient Environment
I_{surf}	Signal Area for SERS
I_{vol}	Signal Area for Neat Analyte
ν	Incident Frequency
ν'	Scattered Frequency

$\nu+\nu_\varphi$	Antistokes Frequency
ν_φ	Vibrational Frequency
$\nu-\nu_\varphi$	Stokes Frequency
N_{surf}	Surface Number Density
N_{vol}	Number Density
r	Bond Length at Given Time
r_{eq}	Bond Length at Equilibrium
r_{max}	Maximum Distance of Separation
APTES	Aminopropyltriethoxysilane
BT	Benzenethiol
CCD	Charge Coupled Device
CCP	Capacitively Coupled Plasma
CE	Chemical Enhancement
CT	Charge-Transfer
DOP	Disc on Pillar

EBL	Electron Beam Lithography
EF	Enhancement Factor
EM	Electromagnetic
FDTD	Finite Difference Time Domain
FIB	Focused Ion Beam
FITC	Fluorescein Isothiocyanate
FON	Film Over Nanosphere
HOMO	Highest Occupied Molecular Orbital
ICP	Inductively Coupled Plasma
IR	Infrared
LB	Lagnmuir Blodgett
LDNAs	Lithographic Defined Nanoaggregates
LFIEF	Local Field Intensity Enhancement Factor
LMIS	Liquid-Metal Ion Source
LSPR	Localized Surface Plasmon Resonance

LUMO	Lowest Unoccupied Molecular Orbital
MIT	Mitoxantrone
NHA	Nanohole Array
NSL	Nanosphere Lithography
PDMS	Poly(dimethylsiloxane)
PECVD	Plasma Enhanced Chemical Vapor Deposition
PML	Perfectly Matching Layer
PVD	Physical Vapor Deposition
QCM	Quartz-crystal Microbalance
R6G	Rhodamine 6G
RIE	Reactive Ion Etching
RSD	Relative Standard Deviation
SAM	Self-assembled Monolayer
SEF	Surface Enhanced Fluorescence
SEM	Scanning Electron Microscopy

SERRS	Surface Enhanced Resonance Raman scattering
SERS	Surface Enhanced Raman Spectroscopy
SMSERS	Single Molecule SERS
STT	Sample Translation Technique
TEM	Transmission Electron Microscopy
VLS	Vapor-Liquid-Solid

Chapter 1

Introduction

This dissertation is concerned with improving the analytical application and use of surface enhanced Raman spectroscopy (SERS) substrates through rational design. Through continued development using lithographic methods, insight into how to create quality analytical SERS substrates was obtained. Current work also focuses on creating structures with enhanced Raman capabilities without the need for a metallic surface and understanding how this phenomena works.

The structure for this dissertation is ordered so that a brief overview of the Raman effect and SERS mechanisms are provided (Chapter 1). Chapter 2 follows with a discussion of various SERS substrates and the techniques used to create them, with electron beam lithography (EBL) and reactive ion etching (RIE) comprising a large focus. A combinatorial-like approach to lithographic SERS substrate development and analytical studies are looked at in Chapter 3. Based on the information garnered in the previous chapter, disc on pillar substrates are then analyzed for analytical utility (Chapter 4). Subsequent research focuses on using silicon nanopillar structures for use with various informative techniques (Chapter 5). Chapters 3-5 are presented as publications from my dissertation work.

The focus of this chapter is to provide a brief introduction to Raman spectroscopy. Moreover, it introduces basic SERS theory and mechanisms while also providing insight into current analytical prospects for the technique.

1.1 Brief introduction to Raman spectroscopy

1.1.1 The Raman effect

Raman spectroscopy, as it is known today, is a valuable, highly selective technique used in the determination of structural information from analyte molecules. This method of characterization can yield narrow, well-resolved vibrational bands which, in essence, provide a “fingerprint” of a given analyte and involve surface processes and interfacial reactions [1, 2]. The method was first theoretically predicted and described in 1923 by A. Smekal [3] and later experimentally observed by C.V. Raman in 1928 [4, 5].

C.V. Raman perceived that when monochromatic light of a frequency ν_0 is used, the scattered light produces a configuration of lines of shifted frequency- the Raman spectrum. Furthermore, he noted that the shifts are energetically independent of the exciting frequency, ν_0, and are characteristic of the chemical structures of the analyte leading to the scattering [5]. This effect was only measured early on with a few pure organic solvents at extremely high concentrations so as to be visible to the eye. However, once the solutions became more dilute, or one analyzed a solid substance, the effect was too weak to easily observe. As such, the many applications of this technique were delayed for several decades until the advent of lasers and more efficient detection systems. Currently, it is now possible to observe Raman scattering in materials that would have been unfeasible just a few decades earlier.

The Raman effect occurs when a beam of monochromatic exciting radiation interacts with a material and scattering occurs. Most of this scattered radiation has the same energy as the incident photons (elastic scattering) and is known as Rayleigh scattering. However, a small portion of this scattered radiation has either higher or lower energy than the incident photons (inelastic scattering) and is known as Raman scattering. Due to light-matter interactions, energy is either gained or lost by the molecule during Raman scattering. As such, the conservation of energy states:

$$h\nu + E = h\nu' + E' \tag{1.1}$$

where ν and ν' are incident and scattered frequencies while E and E' are the initial and final energy of a molecule, respectively. The previous equation can be rewritten as:

$$\Delta E = h(\nu' - \nu) \tag{1.2}$$

Based on the above equation, scattered radiation can be classified into the following categories:

a) Rayleigh scattering where $\Delta E = 0$, or when $\nu = \nu'$

b) Stokes scattering where $\Delta E < 0$, or when $\nu > \nu'$

c) Antistokes scattering where $\Delta E > 0$, or when $\nu < \nu'$

In other words, Rayleigh scattering occurs when the incident radiation has the same energy as the incident photons. Rayleigh scattering is the most prevalent and intense of the three types. Stokes scattering occurs when the overall change in energy is negative. Stokes shifts are seen at wavenumber shifts smaller than the Rayleigh line, making them red shifted. Antistokes scattering is observed when the energy of the incident photons is greater than the exciting radiation and are found at wavenumbers greater than the Rayleigh line, making them blue shifted. Overall, the Raman effect occurs when incident radiation impinges upon a given molecule and interacts with the electron cloud of the molecule's bonds [6]. The electrons in the cloud are then excited into a virtual state.

Figure 1.1 shows a schematic of a basic energy level diagram for the three types of scattering. The location of the electrons within the vibrational levels prior to excitation into a virtual state helps determine the shift that is observed. When the electrons begin at the lowest vibrational level of the ground state and relax to an excited level, Stokes shifts are observed. Antistokes shifts occur when the electrons begin in an excited vibrational level at ground state and relax to a lower level. However, at room temperature, the number of molecules starting at an excited state will be extremely small; thus, Antistokes shifts are much less common unless the temperature is increased. Still, regardless of the shift that is observed, in order for the Raman effect to occur there must be a change in polarizability of the electron cloud of the molecule [6].

When a molecule is placed in an electric field, the electrons and nuclei become displaced, resulting in an induced dipole moment; this molecule is then said to be polarized. As such, the strength of the electric field, E, and the magnitude of the induced dipole, μ, lead to:

$$\mu = \alpha E \tag{1.3}$$

with α representing the polarizability of the given molecule. The electric field strength of an electromagnetic wave of frequency ν is expressed as:

$$E = E_0 \cos 2\pi\nu t \tag{1.4}$$

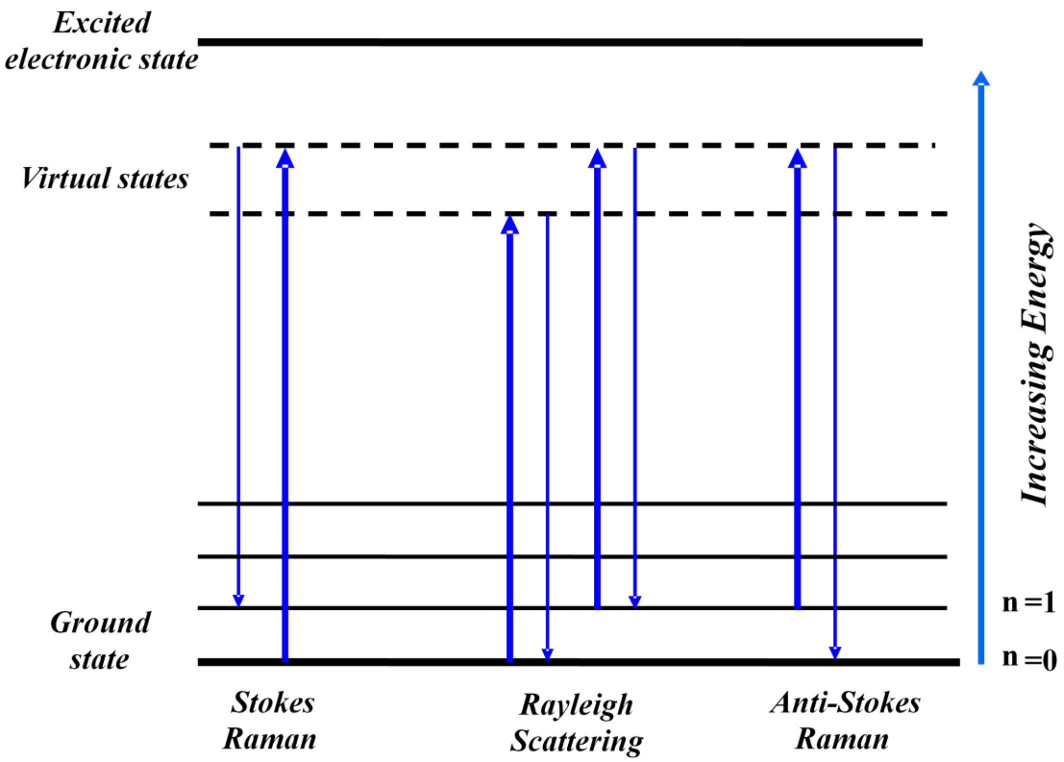

Figure 1.1: Schematic of Raman energy level diagram.

where E_0 represents the amplitude of the electromagnetic wave. When combining equations (1.3) and (1.4), the following equation occurs:

$$\mu = \alpha E_0 \cos 2\pi\nu t \tag{1.5}$$

With the above equation, one could conclude that the interaction of electromagnetic radiation, of frequency ν, induces a dipole moment oscillating at the same frequency. However, the polarizability actually changes with small displacement from its equilibrium position, as seen by:

$$\alpha = \alpha_0 + \left(r - r_{eq}\right)\frac{\partial\alpha}{\partial r} \tag{1.6}$$

where α_0 is the equilibrium polarizability and r and r_{eq} are bond lengths at a given instant and at equilibrium position, respectively. Assuming the molecule exhibits simple harmonic motion, the displacement can be shown as:

$$r - r_{eq} = r_{max} \cos 2\pi\nu_j t \tag{1.7}$$

with ν_j being the vibrational frequency of a molecule and r_{max} being the maximum distance of separation between atoms relative to their equilibrium position. When equation (1.7) is substituted into equation (1.6), the following formula occurs:

$$\alpha = \alpha_0 + \left(\frac{\partial\alpha}{\partial r}\right) r_{max} \cos 2\pi\nu_j t \tag{1.8}$$

Finally, when the above equation (1.8) is used with equation (1.5), the following is seen:

$$\mu = \alpha_0 E_0 \cos 2\pi\nu t + E_0\, r_{max} \left(\frac{\partial\alpha}{\partial r}\right) \cos 2\pi\nu_j t \cos 2\pi\nu t \tag{1.9}$$

which can be rewritten as:

$$\mu = \alpha_0 E_0 \left(\frac{\partial \alpha}{\partial r}\right) \cos 2\pi \nu t + \tag{1.10}$$

$$\frac{E_0}{2} r_{max} \left(\frac{\partial \alpha}{\partial r}\right) \cos\left[2\pi\left(\nu - \nu_j\right)t\right] +$$

$$\frac{\mathrm{E}_0}{2} r_{max} \left(\frac{\partial \alpha}{\partial r}\right) \cos\left[2\pi\left(\nu + \nu_j\right)t\right]$$

In equation (1.10), the first term occurs at the excitation frequency ν and corresponds with Rayleigh scattering. The second and third terms represent Stokes (ν-ν_j) and Antistokes (ν+ν_j) scattering. The excitation frequency has been modulated by the vibrational frequency of the bond in both Stokes and Antistokes scattering.

1.1.2 Instrumentation

As mentioned previously, a sample is irradiated with monochromatic light in Raman experiments. The scattered light is traditionally observed at right angles to the incident radiation. In modern confocal Raman microscopes, however, the scattered light is collected by a microscope objective at a 180° geometry; still, most basic components are the same. A modern Raman instrument generally consists of four main components: a laser source, a sample-illumination system, holographic optics, and a spectrometer with an appropriate detector [7].

For Raman spectroscopy, extremely intense sources of radiation are needed as intensities for scattered radiation is generally weak. The high intensity of lasers usually yields a great enough intensity of Raman scatter that it is measurable with reasonable signal-to-noise ratios [8]. The most common lasers used in Raman scattering include Argon-ion, Krypton-ion, Helium-Neon, and Diode lasers [9]. Since Raman scattering intensity varies as the fourth power of the laser frequency, those lasers with a shorter wavelength (Argon at 488/514 nm and Krypton at 530.9/647.1 nm) provide more intense Raman lines [9]. These higher intensity lasers, however, can lead to increased fluorescence emission and photodegredation of samples due to the greater energy. Lasers in the near-IR region, such as a Diodes (782/830 nm), have become more popular due to the ability to operate at a higher power with a decreased chance of photodegredation. Moreover, the lasers are not energetic enough to produce many excited electronic states of a molecule, making fluorescence less of an issue. He-Ne (632.8 nm) laser sources fall in the middle and can minimize the above effects while still providing strong intensity for Raman studies.

To study the Raman effect, the type of sample-illumination system used depends greatly on the type of radiation source. The laser must be tightly focused on the sample due to the weakness of the Raman effect [10]. Also, the scattered radiation must be collected efficiently. The excitation of the sample and collection of the scattered light is accomplished by utilizing numerous optical configurations usually either a 90° or 180° scattering geometry. Most new instruments have adopted the 180°, or backscattering, system as the 90° geometry has an optimum concentration required to maximize the Raman signal. The backscattering method avoids this pitfall and can easily correct for self-absorption in colored solutions [7].

In a Raman spectrometer, there are a few holographic filters, or wavelength selectors, placed throughout the path of the laser. Initially, a narrow band-pass filter is placed between the laser and the sample to help isolate the exciting line. Secondly, a holographic notch filter is used after the sample to provide narrow band width rejection of the given laser line. The filter transmits a small about of the backscattered laser line (often better than 10^4 rejection) while allowing 90% of the enduring frequencies to reach the detector.

The backscattered light is transmitted to the spectrometer, where divergent light is collimated by a spherical mirror. The light is then diffracted by a grating and the diffracted light is then focused by a second mirror [9]. The spectrum is then projected onto the detector, most commonly a charge coupled device (CCD). A CCD is comprised of a series of silicon photosites (pixels) placed in a two dimensional array [11]. Each pixel is surrounded by a non-conductive barrier and has two conductive electrodes separated by a thin silica dielectric layer. A charge buildup on the surface of a pixel is induced when a photon strikes it. The charge buildup is then stored in a capacitor until the Raman signals are collected. The number of electrons collected by each pixel is recorded by the computer and produces the Raman spectrum observed [12].

The type of Raman spectrometer used in the studies conducted and presented throughout this dissertation (see Figure 1.2) is a confocal Raman system. The instrument is a JY-Horiba LabRam Spectrograph with a 632.8 nm He-Ne laser. The spot size is dependent on the microscope objective in use. Confocal Raman systems have several advantages including the efficient rejection of stray light and fluorescence [7]. Moreover, confocal systems offer high throughput, good collection efficiency, and smaller sample requirements [13].

1.1.3 Resonance Raman Spectroscopy

A specific type of Raman spectroscopy that is important to note is resonance Raman spectroscopy. Resonance Raman is observed when the exciting frequency

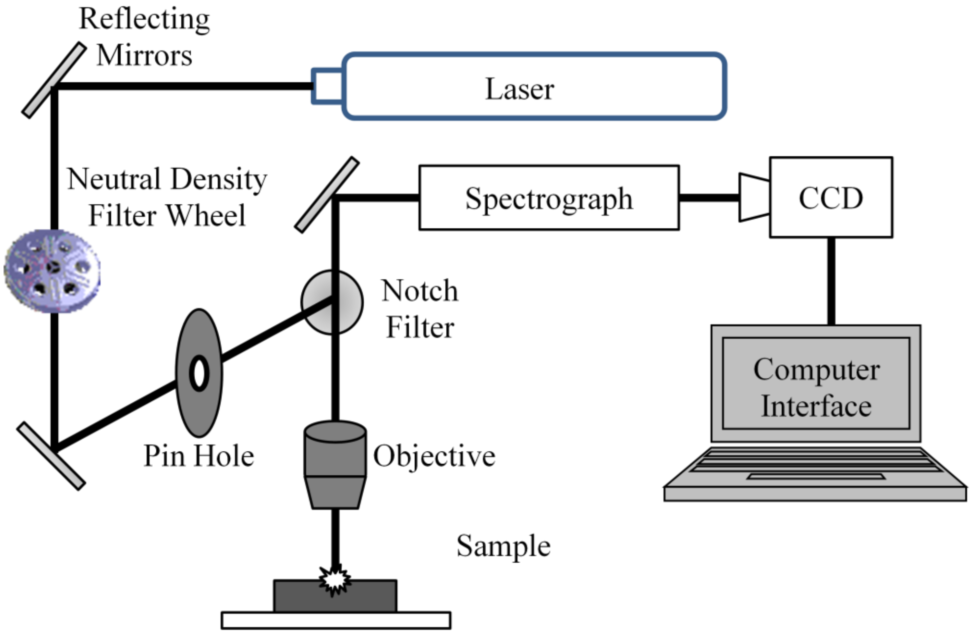

Figure 1.2: Schematic JY Horiba LabRam Spectrometer used in current studies.

corresponds to the energy required for an electronic transition of the molecule. The resulting Raman signals have been enhanced as much at 10^2-10^6 greater than normally observed [14], meaning the detection limit for resonance Raman scattering is often much lower than other techniques. Furthermore, as resonance Raman only occurs with the bands associated with the given chromophore, most spectra consist of only a few lines. This allows for the targeting of specific absorption bands so as to selectively acquire a resonance Raman spectrum. However, it is often difficult to operate the technique in the resonance region of all given samples and tunable lasers are usually required to take advantage of the enhancement.

Resonance Raman scattering occurs differently than both normal Raman scattering and fluorescence. Unlike normal Raman, resonance Raman varies energetically as electrons are promoted to an excited state and followed by an immediate relaxation to a vibrational level of the electronic ground state [15]. The relaxation in resonance Raman is also not preceded by radiationless relaxation to the lowest vibrational ground state of the excited electronic state as is seen with fluorescence (Figure 1.3). Also, the time for a fluorescence process occurs in nanoseconds while resonance Raman can happen in a picoseconds or less [15]; fluorescence often interferes with resonance Raman [9].

As seen, Raman scattering results from the quantized vibrational changes, similar to those seen with infrared absorption, showing the observed Raman signal of a molecule. The differences between incident and scattered visible radiation wavelengths exist within the mid-infrared regions of the spectrum. One advantage Raman has over other vibrational techniques, such as infrared (IR) absorption, is the ability to analyze analytes

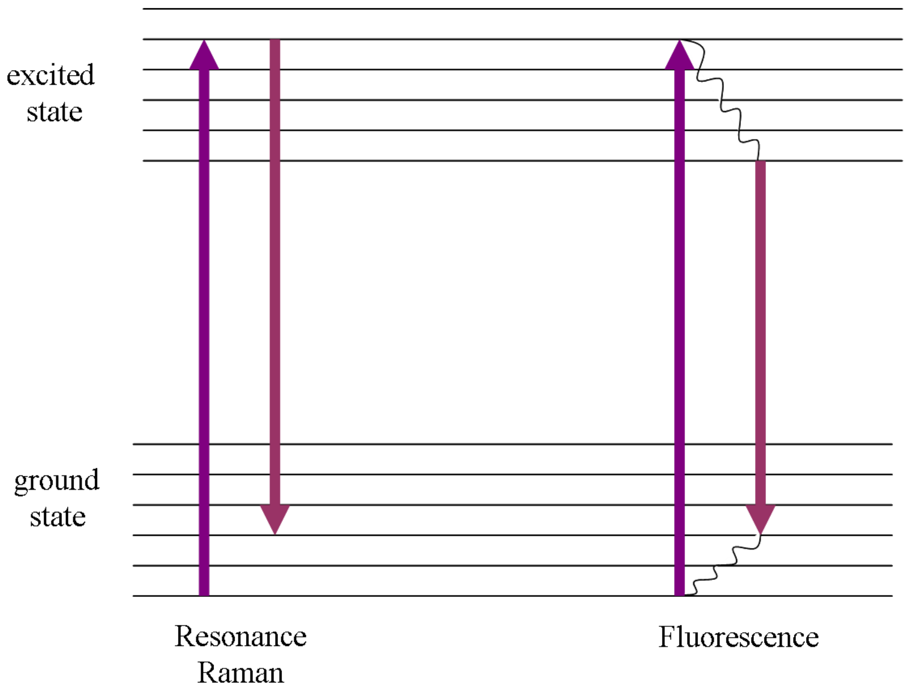

Figure 1.3: Energy level diagram for (left) resonance Raman scattering and (right) fluorescence emission.

in aqueous solutions. Also, IR absorption has difficulty with glass or quartz cells holding a sample due to interference; however, these limitations are not present with Raman scattering. Still, Raman will always have limitations in the extremely small cross sectional areas, leading to poor sensitivity. Moreover, fluorescence often competes with Raman signals of certain samples, particularly if not using a near-IR laser source [16]. Even still, there are techniques to work around these limitations in sensitivity.

1.2 Surface Enhanced Raman Spectroscopy (SERS)

1.2.1 Overriding theory

As mentioned previously, one of the drawbacks to conventional Raman spectroscopy is its inherently small cross section, or the probability of the effect occurring. A typical cross section for a molecule in Raman spectroscopy is around 10^{-30} cm^2 [17]. In contrast, the cross sections for Rayleigh scattering and fluorescence are approximately 10^{-26} and 10^{-19}, respectively. This inherent weakness results in a lack of sensitivity and poor limit of detection [2], thus limiting potential analysis to neat analytes or those with a concentration greater than 0.1 M [9]. To improve sensitivity, expand the list of potential analytes, and strengthen overall analyte signal, surface enhanced Raman spectroscopy (SERS) can be used.

SERS was first observed by Fleishmann et al. in 1974 when a roughened silver electrode enhanced the signal of pyridine adsorbed to its surface [18]. This research focused on implementing Raman spectroscopy as a potential method for observing molecules on surfaces with monolayer coverage. Fleishmann et al. inferred that the amplified pyridine signal was caused by increased surface area from the roughened silver electrode. In 1977, two separate research groups, Jeanmarie and Van Duyne [19] and Albrecht and Creighton [20], noted that the observed enhancement could not be accounted for solely by an increased surface area and that other mechanisms must exist. They proposed that the enhancement was coming from another mechanism involving the adsorbed molecules on the surface. For the next decade, researches into the SERS effect increased greatly and by 1985 attributes of experiments as well as general mechanisms governing SERS were commonly agreed upon, although the particulars of the mechanisms are still the subject of active debate.

SERS involves a selection of molecules being adsorbed onto the surface of a variety of metals with differing morphologies. Typically, silver, gold, or copper are the chosen metals comprising SERS substrates; however, there have been successful experiments involving a variety of metals as well [17]. These coinage metals are usually used since the resonance condition for these metals lies at common laser frequencies for Raman spectroscopy. Also, at the resonance frequency, the dielectric function for these metals is minor. While a theoretical basis for the SERS effect has been debated substantially [21-23], the simplistic explanation is that the intensity of the Raman scattering is proportional to the induced dipole, μ_R, of the given molecule. Additionally, μ is proportional to the polarizability of the molecule in question, α, and the magnitude of the incident electric field, E. This is seen with the expression (1.3) discussed earlier in the chapter where it is seen that an increase in the molecular polarizability or the magnitude of the field that is experienced can enhance the observed Raman scattering intensity.

Based on the above findings, there are generally two accepted enhancement mechanisms responsible for SERS: Electromagnetic (EM) and Chemical Enhancement (CE) mechanisms. The EM models account for E-related enhancements and are independent of the adsorbed analyte. The CE models, however, account for α-related enhancement and are specific to the chemical interaction between the adsorbed analyte and the metallic surface. The chemical effect is less understood and regarded as the lesser contributor (enhancements of two or three orders of magnitude) to overall SERS enhancement [17]. EM, however, is the dominant mechanism [16].

1.2.2 Enhancement mechanisms

Electromagnetic Enhancement

Of the two forms of SERS enhancement, EM enhancement is by far the greatest contributor to overall signal enhancement and can contribute as much as 10^{11} [24, 25]. EM enhancement is usually observed when a SERS substrate is prepared with a roughened metal surface, consisting of features smaller than the wavelength of light in use [26, 27]. As observed in Raman spectroscopy with equation (1.3), when monochromatic radiation of frequency, ν, and electric field, E, interacts with a molecule, a Raman dipole is induced. This dipole oscillates at a frequency, ν_R, and radiates power proportional to the square of the induced dipole ($|\mu_R|^2$). In the far-field, this frequency is detected as Raman signal.

A similar description can be applied to SERS with some alterations based on the presence of a roughened metal surface. These distinctions include the potential for the EM field as the metal's surface to be greatly increased, resulting in possible local field enhancements. Moreover, the Raman dipole radiation properties can be affected by the metallic environment leading to potential radiation enhancement. More specifically, when EM radiation impinges upon the surface of an appropriate metal substrate, conduction band electrons begin to oscillate at a frequency equal to that of the incident light. These oscillating electrons are known as *surface plasmons* when at or near the surface [28]. Surface plasmons can be characterized as one of two types: propagating or localized. Propagating surface plasmons move across the surface in the x-and-y-directions along the metal-dielectric interface [28, 29]. Localized surface plasmons, however, are restricted to the surface of a nanoparticle at a localized surface plasmon resonance (LSPR) frequency [28, 30]. Moreover, for localized surface plasmons to be excited by light, the metal substrate must have a roughened surface. The EM field of light at the surface can be enhanced greatly with appropriate conditions, including size and shape of nanoparticles, to excite surface [17, 28, 30].

To achieve a large EM enhancement of the signal for an analyte, it is necessary for the resonance of the surface plasmons to correspond with the wavelength of the incident radiation [31]. The amplification for both the incident field of the laser and the scattered Raman field makes up the EM enhancement mechanism for SERS through their interaction with the roughened substrate surface [17].

To illustrate the EM mechanism, a simple case involving a metal sphere (with a radius much smaller than the wavelength of light) in an external electric field can be used. With a uniform electric field across the particle and the field induced as the particle's surface related to the laser field, the following equation can be used:

$$E_{induced} = \left\{\frac{[\varepsilon_1(\omega) - \varepsilon_2]}{\varepsilon_1(\omega) + 2\varepsilon_2}\right\} E_{laser} \qquad (1.12)$$

with $\varepsilon_1(\omega)$ being the complex, frequency dependent dielectric function of the metal while ε_2 is the relative permittivity of the ambient environment. Furthermore, at a frequency where:

$$(\varepsilon_1) = -2\varepsilon_2 \qquad (1.13)$$

the function is completely resonant. The local field experienced, in which a molecule adsorbed on the surface of the particular particle, is strongly increased by excitation of the surface plasmons. Specifically, the particle has localized the plane wave of the light as a field centered in the sphere that decreases as the distance from the surface grows. The particle enhances the incident field and Raman scatter field. Since the above model focuses on a simple sphere, the numerical factor of 2 in equation (1.12) will change with differing structures.

Finally, it is important to mention that the local field intensity at a specific point is proportional to the square of the electric field amplitude at that given point. Furthermore, the local field intensity enhancement factor (LFIEF) at a specific point can be normalized to that value with respect to the intensity of the incoming field at the known point. This can be represented by:

$$LFIEF(r) = \frac{|E(r)|^2}{|E_0(r)|^2} \qquad (1.14)$$

Still, the overall enhancement scales to approximately E^4; Raman scattered light and the incident laser differ in frequency, so the enhancement more correctly is:

$$EF \approx LIFEF_{Scatter} LIFEF_{Laser} \qquad (1.15)$$

where EF is the enhancement factor. Both fields can be resonant with the surface plasmons with small frequency shifts. The above formula is only an approximation of the real EF and further approximations are often possible [32]. Equation (1.14) contains several implicit approximations, including the fact that it ignores any polarization complications between the incoming and scattered fields. Still, in many cases, the difference between the frequency of scattering and the laser can be ignored. When taking the LIFEF at a specific point seen in Equation (1.14) with the approximation in equation (1.15), EF can be approximately calculated as:

$$EF \sim LFIEF^2 = \frac{|E(r)|^4}{|E_0(r)|^4} \tag{1.16}$$

This is known as the $|E|^4$ approximation for SERS enhancement. Even though the equation has many simplifications, it is still a useful tool when estimating actual enhancement and provides a good figure of merit when comparing models and experiments [33].

Chemical Enhancement:

While it is well documented that EM enhancement provides the vast majority of SERS enhancement, other forms of enhancement exist and are normally grouped under the heading of chemical enhancement. It is important to note that the EF's described earlier would still exist even if there was no molecule on the surface as they are an intrinsic property of the substrate specifically. Once a molecule is introduced into the situation, its simultaneous interaction between the metal and the EM field can achieve added SERS enhancement; the effect is multiplicative when both CE and EM mechanisms are present. As such, it is extremely difficult to separate these effects from a system with both forms of enhancement. Even still, CE contributes little overall in terms of signal enhancement with often no more than an additional factor of 10 [32].

In general, the CE effect to SERS is short ranged (< 0.5 nm) since it depends on the adsorption site, bond geometry, and energy levels of the adsorbate molecule. The CE mechanism is looked at as a resonance Raman mechanism. The most common explanation of CE is based in a charge-transfer (CT) mechanism. The CT mechanism is attributed to an increase in the molecular polarizability of the molecule resulting from the formation of a metal-adsorbate complex [2]. Chemisorption occurs due to the adsorbate bonding to the metal surface and forming new electron states which serve as resonant intermediate states. Moreover, the highest occupied molecular orbital (HOMO) and the lowest unoccupied molecular orbital (LUMO) of the adsorbate are symmetrically disposed in energy with the Fermi level of the metal (see Figure 1.4). These CT excitations occur from the Fermi level to the LUMO with retro-donation of electrons from the HUMO to the Fermi level of the metal. Furthermore, under specific conditions, the laser energy can be in resonance with the electronic excitation of the metal-adsorbate complex.

1.2.3 SERS applications

SERS has many advantages over other techniques for use in a variety of areas. In its simplest form, SERS is comparable to Raman spectroscopy with better sensitivity. As such, SERS still provides specific detail about the “fingerprint” of a given molecule or process. However, since conventional Raman has weak signal intensity, the useful technique has not been applied as universally as other methods. SERS has the ability to not only improve the sensitivity for those applications already used by Raman while also

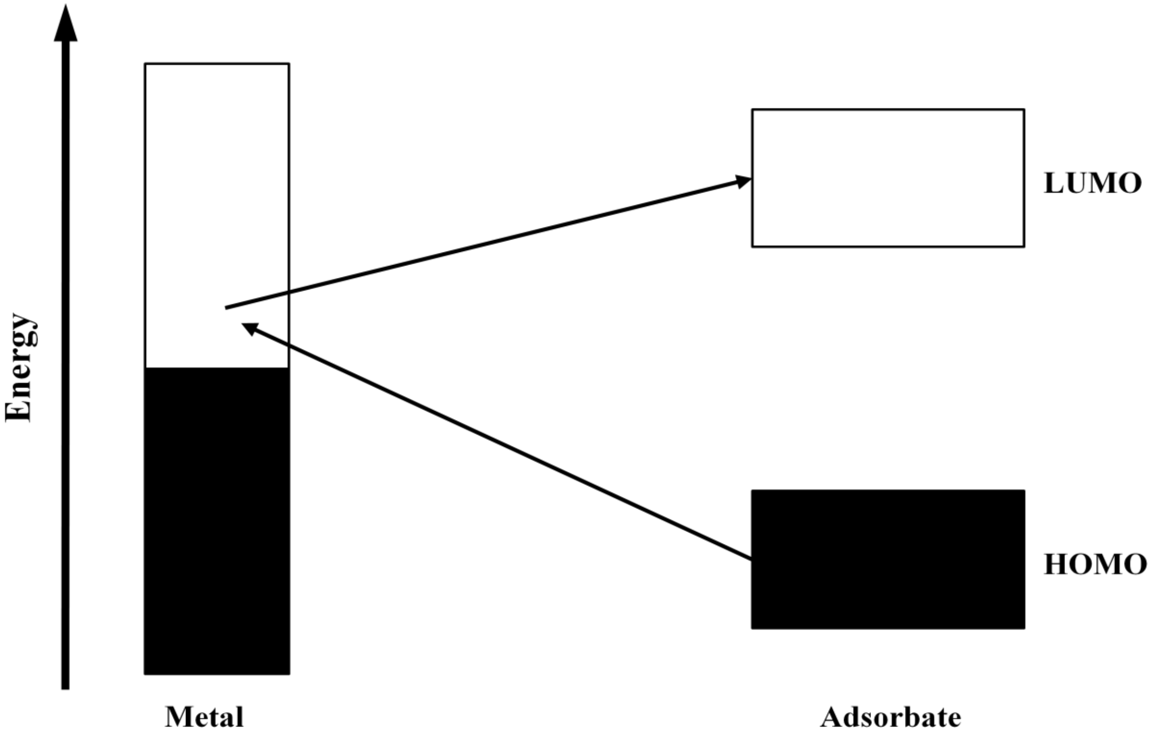

Figure 1.4: Molecular orbital diagram demonstrating origin of charge-transfer mechanism for chemical enhancement.

expanding the potential uses of the method to those that would not be possible without the added sensitivity and limits of detection. SERS has the potential to impact the areas of analytical chemistry, biochemistry, forensics, environmental analysis, trace analysis, and many others. Currently, this technique has been implemented successfully for detecting trace amounts of environmental contaminants [34, 35] and pharmaceuticals [36, 37]. The technique has been used in biochemical fields to help analyze electron transfer reactions in proteins [38] and provide quantitative DNA analysis [39, 40]. SERS has been successfully implemented in a variety of scientific areas and rivals fluorescence spectroscopy in many ways [41]. Still, SERS does have certain limitations as an analytical technique, many of which are related to the substrate in question.

.

Chapter 2

Surface-Enhanced Raman Spectroscopy Substrates and Nanofabrication Techniques

This chapter aims to discuss the variety of options for useful creating SERS substrates. Each fabrication method will be compared and contrasted with others to give a good representation of why one would be chosen over another in a given situation. Also, the last section of the chapter will describe some of the most popular fabrication techniques and demonstrate why electron beam lithography (EBL) was chosen for the work reported later.

2.1 SERS substrates

As mentioned in Chapter 1, the SERS effect is based mainly on two mechanisms related to enhancement: chemical and electromagnetic. Chemical enhancement is dependent on the analyte adsorbed onto the surface of the substrate and the nature of the metal surface, leading to a relatively small enhancement. Electromagnetic enhancement, however, is not dependent on the analyte in question and is easily observed on roughened metal substrates which have features smaller than a wavelength of light. The EM mechanism can provide SERS enhancement of greater than 10^{11} [42] under optimum conditions, although enhancement of this magnitude is difficult to achieve.

Even still, there is generally a consensus on what traits a model SERS substrate should possess. Based on the comprehensive discussions [43], the ideal SERS substrate should have:

a) Strong SERS activity, leading to high sensitivity.
b) Tunable with different systems to better maximize enhancement.
c) Substrate and enhancement uniformity.
d) Good stability and reproducibility between individual substrates.
e) Ability to be applied to a variety of analytes of differing properties.

Unfortunately, achieving these objectives is not trivial. One reason that it is difficult to obtain extremely high enhancement is that the SERS effect is highly dependent on nanoparticle shape, size, and structure with regards to the given wavelength and dielectric properties of the substrate [28, 30, 44]. A great amount of research has been devoted to developing SERS substrates to take advantage of the high EM enhancement available. SERS substrates can possess both random and controlled morphologies so as to find the best way to tune the observed effect to the specific experiment.

2.1.1 Random morphology substrates

The first SERS substrates, as mentioned in Chapter 1, consisted of roughened silver electrodes [18]. The electrode surface was altered by an oxidation-reduction cycle in an electrochemical cell containing silver salts causing a roughened silver film on the electrode surface. This substrate allows for the examination of charge transfer between both analyte molecules and substrate metal surface as well as orientation of the molecules at or near the surface through adjustments in electrode potential [45]. However, the use of these electrode substrates has waned over the years due to relatively low enhancement.

Vacuum deposited metal island films are another random morphology substrate commonly used in SERS analysis. These substrates include metals on planar surfaces such as glass, quartz, and silicon wafers or nanoparticles embedded surfaces such as silica beads and polystyrene [46, 47]. Metal island films are often high purity and relatively easy to prepare. The metal island films can also be tuned somewhat to appropriate localized surface plasmon resonances by altering parameters such as film thickness and deposition rate, with most thicknesses of metal being between 5-20 nm [31]. An example of a Ag island film on glass can be seen in Figure 2.1a.

Random morphology SERS substrates also include a class involving metal-poly(dimethylsiloxane) (PDMS) nanocomposites. This type of substrate has some similarities to conventional metal island substrates as a film of metal is deposited onto the surface. However, unlike other surfaces, the PDMS allows the metal to embed itself into the top layer of the polymer, substantially increasing the overall surface area and offer some protection against oxidation. The polymer allows analytes to partition into the top layer due to its solid-phase extraction capabilities. Added interaction between the metal particles and analyte leads to a greater enhancement than that of traditional metal island films [48]. Figure 2.1b shows an image of a Ag –PDMS nanocomposite used for SERS analysis.

The most common type of random morphology SERS substrate is simple colloidal silver or gold nanoparticles. Systems usually have particles ranging from 10-150 nm can consistently yield large signal enhancement [49]. Metallic colloids are

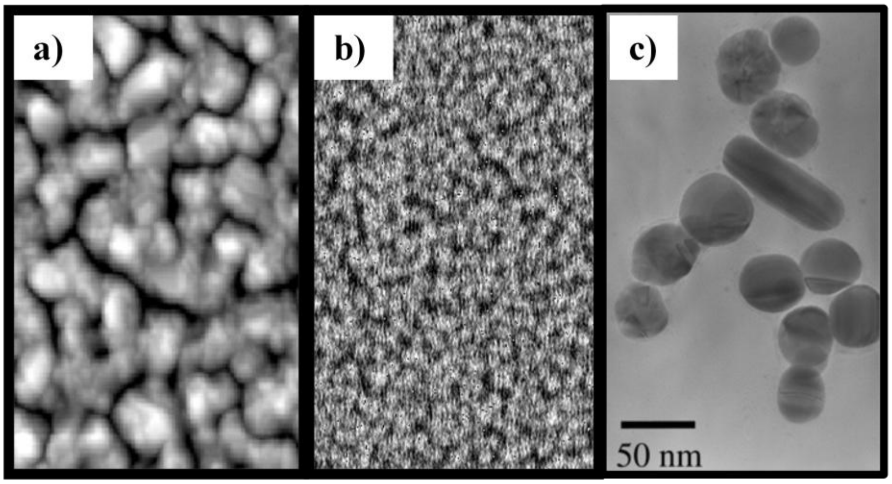

Figure 2.1: Examples of non-lithographically fabricated random substrates. a) Ag islands on glass, b) Ag nanocomposite with PDMS, c) Aggregated Ag colloid particles.

generally produced by reducing metal salts, often silver nitrate with sodium citrate. The reduction can also be done in a careful and controlled manner to create cubes, rods, triangles, and other structures [50]. The most common use for colloidal systems currently is with single molecule SERS detection (SMSERS) [44, 51]. In these systems, aggregated clusters of metal colloid can possess “hot spot(s)” within the aggregate itself that achieve extremely high enhancement [52, 53]. There is debate as to the exact reason for the areas of high enhancement and whether it is the aggregates specifically or if a “hot” particle becomes entrapped in the aggregate. Still, it has been shown that hot aggregates can contain a wide variety of particle numbers and configurations [54, 55]. An example can be found in Figure 2.1c.

Overall, the use of random morphology substrates has certain benefits including ease of fabrication and modest to occasionally strong enhancement, but there is often a lack of reproducibility in the substrates. Even though colloid has shown extremely high enhancement, the hot spots created are difficult to find and recreate. These hot areas also account for less than 1% of the surface area of the SERS substrate [56]. For SERS to move toward having a greater impact analytically, these issues must be dealt with appropriately.

2.1.2 Deterministic Ordered SERS substrates

Even though random morphology SERS substrates have allowed single molecule detection, drawbacks to these types of platforms have begun to limit their use. Ordered morphology SERS substrates have become more popular as the need for reproducible results expands. Also, ordered SERS substrates offer the ability to have greater control over a variety of substrate features including nanoparticle size and shape. Ordered substrates can more likely be tuned to system needs whereas random morphology substrates are difficult to control.

Despite the potential of ordered substrates, to date it has been difficult to create an ordered substrate that produces exceptional and uniform enhancement. The development of better performing SERS substrates that can be easily controlled and manipulated to fit a given situation continues to be an active area of SERS research. Once an appropriate substrate is created, the ability to use SERS as an analytical tool would increase dramatically. As such, the area of nanofabrication has become more commonly implemented in the SERS arena.

2.2 Relevant nanofabrication techniques

Aside from looking at the SERS system that provides for the greatest enhancement, there are other important considerations to be accounted for when determining the best substrate. Ideal SERS substrates can provide a variety of benefits including reproducibility and uniformity. Easily produced and implemented SERS platforms are prominent factors as well since the fabrication of certain substrates can be complex. Furthermore, all fabrication methods have drawbacks and limitations that make certain techniques desirable in some situations but not others.

Nanofabrication at its core aims to create nanoscale structures with the ability to serve as components in specific devises or act as a complete system on their own. Furthermore, nanofabrication looks to reproducibly create large quantities of these devises at a fairly low cost. Overall two distinct groups of fabrication methods have emerged: bottom-up and top-down [57]. Bottom-down fabrication focuses on synthetic methods for creating substrates by assembling subnanoscale building blocks into specific patterns. The most common uses for these types of methods include biological and chemical sensors [58], but these methods have been used for SERS detection on numerous occasions. Top-down methods involve conventional lithographic techniques where nanoscale structures are created by removing parts of a bulk material, often by some etchant process. Also, the top-down approach patterns the chips in a specific place so there is no need for assembly. The top-down approach has been used commonly in electronic and photonic industries and is also becoming increasingly more common in the creation of SERS substrates [58], but certain limits have prevented rapid development in these areas.

2.2.1 Bottom-up SERS techniques

Bottom-up techniques have become some of the most popular non-random SERS substrates for bulk fabrication due to the relative ease of assembly. These techniques are often much less expensive than top-down techniques and require less specialized equipment. One common technique for SERS substrate fabrication is the chemical assembly, or self-assembly, method [59]. The method modifies the solid substrate (often silicon or glass) with bifunctional molecules for metal nanoparticle immobilization. The molecules form a compact layer with the solid substrate, allowing the other functional group to interact with nanoparticles. This process forms an ordered layer of nanoparticles for SERS analysis. Chemical assembly substrates can allow for a homogeneous SERS signal over a large area, but there can often be a problem either with aggregates forming on the surface or low SERS activity due to low electromagnetic coupling [60]. Even though the aggregation can be mitigated with proper cleaning, it is difficult to achieve a surface without defects, particularly on a large scale [59].

The Lagnmuir Blodgett (LB) method, originally used for preparing large areas with a film of amphiphilic molecules onto solid substrates [61], can alleviate the aggregation problem. Nanoparticles modified with hydrophobic molecules and dispersed into a volatile solvent immiscible in water, often hexane or chloroform. After dispersion into water, a layer of random nanoparticles at the interface can be created once the solvent evaporates. Finally an ordered layer of nanoparticles will form on the surface resulting from compression as the LB trough barrier moves [62]. The interparticle spacing will decrease during compression. Substrates prepared by this method have exhibited SERS enhancement of as much as 10^7 [63]. This simple procedure can be used with a variety of shapes and sizes of nanoparticles which align based on these properties. While the LB films can form highly ordered close-packed systems, many of the chemical modifications that are used to create specific nanoparticles interfere with SERS analysis.

Another popular technique, popularized by the Van Duyne group, is Nanosphere Lithography (NSL) [64, 65]. NSL is a type of template based fabrication used to create highly ordered SERS substrates. These substrates are created by assembling polystyrene or silica spheres of a given size onto a clean substrate. A layer of the ordered nanosphere film will form on the substrate by carefully controlling the assembly. Metal is then deposited on top of the nanosphere film, acting as a template, to a desired thickness. If the metal is deposited using physical vapor deposition, the SERS substrate can be used with the metal film over nanosphere (FON) or the nanospheres can be removed via sonication leaving surface-confined nanoparticles in the shape of a truncated tetrahedron

[59]. The metal film can also be created using electrochemical deposition prior to removal of the nanospheres, which leaves nanoholes [59]. Either way, NSL can produce SERS substrates with controlled features with the potential for high enhancement. However, the success of this method relies heavily on the experimental conditions. Also, it is difficult to achieve a surface without any point or line defects with nanospheres smaller than 200 nm [59].

Overall, bottom-up methods offer simple methods for creating relatively ordered SERS substrates. These substrates have been able to obtain enhancement of better than 10^7 when conditions have been optimized, allowing for some sensitive analysis. However, the reproducibility for these methods is still lacking and varies largely on the experimental conditions. Top-down methods using reproducible lithographic techniques have since become more popular.

2.2.2 Top-down SERS methods

Top-down fabrication methods have become more common for SERS substrates due to the potential for highly reproducible fabrication. These techniques can also allow for substrates to be easily tuned to the system of interest for analysis. However, these techniques do have certain limitation. One drawback to top-down methods is the amount of steps that each fabrication technique will require and the complexity of each step [66]. As the number of individual steps involved in processing increase, the need for accuracy in each step is amplified. Another hindrance to lithographic methods for SERS substrates are the physical limitations of the techniques themselves. Until recently, the resolution required to create a viable SERS substrate was difficult to achieve in a consistent manner [67]. Also, as with most nanofabrication techniques, throughput is often a problem for lithographic techniques. Improvements in the techniques and the instrumentation involved have begun to alleviate these issues, but they continue to be a limiting factor [66]. Still, the potential for reproducible substrates with strong enhancement exists for these advanced substrates.

SERS substrates can be fabricated using the focused ion beam (FIB) technique. A FIB instrument consists of an ion source, ion optics, a stage, and a vacuum system [68]. The ion beam, often Ga^+, is usually a liquid-metal ion source (LMIS). The LMIS is a high-brightness ion source that produces beams of heavier ions which can be focused to a spot size of smaller than 10 nm [69]. The beam is collimated into parallel beams by condenser lenses before passing though a mass separator and drift tube. This setup filters out unwanted ions from the alloy ion sources. A lens objective and electrostatic beam deflector focus the beam into a fine spot on the substrate for milling [68].

Milling is a process combining sputtering, material redeposition, and swelling. Most frequently, nanohole arrays (NHAs) are created with FIB milling as it has a higher throughput than milling vertical structures. The NHA systems are similar to other SERS substrates as they are highly dependent on size and shape of the nanoholes [57]. With high resolution it is easy to study the effect of separation on holes as well as optimize the system for a particular experiment. NHA periodicity is also easy to manipulate, even on the same substrate, leading to better SERS tunability [70]. Another benefit to FIB milling is that the initial substrate could easily be used as an imprint stamp with a substance such as PDMS [71, 72] allowing for improved throughput.

2.2.3 Electron beam lithography

An additional lithographic method that employs focused particle beams and has become more common with SERS is electron beam lithography (EBL). EBL uses similar principles as normal photolithography, only on a much smaller scale [57]. Like other top-down methods, EBL can reproducibly produce SERS substrates with known features and good resolution. Although cost and throughput are drawbacks to this technique, the benefits of this technique, particularly for academic purposes, outweigh the potential limitations.

The work reported herein focuses on developing SERS substrates via electron beam lithography. EBL has the potential to create small, reproducible structures of a variety of shapes and sizes. EBL pattering was first developed in the early 1960’s using modified electron microscopes [62]. Since the Gaussian beam was already converged as much as possible, the resolution was already under 1 μm. The largest application of EBL has been the semiconductor industry for use with patterning on masks and reticles [73]; the method has progressed rapidly as miniaturization and circuit integration become more important. Since modern EBL instrumentation offers much higher resolution and fast turn-around time, it has become vital to the development of advanced devices. However, the slow pattering process has hampered its ability in mass-production settings [73]. Some techniques have emerged recently to improve the throughput of EBL including variable-shaped beam lithography [74], electron projection lithography [75, 76], and low-energy electron beam proximity projection lithography [77]. These techniques are generally reserved for mass-production, although they do not produce the same resolution achieved through standard EBL. Also, many of the higher throughput techniques use bulky and complex masks which can prove costly and difficult to fabricate as the feature sizes continue to shrink.

A typical EBL system consists of three main components: an electron gun or source, a vacuum system or column to focus the electron beam, and a computer system that controls the various parts [78]. Figure 2.2 is a simplified schematic of a common EBL system. The electron gun controls the creation of the electron beam with the first step producing the electrons by cathodes or electron emitters. Once formed, the electrons are accelerated by electrostatic fields producing greater energy. These electrons are then focused into a beam. The manipulation of the beam then happens under a high vacuum. A series of electric and magnetic lenses can focus and deflect the beam to a specific point on the substrate. Finally, the computer system coordinates the movement of the electron beam over the substrate and whether or not to expose the substrate underneath to the beam [73]. The control system can intermittently turn the beam on and off so as the intended location(s) are the only ones being “written” on.

EBL is generally used either in mask making for use with other lithography or, as in this case, in a direct writing process on the semiconductor substrate [78]. EBL is different than most photolithography in that the directed electrons, rather than photons, specifically expose a known location on the substrate instead of the entire surface. As such, there is no need for a mask when working with EBL [73]. The patterns are instead created by the areas that are exposed to the electron beams. The surface of the substrate is often coated with a photoresist, an electron sensitive material often coating a semiconductor wafer [71]. There are a variety of resists with different properties

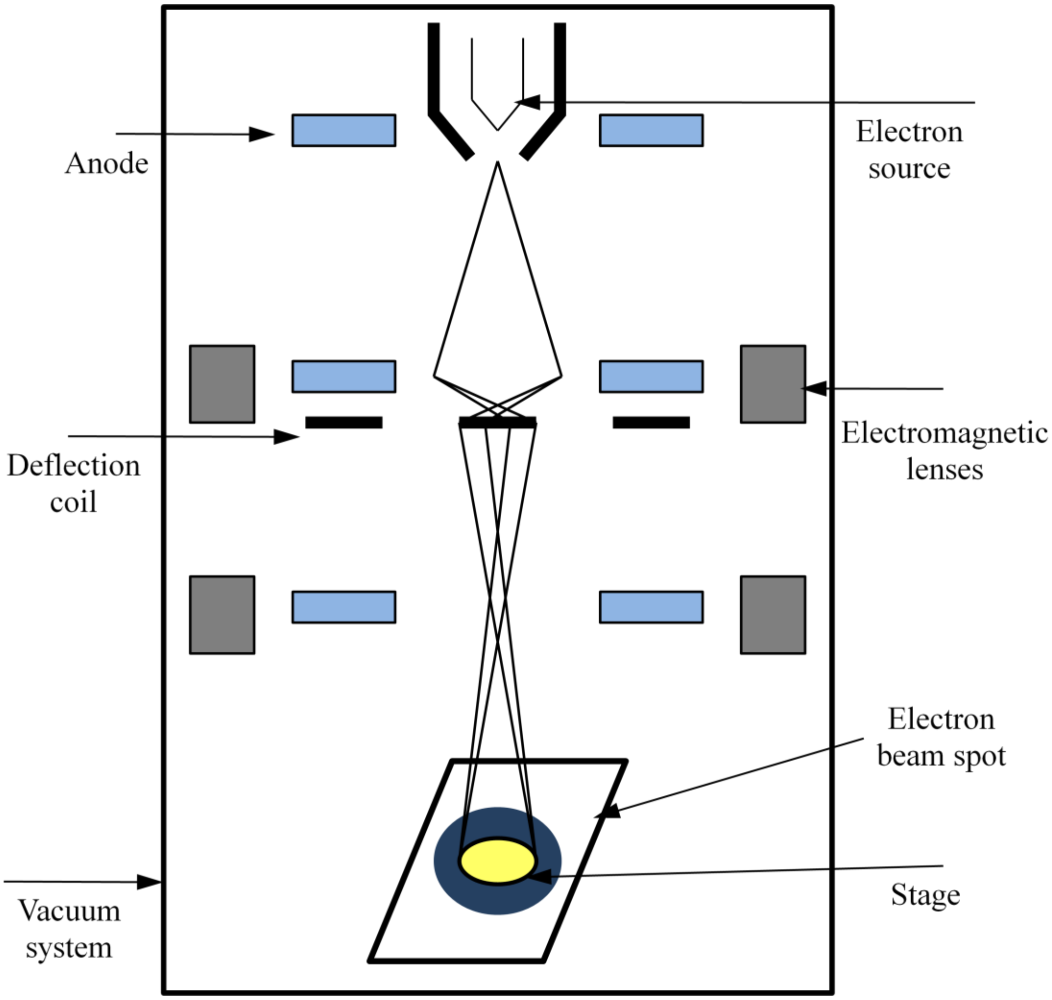

Figure 2.2: Simplified schematic of an electron beam lithography system.

including resolution and throughput time, but the biggest distinction is if the resist is positive or negative tone. Positive tone resist molecules become resolved (depolymerized) after exposure to the electron beam while negative tone resist molecules polymerize after exposure. The resolved positive resist areas are then removed during development, creating space where the pattern was written. The polymerized negative tone resist, however, remains during chemical development while the rest of the resist rinses away. Figure 2.3 shows a schematic of the process for the two types of resist development. Once the resist has been developed, further steps can be taken to complete the substrate if necessary.

When compared to traditional photolithography, EBL can accomplish much greater resolution since the electron beam spot size can be focused to ~1 nm. Overall, the resolution for photolithography is approximately +/- 0.5 µm at its best while EBL can be optimized to obtain resolution better than +/- 10 nm [66]. To achieve the high precision and resolution that EBL is known for, the system must be optimized to avoid extraneous resist exposure. Extra resist exposure can occur with electrons of extremely high or extremely low energy [79]. With high energy electrons, the beam diffuses deeper into the resist, causing more area to be exposed. Low energy electrons cannot scatter enough over large distances, leaving certain areas to be more exposed than others. The resolution for lithography is also linked with the type of resist used. Furthermore, the type of developer employed can help yield better contrast between developed and undeveloped areas, improving the resolution greatly. The Zep 520A resist utilized in the work reported herein is a type of high resolution PMMA and has resolution better than 10 nm [80].

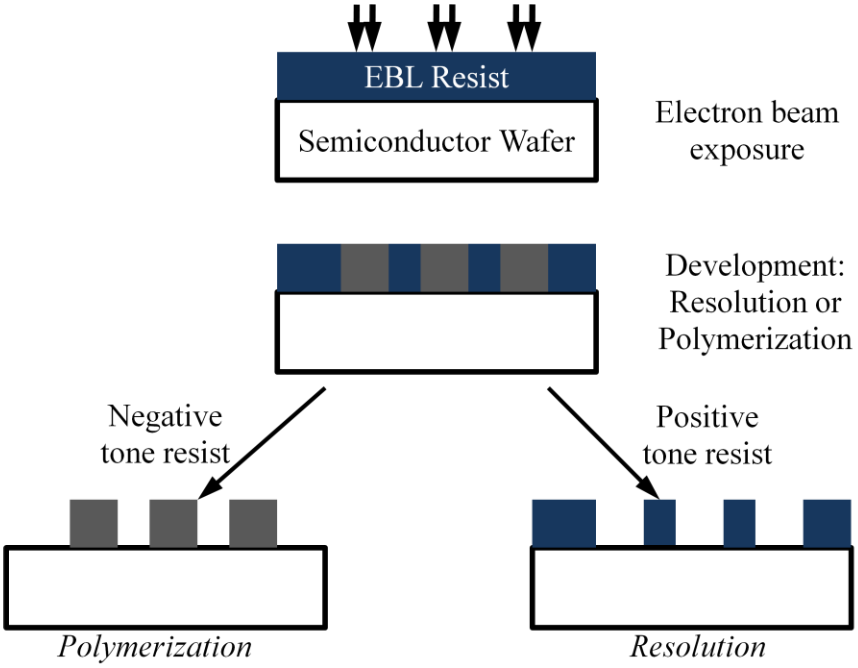

Figure 2.3: Illustration of the differences between direct (left) and in indirect/liftoff photolithographic procedures.

Due to its controlled nature, several research groups have used EBL to fabricate SERS substrates. Previously, our group has demonstrated a direct EBL technique for fabricating ordered nanostructures before vapor deposition of Ag to create reproducible SERS substrates [81]. Other groups have often used EBL to create metal nanoparticles by using a lift-off technique that removes unwanted resist after a metal layer has been placed on the substrate surface [82-84]. This leaves the metallic features in known patterns for SERS analysis. Still, the overall goal for these projects is to create a reproducible SERS substrate that can produce signal enhancements similar to those of the random morphology substrates. The work reported herein focuses some on developing a new method of EBL fabrication in conjunction with reactive ion etching (RIE) for SERS substrates to gain better control over the features in question as well as increase overall SERS enhancement.

2.2.4 Reactive Ion Etching

The largest difference between the method used in previous pillar fabrication trials and the method employed currently is the use of etching, specifically RIE. Etching is used to permanently transfer the topographically imprinted pattern from a mask material (most commonly photoresist or metal) onto the surface of the substrate [85]. In nanofabrication this can be achieved either through a wet chemical etch or a dry plasma etch. The chosen method is determined by the desired etch profile for the final substrate, as seen in Figure 2.4. Wet etching is often the simplest form of etching as it uses an etchant solution, usually an acid, to chemically attack the underlying surface while leaving the mask intact. This method leads to isotropic etching which causes undercutting beneath the mask’s surface in a nondirectional manner [85]. The wet

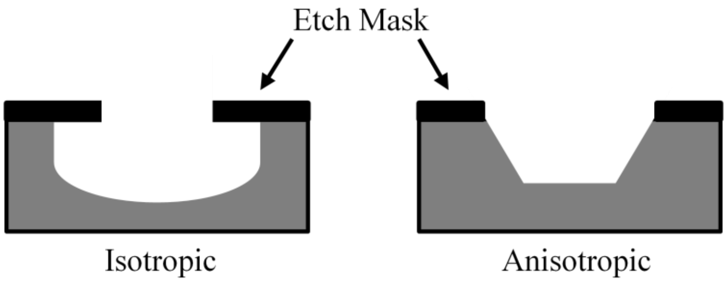

Figure 2.4: Example of different etch profiles for chemical and physical etches.

chemical etch is also a slow process and possesses little control over position and direction. Wet etching is not commonly used in nanofabrication for these reasons. Most nanofabrication requires anisotropic etch profiles instead since they produce sharp, controlled features.

Dry plasma etching utilizes an ionized gas (plasma) instead of a liquid etchant. An electric field accelerates the ions toward the wafer. The resulting etch is a combination of chemical etching, from the film reacting with the plasma, and physical sputtering, from the directional bombardment of the ions as they hit the wafer [85]. The chemical aspects of the process yield good etch selectivity, *i.e.* the ratio of the substrate etch rate to the mask etch rate, for a variety of materials. This type of etch is still essentially isotropic. Physical sputtering, however, is highly directional and leads to extremely vertical features with poor etch selectivity. Thus, most plasma etching combines the two processes to achieve a finished product that is both selective and directional. Several different techniques provide quality results for nanofabrication with RIE being the most common.

A schematic of an RIE system is shown in Figure 2.5. The substrate is placed within a reactor in the RIE system. Reactive species are generated in a plasma using an RF power source and a specific gaseous mixture. Ions are then accelerated toward the substrate surface leading to both physical and chemical etches. The physical process is from high energy ions that knock atoms out of the substrate surface through a transfer of kinetic energy. The chemical process occurs with the formation of gaseous material at the surface of the substrate, causing a similar result as a wet chemical etch. The etch profile and etch depth can be controlled by various parameters [66]. The specific types of

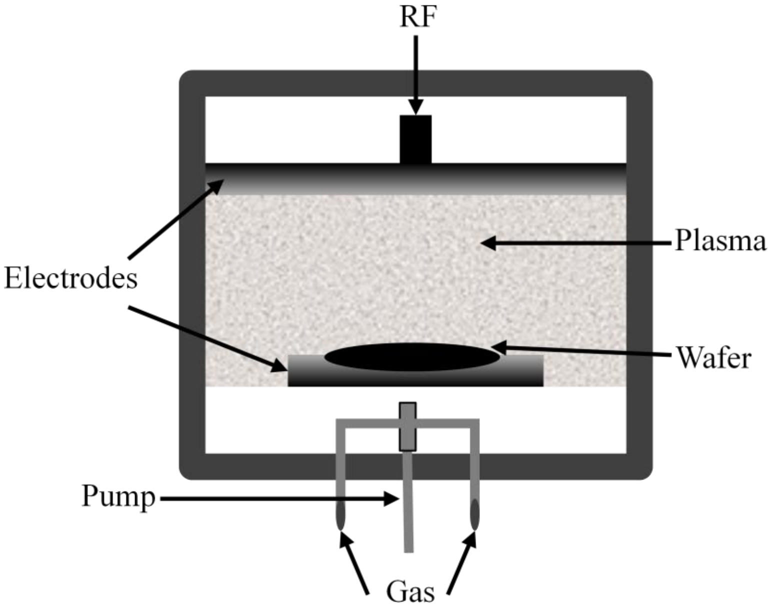

Figure 2.5: Schematic of RIE chamber.

gases and the amount of each type, as well as gas flow rate, help determine how aggressively the chemicals interact with the substrate. RF power, etch time, and chamber temperature all contribute to whether the chemical or physical etch process dominates.

The RIE etch processes used in this work have involved a variety of gas combinations, most involving fluorine containing compounds. The etch time has also been altered frequently in the hopes of identifying the optimum height for the SERS substrates (pillars) in question. More specifics as to the final structures and the parameters that created them will be discussed in subsequent sections.

Chapter 3

Controllable Nanofabrication of Aggregate-Like Nanoparticle Substrates and Evaluation for Surface Enhanced Raman Spectroscopy

Chapter 3 is an adaptation of a research article published in *ACS Nano, 2009, 3, 3845-3853*. This article discusses a novel combinatorial approach to improving SERS substrate fabrication and analysis. Coauthors include Jenny Oran, who developed the first random morphology substrate designs, and Scott Retterer, who helped develop the electron beam lithography and liftoff process used in the fabrication of the many substrates. This chapter has been revised as the Experimental section originally came at the end of the work and now follows the Introduction.

3.1 Introduction

Surface Enhanced Raman Spectroscopy (SERS) is a valuable analytical phenomenon that can result in a dramatic increase in Raman signal from molecules that have been sorbed onto or are in the vicinity of nanometer-sized metallic particles. There are two accepted mechanisms, chemical and electromagnetic, that are generally recognized as being responsible for the observation of the SERS effect [21, 86].

Chemical enhancement mechanisms are dependent upon both analyte molecules adsorbed to the SERS substrate surface and the nature of the metal surface itself, in some cases creating a charge transfer intermediate state to increase Raman signal [87].

Electromagnetic enhancement is more general in nature and is typically not critically dependent upon the analyte used. It can be seen in SERS when substrates are made of roughened metal surfaces or nanoparticles, typically gold, silver, or copper, that have features smaller than the wavelength of light being used [26, 27, 88]. When electromagnetic radiation impinges on the metal composing the SERS substrate, conduction band electrons undergo oscillations of frequency equal to that of the incident light. These oscillating electrons produce surface plasmons at/near the metal surface [89]. The resulting secondary electric field adds to the incident field. Thus, localized surface plasmons have the ability to enhance the electromagnetic field in the area near the nanoparticles composing the substrate, leading to greater Raman signal enhancement for analytes located therein. Similarly, the Raman scatter can be amplified by the substrate. The SERS effect is highly dependent upon nanoparticle shape and structure as it relates to the excitation wavelength and the dielectric properties of the medium [28, 30, 44]. As a result, recent research [90-92] has focused on taking advantage of the electromagnetic enhancement mechanism of SERS by engineering substrates with both random and controlled morphologies that can be used to tune the observed surface plasmon resonance to suit the experiment.

Perhaps the most common type of SERS substrate, one that consistently yields large signal enhancement, is simple colloidal gold or silver nanoparticles having the size range of 10-150 nm [49, 93]. Usually these are formed by the reduction of metal salts, e.g., the reduction of silver nitrate with sodium citrate. In some cases, the reduction is accomplished in more careful fashion to create cubes, rods, or triangular structures [50]. The colloidal systems that are most often used for single molecule or otherwise ultra-sensitive detection are usually aggregated clusters that possess some “hot spot(s)” within certain aggregates. Research has shown “hot” aggregates can contain as few as two to six [93] tightly packed particles and be as large as greater than 20 particles [55]. Much research has been done using colloidal substrates to support the finding that nanoparticle density plays a role in Raman signal enhancement [51, 52, 55, 94, 95]. In one study by Khan, *et al.*, the effects of aggregate size/nanoparticle density on surface enhanced resonance Raman scattering (SERRS) signal was examined [55]. Ag colloid solution was evenly distributed across the surface of a transmission electron microscopy (TEM) grid, and SERRS data was collected and correlated with TEM images. The results showed that as nanoparticle density increased, SERRS activity increased. Regions of the grids that contained large aggregates showed the most intense SERRS signal, while regions with few particles were the least intense [55]. Another study by Camden, *et al.*, focused on the correlation between nanoparticle structures known to yield single molecule SERS, wherein several active aggregates were identified [56]. The results showed that hot spots likely occur at particle-particle intersections. A focus was made at studying a simple dual particle aggregate composed of a hemispherically capped rod and a sphere with a T-shape that yielded single molecule sensitivity [56]. While well-designed, random morphology substrates may lead to improved SERS enhancement, it is difficult to synthetically reproduce the nanoparticle aggregates that have been found to yield large SERS signal. One alternative to colloid is metal island film substrates [96]. The advantages of this type of substrate over colloid-based substrates include better reproducibility from spot to spot and ease of fabrication. However, these substrates have yet to generate the signal enhancements of the best performing colloidal systems.

Previous work in our group, has demonstrated electron beam lithography (EBL) techniques for the definition and fabrication of nanostructured SERS substrates [81, 97, 98]. With EBL, the morphology of the SERS-active substrate can be controlled since the nanoparticles composing the substrate are chosen and laid out using computer aided design software [81, 92, 97-99]. Also, EBL remains an important technique for fabricating uniform, reproducible substrates. Recently, we found that substrates made of ordered arrays of ellipses having aspect ratios of 300:300 nm and 300:250 nm gave better SERS enhancement than smaller, prolate ellipses (6:1 to 6:4) [98]. We have also performed research with synthetically produced, random shaped aggregated colloid and colloid shaped as cubes that have yielded good SERS enhancement as well [100]. Along those lines, our focus herein is to combine the two approaches to substrate creation and fabricate combinatorial sets of SERS substrates comprised of random patterns that can be *spectrally mapped and reproduced* based on their demonstrated enhancement.

To this end, we borrow from the biomedical concepts of combinatorial chemistry and cloning and demonstrate a novel EBL-reactive ion etching (RIE) approach to the combinatorial fabrication of SERS substrates. The substrates are arranged in 10x10 matrices composed of randomly different 5x5 μm cells of Lithographic Defined Nanoaggregates (LDNAs) and inspected for SERS activity using benzenethiol (BT) as a test compound. We combine the randomness of colloidal aggregate substrates with the ability of the EBL system to reproduce substrate morphology by designing arrays containing aggregates made up of different shapes ranging in size from approximately 75- 650 nm. Herein, we describe the process we used to create these LDNAs, as well as the combinatorial approach to determine the best performing aggregates. Experiments were also completed to examine reproducibility of both the aggregates, in addition to the SERS signals they produce. Finally, an experiment was used to inspect the ability of our substrates to be cloned over large areas while remaining uniform, intense SERS active in the process.

3.2 Experimental

3.2.1 Instrumentation

All SERS spectra were collected using a JY-Horiba LabRam Spectrograph. Details of the instrument setup have been described previously [101, 102]. In general, a 50X (0.45 NA, ∞) microscope objective was used to deliver 0.67mW of the 633 nm line of a thermoelectrically cooled HeNe laser with a spot size of approximately 5 μm. All spectra were collected with a 180° scattering geometry and sample acquisition times were set to 1 second unless otherwise stated. The polarization vector was vertical in the plane of the substrate arrays in all cases. Normally SERS spectra are manually corrected for the broad background scatter using the LabSpec 4.12 software of our Raman system.

3.2.2 Preparation of SERS-Active Substrates

As described above, 50x50 μm patterns containing different shapes of varying sizes (see appearance in Figure 3.1a), randomly positioned in the array to form 5x5 μm cells, were created in AutoCAD 2005. These arrays were formed with either various

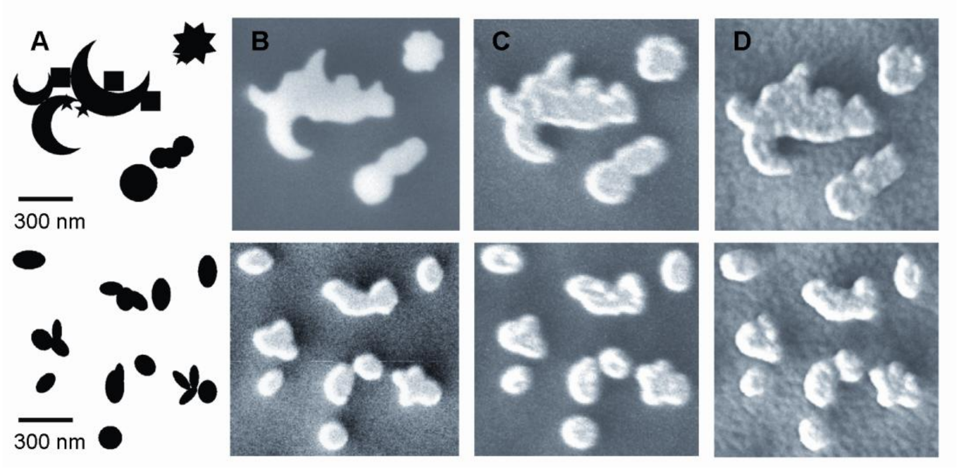

Figure 3.1: (a) Images of CAD of a various shape pattern (above) and circle/ellipse pattern (below) and SEMs of (b) EBL patterns following 250 nm deep RIE, (c) EBL patterns after deposition of 20 nm of SiO2, and (d) deposition 40 nm of Ag.

shapes or different circles and ellipses to create the pattern types seen in Table 3.1. The patterns were each created by selecting the types of shapes as well as the sizes to use for that pattern. Subsequently, individual shapes were manually inserted into a 50x50 μm CAD square in a random, blind fashion until a predetermined overall average density (percent coverage/5x5 μm cell) was reached. Some manipulation of the CAD patterns was performed so that the larger CAD square was partitioned into 100 smaller 5x5 μm cells that roughly match the laser spot size.

Once a strong performing "hot" cell was pin-pointed via SERS data collection – described below, that 5x5 μm cell was found in the original AutoCAD drawing and cloned into a macro-pattern in the shape of a "T" (called "cloned cell "T" pattern). The AutoCAD drawings were then converted to GDS-II format by using the LinkCAD conversion program. The files were transferred to the EBL system computer and converted to the format readable by the instrument.

3.2.3 Liftoff Pillar Method

A 2-in Si wafer (Wafer World, FL) was baked for 45 minutes at 250˚C to remove any excess moisture adsorbed onto the surface. A 300 nm film of Zep 520A, a high resolution positive tone resist suspended in anisole, was applied to the wafer using spin coating at 6000 rpm for 45 s. Once coated, the wafer was then baked at 180˚C for 2 minutes and placed under vacuum in EBL system. The resist film thickness was estimated from a chart provided by the manufacturer based on spin rate.

Table 3.1: General morphological data on the 8 different types of tested matrices.

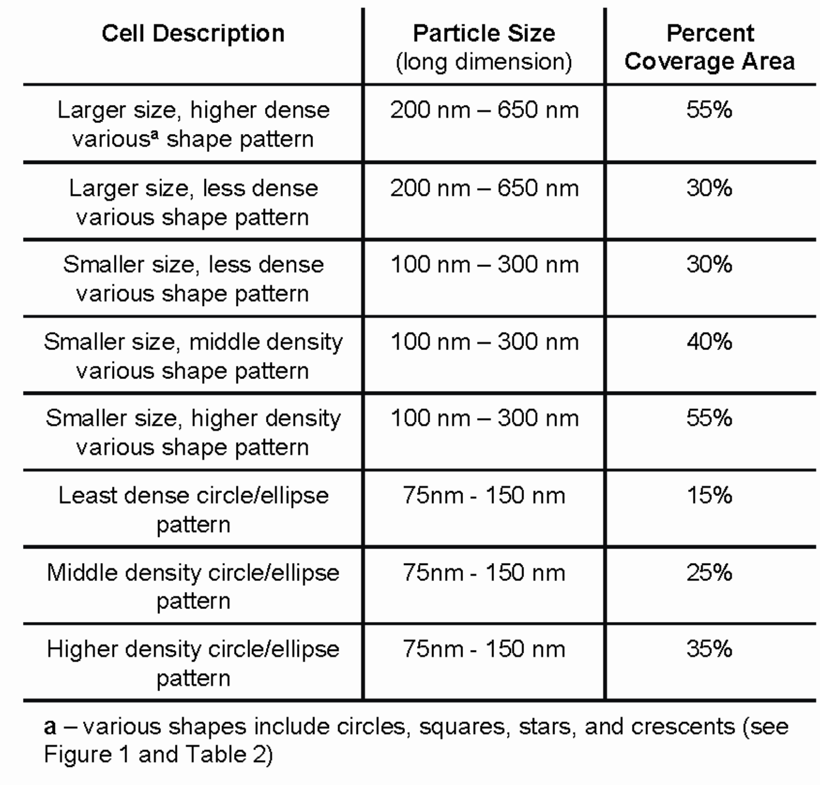

Cell Description	**Particle Size** (long dimension)	**Percent Coverage Area**
Larger size, higher dense various[a] shape pattern	200 nm – 650 nm	55%
Larger size, less dense various shape pattern	200 nm – 650 nm	30%
Smaller size, less dense various shape pattern	100 nm – 300 nm	30%
Smaller size, middle density various shape pattern	100 nm – 300 nm	40%
Smaller size, higher density various shape pattern	100 nm – 300 nm	55%
Least dense circle/ellipse pattern	75nm - 150 nm	15%
Middle density circle/ellipse pattern	75nm - 150 nm	25%
Higher density circle/ellipse pattern	75nm - 150 nm	35%

a – various shapes include circles, squares, stars, and crescents (see Figure 1 and Table 2)

A Jeol JBX-9300 FS/E EBL system with a 100 keV thermal field emission gun was used for the writing of the nano-arrays. The resist film was exposed to a dose of 420 μC/cm^2 for fabrication. Each 50x50 μm pattern was spaced 200 μm apart in both the x and y directions yielding evenly spaced rows of unique patterns. Each row has similar features while each column has varied individual patterns. When exposure was complete, the patterns were developed using xylene for 30 s, rinsed with isopropyl alcohol, and dried. Wafers were then exposed to an O_2 plasma for 6 seconds at 100 Watts (Technics Reactive Ion Etching System) to remove resist residue on the patterns after development.

For the liftoff process, 10 nm of chromium were then deposited onto the surface of the wafer using an Electron-beam dual gun evaporation chamber (Thermonics Laboratory, VE- 240). The excess resist and chromium were then removed via liftoff using an acetone bath followed by an isopropyl alcohol rinse. The wafers are then rinsed with deionized water and dried. The patterns are then etched using an Oxford RIE to a pillar height of 250 nm at a rate of 100 nm/min (see appearance in Figure 3.1b). After the etching, the chromium was removed using a chromium photomask etchant, Cr-14S, bath for 20 minutes. Finally, 20 nm of SiO_2 were deposited onto the silicon surface using an Oxford Plasma Enhanced Chemical Vapor Deposition (PECVD) system at a rate of 1.2 nm/s (see appearance in Figure 3.1c).

Substrates were made SERS-active by deposition of 99.999 % Ag (Alfa Aesar, MA) using a physical vapor deposition (PVD) chamber from Cooke Vacuum Products, Inc. Samples were mounted 25 cm above and normal to the effusive source. Average mass thickness and deposition rates were monitored for each film using a quartz-crystal microbalance (QCM) mounted adjacent to the substrates. The SiO_2 patterns were coated with varying amounts of Ag at differing deposition rates depending on the study being done (see appearance in Figure 3.1d).

Scanning electron microscopy (SEM) images were collected with a Jeol JSM-7400F microscope with a field-emission gun operating at a range of 1.50-5.00 kV depending on the substrate surface. Sample damage and charge build-up were reduced under these conditions to yield high-resolution images of Ag-coated and uncoated surfaces.

3.2.4 Analyte preparation and data acquisition

The analyte used in most studies was $1x10^{-5}$ M BT (99%, Fisher), in 18 MΩ deionised water (Barnstead, E-Pure) which formed a well defined self-assembled monolayer (SAM) on the metal surface. Details of how data was collected and processed have been described previously [47, 101]. The wafer containing the rows of patterns was placed at the bottom of a plastic Petri dish that was filled with approximately 2 mL of BT solution for 15 minutes before being rinsed with deionized water and dried. SERS signal was optimized by fine-focusing the microscope objective, and the spectroscopic data was collected by rastering the laser beam across each pattern at 5 µm intervals (1 spectral acquisition per step) over a 4900 μm^2 area (N = 196). In some studies, a previously described sample translation technique (STT) [101, 102] was used, while other test analytes were sometimes used, as well. It should be noted that the laser spot jitter on our nanofabricated samples is estimated to be 1-2 µm and was influenced by construction near our laboratory.

3.3 Results and discussion

3.3.1 Spectral mapping of initial aggregate arrays

EBL patterns were made from randomly arranged, computer generated, arrays of differing nanoparticle shapes. An array in this work is defined at the individual particles that are laid down onto the computer template. These arrayed shapes formed 5x5 μm cells, containing either (i) various shapes (stars, crescent moons, etc.) or (ii) eight different circles and ellipses, each of which are of assorted sizes totaling different coverage areas (see Table 3.1 for details). The cells were formed into 5x5 μm squares to approximate the laser spot size. Circles/ellipses were chosen to mimic the nanoparticle shapes in the hot aggregates that form via colloid reduction (although more disk like than true synthetic colloids) [55, 93]. The various shapes were chosen to produce structures with sharper features. However, as seen in Figure 3.1, the nanofabrication processes tend to round-out the sharper features. These arrayed cells form the overall 50x50 μm patterns (a 10x10 matrix that contains 100 morphologically different cells) that are surveyed for SERS signals in these experiments.

In order to determine whether an original aggregate array contained areas of substantial enhancement, the array was spectrally mapped and the SERS signals obtained from the SAM of BT [103, 104]. 25 nm of Ag was deposited onto the different patterns at a rate of 1 Å/s. It was determined that depositing a layer of SiO_2 on the wafer prior to depositing the Ag, thereby altering the dielectric properties of the substrate, substantially improved signals [105]. Initial experiments showed that 20 nm of SiO_2 was optimum for dielectric aspects without appreciably distorting the sharp features of the EBL. In every initial 50x50 μm pattern, the best and worst performing of the 100 individual 5x5 μm cells were determined. Each individual analysis was then compared with other trials using the same parameters, including the substrate pattern type. In general, there were individual cells, or regions of cells, giving consistently high signals in each of the initial trials. Figure 3.2 shows the analysis of the least dense circle/ellipse pattern with a corresponding hot region in the lower right corner of the substrate. While the two hot areas seem to be in the same overall region, it is difficult to determine from the full 50x50 μm pattern spectral mapping experiment whether the two hot cells are identical. This is due to instrument limitations, in particular not being able to start the rastering analysis in exactly the same spot for each trial. To obviate this limitation we use an additional, more confined, spectral mapping experiment to pinpoint the hottest cell(s). The process is discussed in the following section.

It is also obvious from looking at Figure 3.2 that no discernable signal occurs outside of the 50x50 μm pattern. As shown, the "hot" region was not only located in the same area in both trials, the signals were almost identical. Strong performing cells were generally determined from the magnitudes of the 1056 and 1575 cm^{-1} bands. There are small relative differences in spectral features, as some minor bands are stronger in certain cells than others, presumably due to the random nature of the substrates or trace impurities. In this case, the signal for the single best cell in each pattern was roughly 5 times stronger than the average signal for the entire pattern and over 10 times higher than the lower performing cells. This showed that a hot region was present in the original pattern, as well as present in each of the low density circle/ellipse patterns tested.

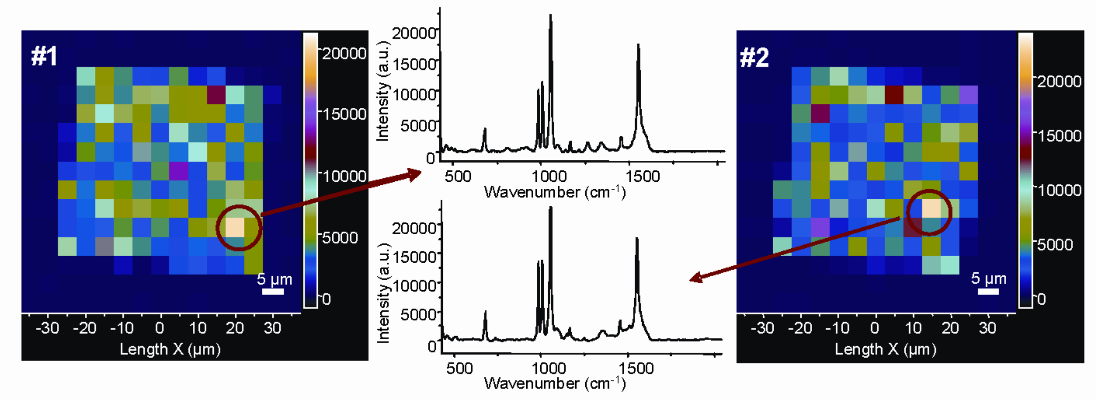

Figure 3.2: Combinatorial-like SERS signal survey of two 50x50 µm patterns of the least dense circle ellipse type of pattern. The spectra of BT for the apparent best 5x5 µm cells are shown.

This general procedure for determining hot regions was followed for all pattern types presented in Table 3.1. Through analysis, it was determined that the circle/ellipse patterns had an overall higher signal than the various shape patterns. Counter intuitively, those patterns with lower overall surface area performed better than those with greater area. Table 3.2 shows a portion of the CAD for the best cell of each pattern type, as well as the top and bottom three performing cells' signal heights at the 1056 cm^{-1} band. As illustrated in Table 3.2, the highest to lowest signals range by more than a factor of 44 in signal height. There is clearly a wide range in signals in even the same pattern. This can be attributed to the fact that the structures are random in nature. As such, some of the cells could be much "hotter" than any other part of the pattern. Therefore, determining the best performing cells in a given pattern is paramount to potentially creating reproducible structures with overall uniform strong enhancement. The process for doing so is addressed in the next section.

The circle/ellipse patterns consistently gave signal at a higher intensity than the various shape patterns. Also, the lower density patterns had better performing hot spots than the higher density substrates. The overall best performing substrate, the low density circle/ellipse pattern, had only approximately 15% coverage of each 5x5 μm cell. Previous EBL substrate work from our group indicated that the substrates with denser surface coverage had higher overall enhancement [81, 97, 98]. However, the prior work did not involve RIE to create pillars of Si and subsequently the creation of a layer of SiO_2. We suspect that the continuous layer of 25 nm Ag over the SiO_2 may be a factor, and experiments are planned to investigate this possibility. Note that Chumanov and

Table 3.2: Results of combinatorial-like SERS signal surveys of the 8 different types of tested matrices.

Cell Description	CAD Appearance	Signals	
		Highest	Lowest
Larger size, various shape pattern	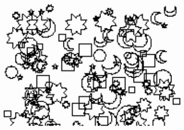	11196 10441 8703	766 435 976
Larger size, less dense various shape pattern		16757 4623 4732	504 727 841
Small size, less dense various shape pattern	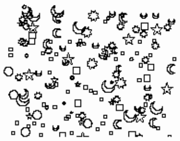	10488 7690 8332	1512 1557 1643
Small size, middle density various shape pattern		6583 7182 6583	1438 1244 1418
Small size, highest density various shape pattern		5677 3586 4127	508 629 625
Least dense circle/ellipse pattern		22295 13610 12254	2226 2266 2164
Middle density circle/ellipse pattern		13644 10066 8980	1278 1392 1527
Highest density circle/ellipse pattern	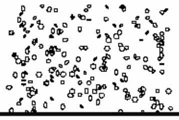	20055 19524 11668	1058 1196 1272

coworkers have observed interesting coupling between continuous metal films and plasmonic particles [106, 107].

3.3.2 Combinatorial cell survey

After initial analysis, it was determined that the pattern types of focus for further inquiry would include the larger size, less dense various shape pattern and the low density circle/ellipse pattern. They each gave large signal, while also having hot regions located in the same general area of the 50x50 μm pattern for each initial trial. To determine which of the 5x5 μm cells was actually giving the large signal, we conducted a more confined spectral mapping experiment. To pinpoint the hot cell, a 3x3 cell matrix of the suspected hot cell region was created. This small 15x15 μm pattern helped determine the correct hot cell due to its small size and ease of reproducibility. Since there are only nine potential cells, the possibility of accidentally misdiagnosing which of the cells is giving the greatest signal is minimized. When looking at the cells in the original 50x50 μm pattern, there is a chance of the best region's signal being obscured with the surrounding cells based solely on size of the substrate and limitations of the Raman instrument. As shown in Figure 3.3 (a and b), the 9 cell array confirms that the hottest point is in the same place as seen in the original array.

After determining the best individual cell, the entity was then broken into quartered sections, each 2.5x2.5 μm. By splitting the hot cell into individual parts, we can determine if there is uniform signal throughout the overall cell or if just a part of the whole is responsible for the majority of signal intensity. As seen in Figure 3.3 (c), the quartered sections yielded quite different signals. This shows that the individual

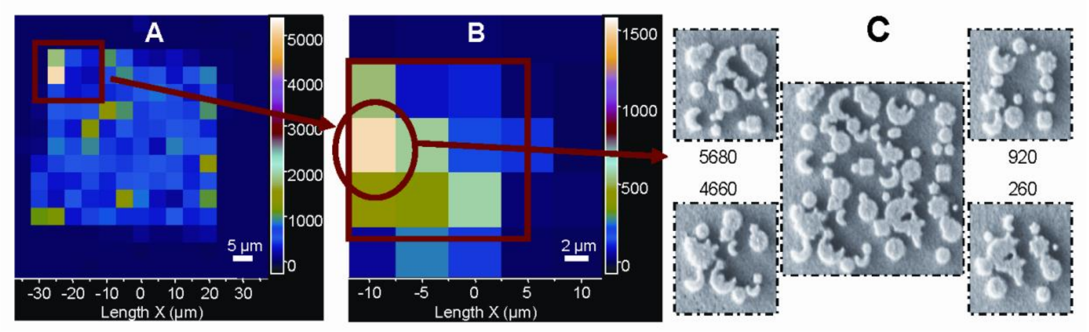

Figure 3.3: Combinatorial-like SERS signal survey (BT analyte) of (a) 10x10 cell original matrix, (b) a 3x3 cell matrix containing an apparent good cell, and (c) sub-dividing the good cell (SEMs and SERS signal heights from 2.5 μm square quarters); focusing on discovering good performing morphologies.

aggregates are capable of giving signal enhancement large enough to affect the overall signal of the entire, larger cell. Furthermore, as the SEM images show, the EBL process is capable of creating aggregates repeatedly that are similar in nature. Each of the four corners of the original bears a close resemblance to the quartered aggregate corresponding to it.

3.3.3 Reproducibly cloned arrays

Once the top performing cell had been identified, the next step was to show that the EBL process can be used to reproducibly clone arrays of similar cells, both in appearance and performance. The top performing cell out of the low density, circle/ellipse patterns and a modest performing cell out of the larger size, various shape pattern were selected and a relatively large 120x120 μm square pattern was cloned with the best performing aggregate forming the shape of a "T" in the center. Figure 3.4a shows an optical image taken by our Raman instrument of what the array looks like. The pattern was then analyzed by raster mapping as done in the previous trials. Figure 3.4b shows the actual mapping of the cloned cell "T" pattern substrate. As shown, the inner part of the "T" seems to be uniform in signal while the outer part also seems to be a uniform color, indicating similar signal intensity. After analysis, the inner part of the pattern had an average signal band area of over 97,000 at 1056 cm^{-1} with an RSD of slightly less than 30%. The outer region had an average signal area of only 23,000 at the same band with an RSD of approximately 31%. In general a modestly performing cell tended to yield somewhat higher signals when cloned into larger areas than when it exists as a unique cell in a diverse morphology array.

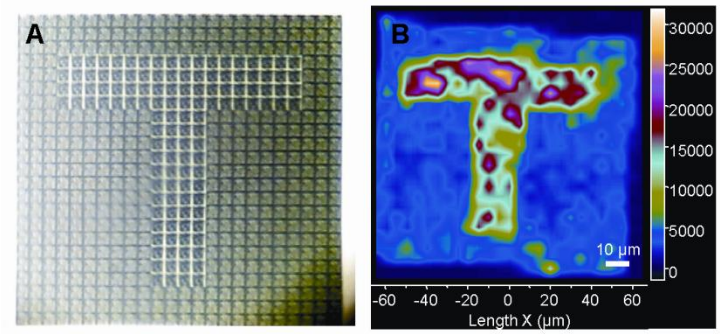

Figure 3.4: Demonstrated ability to clone hot cells into macro-patterns. (a) An image from an optical microscope where the inner "T" is a cloned cell from a high performing cell and the outside is from a modest performing cell. (b) Map showing uniform enhancement from both the outer and inner regions.

This particular pattern shows several advantages of the EBL process for SERS substrate fabrication. First is the ability to create reproducible aggregates that give uniform signal. Even though there are some uncertainties associated with enhancement factor (EF) calculations [108], it still remains one of the ways to evaluate the SERS activity of a substrate or portion of a substrate. With this in mind, we attempted to calculate the EF for the inner part of the "T" region. A common procedure [109] that employs Equation 3.1 for the SERS EF calculation was used:

$$\boldsymbol{EF(1575\ cm^{-1}) = \left(\frac{N_{vol}I_{surf}}{N_{surf}I_{vol}}\right)} \tag{3.1}$$

wherein I_{vol} and I_{surf} were the signal areas under the 1575 cm^{-1} peaks for neat BT (Raman standard) and a SAM of BT (SERS), respectively.

Knowing the laser spot size of our 50x microscope objective (~5 μm) and using the average area covered by the individual cell (15%), we calculated the total surface area of the nanoparticles and multiplied it by the known packing density of BT (6.8x10^{14} molecules/cm^2) [110, 111]. This yielded the maximum surface number density (N_{surf}) of the adsorbed molecules that lead to the SERS signal. Neat BT was used as a Raman standard in a glass capillary. The volume of the area in question was found to be 29.5 nL. Using the density of BT (1.073g/mL) in the neat BT calculation, the number density (N_{vol}) was found to be 1.74x10^{14} molecules. With the above information, the average EF for the inner part of the "T" was calculated to be 3x10^8 with several cells giving enhancement of 5x10^8.

It has been shown in previous work involving single molecule SERS (SMSERS) [24, 25, 112], that electromagnetic EF can approach 10^{11}. While of great significance in

SMSERS, these active "hot spots" with exceptional EF represent only a minuscule percentage of the total substrate area. When comparing the enhancement of a single molecule, it has been shown that the enhancement can be as much as 10^7 times greater than the average enhancement of the entire substrate [56]. From a trace analysis standpoint, this can be a significant analysis limitation as the trace analyte must find the appropriate location on the substrate. In our approach, however, we were able to produce an enhancement of 5×10^8 for a large area metal surface. Although Figure 3.3c clearly indicates the enhancement is not uniform over the entire LDNA metal surface, it is observed that when moving the interrogation laser spot over the entire substrate the average enhancement does not deviate appreciably (note: RSD of ~ 30%). While we do not demonstrate a single aggregate with enhancement approaching theoretical limits, it is possible to create a substrate with high enhancement over relatively large areas (note: hot cells can be cloned at a rate of roughly 0.1 mm^2/min with our system).

3.3.4 Analytical figures of merit with cloned LDNAs

The benefits of a large substrate area also extend into an ability to improve on many figures of merit including reproducibility. One method for improving is altering the way the substrate is analyzed. When laser exposure is increased, the potential for larger signal and better sensitivity increases. However, one issue that can arise is sample photodegradation and substrate damage when a large laser power is used [101, 113]. One way our group has addressed this problem involves using a STT wherein the analyte baring substrate is spun under the focused laser beam to reduce the effective duty cycle of irradiation [101]. As such, the ability to use higher powers and long acquisition times without damaging the sample or the substrate leads to improved limits of detection and sensitivity. Moreover, inhomogeneity in the substrate is averaged out with the STT approach [101]. Large area cloned LDNAs and the STT appear to be a well suited match.

Using the same cells as used in the inner part of the cloned “T” array, a large 300x900 μm array was created. For these experiments, the usual settings of a 1 second acquisition with a laser power of 0.67 mW were altered to accommodate harsher conditions. Using this large region, STT was used to analyze the substrate. Translation of the sample was achieved by spinning the substrate at a rate of approximately 2000 rpm and optically interrogating. While spinning, the average signal of each concentric ring was acquired. This process allows the acquisition time to increase without damaging the substrate or degrading the analyte in the process. Using $5x10^{-7}$ M rhodamine 6G (R6G), a comparison of the reproducibility of STT and a stationary substrate using a 10 second acquisition time at the 0.67 mW power was investigated. As seen in Figure 3.5a, the spectra for the STT analyses were not only similar; they produced an RSD of 6.6% for the 1499 cm^{-1} band. The stationary acquisition, however, produced an RSD value of 22% on this substrate for the same band. While the stationary raster approach is fairly reproducible as far as SERS analysis goes, using the STT allows excellent reproducibility.

The large substrate allows for much harsher conditions than would be possible using SMSERS experimental protocols. The same cloned arrays were exposed to a laser power of 2.7 mW. Using both the STT and a stationary raster, $5x10^{-7}$ M R6G was analyzed with various acquisition times ranging from 1 second to 30 seconds. As seen in Figure 3.5b, there is a large difference between the spectra of the STT and stationary acquisitions. Initially, the 1 second acquisition time for each technique is strikingly

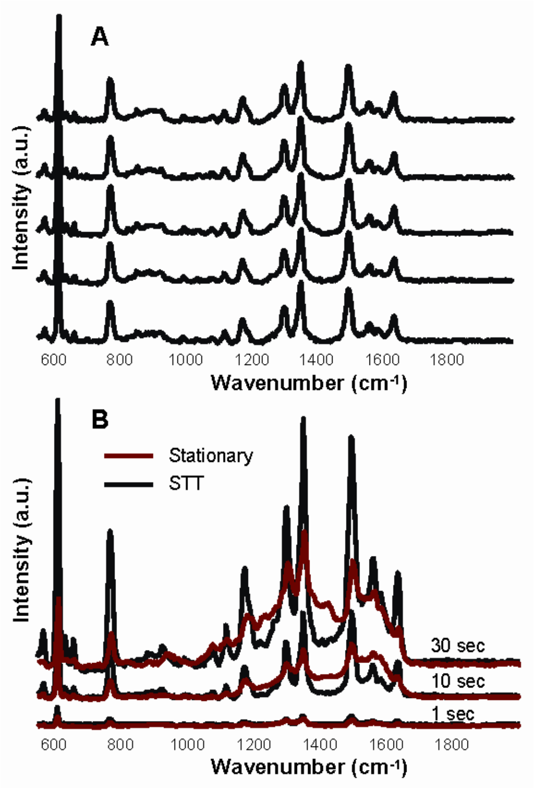

Figure 3.5: (a) Comparison of spectra for R6G during one trial of extended regions of cloned cells and employing STT with incremental increases in spinning radius of about 5 μm each for the spectra and demonstrating very good reproducibility. (b) Spectra indicating the analytical improvement in S/N by virtue of using the STT approach, over single point measurements, by increasing acquisition times with R6G as the analyte.

similar. However, when using a 10 second acquisition time, the intensity for the STT starts to outpace the stationary technique. Also, some of the bands start to show signs of degradation with concomitant carbonation formation (see broad region from 1000-1600 cm^{-1}) [101]. By the time the 30 second acquisition times are used, the difference between techniques is even more pronounced, with many STT bands subsequently more intense than those of the stationary raster. Also, the broad carbonation bands with the stationary raster have obscured the R6G bands almost completely while the STT spectrum is still distinct. Large area LDNAs substrates, therefore, have the ability to withstand harsh conditions without degrading due to the potential of alternate analysis techniques. This is expected to translate into improved calibration plots with lower limits of detection. These improvements correlate to an average signal intensity height of 13375 at the 602 cm^{-1} band with a 30 second acquisition time using the STT, more than 28 times better than the 1 second stationary raster.

3.4 Conclusions

In summary, while colloidal deposition can achieve individual aggregates with large SERS enhancement, the ability of EBL to reproducibly fabricate high-performing pseudo-aggregates makes it an attractive approach for substrate creation. Moreover, through the use of EBL, we were able to consistently identify the “hot” regions (cells) on multiple fabrication attempts. Through a combinatorial-like, spectral mapping approach to “hot” cell identification, it was not only possible to locate an individual cell capable of high signal intensity, but also dissect the individual cells to further study morphological features leading to SERS enhancement. Using the cells denoted as the best performing, we are able to clone large arrays that yielded electromagnetic enhancement of 5×10^8 with good uniformity, providing improved analytical capabilities by mating with STT. While more straightforwardly-created, non-lithographic substrates such as metal films over nanospheres can achieve enhancements of 1×10^8 over relatively large areas [114, 115], we contend that by dissecting cells more acutely (as see in Figure 3.3), and/or exploring additional nanoparticle shapes and sizes, extended LDNA surfaces may be fabricated with uniform enhancements significantly better than the 5×10^8 reported herein.

3.5 Acknowledgements

This research was supported by the U. S. Environmental Protection Agency STAR Program under grant EPA-83274001 with the University of Tennessee. The nanofabrication portion of this research, conducted at Oak Ridge National Laboratory's Center for Nanophase Materials Sciences, was sponsored by the Scientific User Facilities Division, Office of Basic Energy Sciences, U.S. Department of Energy.

Chapter 4

Efficient Disc on Pillar Substrates for Surface Enhanced Raman Spectroscopic Analysis

Chapter 4 represents an earlier more comprehensive version of a research article ultimately published in *Chemical Communications, 2011, 47, 3814-3816*. This version discusses the fabrication and subsequent analysis of a simple but effective SERS substrate. Coauthors include Alessia Polemi and Kevin Shuford of Drexel University who conducted the theoretical modeling discussed. Also, Nickolay Lavrik contributed to both theoretical modeling and initial determinations of parameters to adjust for optimum enhancement. As this is an earlier version, a large amount of text from each section was removed before the final accepted manuscript. The largest changes occur in the analysis of arrays and a more in depth look at analytical analyses. The rest of the changes resulted mostly in abbreviated descriptions and are more trivial in nature.

4.1 Introduction

Surface Enhanced Raman Spectroscopy (SERS) is a technique which allows for the determination of molecules that are on or near the surface of a roughened metal surface [21, 44, 87]. SERS is analytically useful due to its ability to identify the "fingerprints" of given analytes coupled with much higher sensitivity than conventional

Raman spectroscopy. There are generally two accepted mechanisms responsible for the SERS effect; chemical and electromagnetic enhancements [21, 86]. Chemical enhancement is the lesser in magnitude of the two and is reliant upon both the analyte molecules adsorbed onto the surface and the metal surface itself [20, 87].

Electromagnetic enhancement, however, is widely regarded as the dominant factor in determining SERS signals and not typically dependent on the analytes involved [18, 26]. When a roughened metal surface, or nanoparticles, with features smaller than a wavelength of light are used, electromagnetic radiation impinging on the SERS substrate causes conduction band electrons in the metal to oscillate at frequency of the incident light [26, 27, 88]. These oscillations produce surface plasmons at or near the surface of the metal that can be very intense, leading to substantial SERS signal enhancement for analytes located therein [89]. Also, the SERS enhancement is highly dependent on the nanoparticle size, shape, and structure with relation to the excitation wavelength and dielectric properties of the substrate [30, 44, 116, 117]. As such, research has focused on generating substrates, both random and ordered, with the ability to tune the observed surface plasmon resonances to the experimental setup [90-92].

SERS substrates can be divided into two general classes, random and engineered [118]. Random substrates are by far the most common and include simple aggregated colloidal gold or silver with particle sizes ranging from 10-150 nm [49, 93], often formed by the reduction of metal salts. Oftentimes, these random aggregates have particularly small interparticle separations, which can lead to large SERS enhancement factors (EFs) of 10^{12} or greater [42], in some cases allowing for single molecule detection. Roughened metal surfaces [19] and anisotropic metal nanoparticles [119] are also commonly used.

The benefit of these random substrates is the ease of fabrication and the high signal enhancements which can result in single molecule detection. Unfortunately, the random substrates have limitations due to a lack of reproducibility. One generally does not know where a “hot spot” will arise in these substrates and generally a miniscule fraction of the substrate exhibits large enhancement [120, 121].

As such, engineered substrates have become more common over the last several years. Techniques including metal island films [122], metal film over nanospheres [115], and holes in metal films have increased in popularity due greater reproducibility [123]. Unfortunately, these approaches have not routinely achieved an enhancement nearing that of the random aggregates. Other popular techniques involve various types of lithography. As far back as the early 1980’s, a group from Bell Labs pioneered the use of electron beam lithography (EBL) to controllably fabricate ordered nano-pillar-arrays [124]. Current lithographic efforts at creating suitable SERS substrates are summarized in the recent review by Haynes, *et. al* [125]. Our group has shown EBL has the ability to produce both ordered and random substrates with high reproducibility [97, 98, 126, 127]. Initially, it was shown that substrates using many ordered arrays of ellipses having varying aspect ratios could provide adequate EFs [98]. Follow up research focused on using shapes with many sharp features (*i.e.:* stars, squares, moons, etc.) and circles and ellipses of various sizes and shapes, both arranged in a random fashion [127]. This work demonstrated certain unexpected observations including that the circle and ellipse substrates consistently outperformed the ones with sharp features and the best performing substrate was the least dense (smallest nanoparticle surface area) of all the types studied [127].

Concomitant with the experimental work, an ability to computationally model the given substrates is of upmost importance to understanding why certain structures perform better or worse than others. Unfortunately, most substrates deal with aggregates or complex arrays that are difficult to model [128]. Also, lithographic methods are unable to consistently fabricate particles with the resolution needed to produce the morphological spacing and fine structure theory suggests would exhibit high enhancement. As such, our group has recently focused on a single pillar structure [129]. This simple substrate allows for ease of fabrication and eliminates complications with interparticle interactions, such as near and long range effects, facilitating relatively straightforward calculations. Using EBL, reactive ion etching (RIE), and vapor deposition, we created disc on pillar (DOP) hybrid nanostructures with a DOP plasmonic nanoparticle, a silicon pillar waveguide, and a nanoannulus and mirrored surface at the base of the pillar. While the element in this hybrid structure that has the most significant effect on the overall enhancement of the system is the DOP plasmonic nanoparticle, the combination of the other features, including optical (waveguide pillar and mirror) and plasmonic (nanoannulus) properties, contributes to the large enhancement seen experimentally herein. Other work has suggested that smaller satellite features on the plasmonic nanoparticle disc contribute greatly to the enhancement of a given system [130]. With initial parameters that were previously determined by our group, including disc diameter and pillar height, we were able to produce DOP that showed $\geq 1\text{x}10^9$ EFs. Moreover, modeling showed that these parameters should theoretically produce a system with high EFs.

The work reported herein focuses on optimizing the DOP substrate to give the greatest enhancement and exploring the analytical utilities of these reusable DOP systems. Factors including pillar height, disc diameter, and silver thickness were systematically studied using a raster analysis technique and benzenethiol (BT) as a test analyte to determine the best possible system. The affect of the DOP in a small ordered array was also examined both experimentally and numerically. Once the DOP was optimized, the analytical capabilities of the pillar system were studied. This system showed the ability to work with a variety of analytes and establish low limits of detection. Preliminary experiments examining the potential for the DOP systems to be used in conjunction with micro- and nano-fluidics were also conducted.

4.2 Experimental Section

4.2.1 Fabrication of SERS-active substrates

The fabrication process of the pillar structures has been detailed elsewhere [127] and is only briefly summarized herein. Initially, a film of Zep 520A was spin coated onto the surface of a 2” silicon wafer (Wafer World, Florida). The wafer was then softbaked and placed under vacuum in the Jeol JBX-9300 FS/E EBL system (100 keV thermal field emission gun). Individual patterns were exposed to a 420 μC/cm^2 dose for writing, yielding unique circles with diameters ranging from 100-300 nm. Each circle had 20 μm of space between other circles with a total of 25 (5-by-5) in a single pattern. Following beam exposure, the wafer was developed and then introduced to an O_2 plasma (Technics RIE). The liftoff process is completed by deposition of 10 nm of Cr with an

Electron-beam dual gun evaporation chamber (Thermonics Laboratory, VE- 240) onto the surface followed by an acetone bath and rinse. The patterns were etched to known heights using an Oxford RIE prior to Cr removal. Finally, 20 nm of SiO_2 were deposited onto the entire surface of the wafer using an Oxford Plasma Enhanced Chemical Vapor Deposition System. A representation of the fabrication process can be seen in Figure 4.1a. Figure 4.1b shows a graphical representation of a single pillar produced by the above process with Figure 4.1c being a scanning electron microscope (SEM) image of an actual pillar.

4.2.2 SERS-Active Substrate Preparation

The above fabricated substrates were made SERS-active by deposition of Ag using the Electron-beam dual gun evaporation chamber. Samples were mounted 50 cm above and normal to the source. Average deposition rates and mass thicknesses were monitored for each film using a quartz-crystal microbalance (QCM) mounted adjacent to the substrates. The Ag was deposited using a rate of 1 Å/s with varying thicknesses ranging from 20-40 nm

4.2.3 Raman Spectroscopy

All SERS spectra were collected using a JY-Horiba LabRam Spectrograph. A neutral density filter was adjusted to deliver 0.67-2.7 mW to the 633 nm laser line of a thermoelectrically cooled HeNe laser. The spectra were collected with a 50X (0.45 NA, ∞) microscope objective, having a corresponding spot size of approximately 5 µm, and 180º scattering geometry and similar wafer orientation for all pillar substrates. Sample acquisition times varied based on the study, but initial trials were set to 3 seconds. Also,

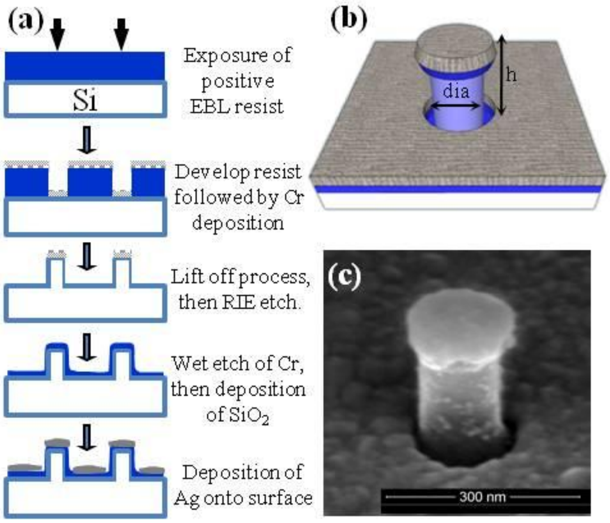

Figure 4.1: (a) Visual representation of the EBL liftoff/RIE process. (b) 3-D depiction of the pillar structure where layers are the silicon wafer (white), 20 nm SiO2 (blue), and Ag (gray). (b) SEM image of pillar structure processed as described previously with 25 nm Ag deposited onto the surface.

SERS spectra are manually corrected for background scatter using the LabSpec 4.12 software available on our Raman instrument.

4.2.4 Analyte Preparation and Data Acquisition

The analyte used in most studies was $1x10^{-5}$ M BT (99%, Fisher) in 18 MΩ Deionized water (Barnstead, E-Pure) which has been shown to form a well defined self assembled monolayer (SAM) on the metal surface. Other analytes include $1x10^{-10}$ M of the drug mitoxantrone dihydrochloride (MIT), rhodamine 6G (R6G), and thiolated DNA (Integrated DNA Technologies, Thiolated 5'-AGACATACA). Specific details about data collection have been described previously [47, 101]. However, the most common process involved placing the wafer containing the individual patterns in the bottom of a plastic Petri dish filled with approximately 2 mL of BT solution for 15 minutes before being rinsed with copious amounts of deionized water and dried. The SERS signal was optimized by focusing the microscope objective while data was often collected by rastering the laser beam across each individual pillar at 0.5 µm intervals with a single acquisition per step. Other studies involved the use of a gravity controlled flow cell where the patterns are held in place on a post within the cell. The liquid analyte then flowed through the tubing into the system, covering the sample at an approximate flow rate of 0.2 mL/min.

Scanning electron microscope (SEM) images were collected with an FEI Dual Beam SEM/FIB microscope with a field-emission gun operating at approximately 5.00 kV, depending on the angle of imaging. Sample damage and charge build-up were reduced under these conditions yielding fairly high-resolution images of the Ag-coated pillar substrates.

4.3 Results and Discussion

4.3.1 Initial Optimization of DOP

A significant quantity of densely packed aggregates are required to in order to produce a sufficient number of hot spots to generate adequate average enhancements for the substrate [51, 55, 94], our recent work demonstrated that one could achieve a high EF with a substrate having a relatively low feature density [127]. That work revolved around random aggregates fabricated from EBL followed by reactive-ion-etching. To accurately explain why the large EF occurred, it was necessary to be able to model the system. However, the random nature of the patterns complicates the modeling. Our focus reported herein shifts to simple structures that are easy to create and reproduce. The simplest structure to create and model, using our EBL technique, is a single circle that had been etched to form a pillar of a given height.

With the goal of “tuning” the DOP system to the highest EF using our experimental conditions, the parameters for the first test were set at those similar to previous work [97, 98, 126]. Each pillar was set at a pillar diameter of 150 nm and a silver disc thickness of 25 nm. A pillar with these parameters is shown in Figure 4.1c. Using a laser power of 0.67 mW and a 0.5 µm step, each pillar was examined using a raster technique, discussed previously[127], to determine the SERS activity. $1\text{x}10^{5}$ M BT was used to evaluate substrates due to its simple spectrum, its ability to form a SAM, and its singular contribution to electromagnetic enhancement [103]. To determine the optimum height for the DOP, several heights ranging from 75-375 nm were used.

Once several pillars from each height had been examined by the raster technique, the EF was calculated for each individual pillar at a given height. While EF determinations are not without flaws, it remains one of the standard ways to determine and compare SERS substrates [108]. As such, a common procedure [109] which employs Eqn. 4.1 was used:

$$\boldsymbol{EF(1575\ cm^{-1}) = \left(\frac{N_{vol} I_{surf}}{N_{surf} I_{vol}}\right)} \tag{4.1}$$

wherein I_{vol} and I_{surf} were the signal areas under the 1575 cm^{-1} bands for neat BT (Raman standard) and a SAM of BT on the substrate (SERS), respectively.

A conventional Raman measurement (under band 1575 cm^{-1}) was made of neat BT with a density of 1.073 g/mL and a focused volume of 29.5 nL. The band area of 4323 a.u. was the I_{vol} for N_{vol}. The known packing density of the benzenethiol SAM (6.8x10^{14} molecules/cm^{2}) [110, 111] and the surface area of the DOP was used to calculate N_{surf} to couple with the I_{surf} values. The surface area was determined using actual dimensions (diameter, height, etc.) from microscopy images of the given DOP structures with the Ag disc top and sidewall area counting as the majority of the surface area. This area was then arbitrarily doubled to account for the nanoannulus and added area due to roughness on the surface of the DOP. Also, during the raster process, there was no discernable Raman signal in the absence of the DOP, so it can be assumed that the EF is singularly due to the DOP.

The average EF values of the various heights were compared in Table 4.1. As shown, the height of the pillar has a large influence in enhancement as the difference between the best and worst performing DOP substrates is approximately 50-fold. The

Table 4.1: The average area (n=3) for the 1060 cm^{-1} band of individual 150 nm diameter pillars is shown along with the RSD and average enhancement factor for each given pillar dimensions (height based on actual microscopic measurements).

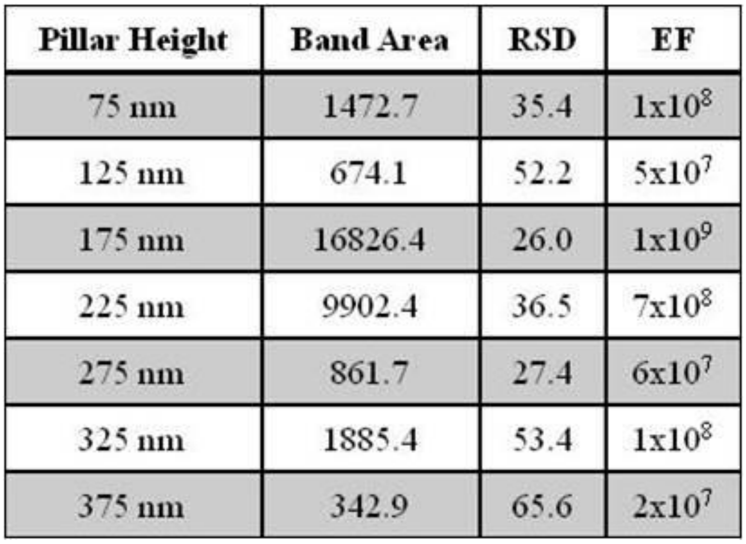

Pillar Height	Band Area	RSD	EF
75 nm	1472.7	35.4	1x10^{8}
125 nm	674.1	52.2	5x10^{7}
175 nm	16826.4	26.0	1x10^{9}
225 nm	9902.4	36.5	7x10^{8}
275 nm	861.7	27.4	6x10^{7}
325 nm	1885.4	53.4	1x10^{8}
375 nm	342.9	65.6	2x10^{7}

average EF value was found to be $1x10^9$ for the optimum height. Also, the inter-DOP RSD at the optimum height was fairly low at approximately 25%. This disparity in enhancement factors is also mirrored well with the modeled data [129]. Our simulations have demonstrated that the characteristics of the local field are strongly dependent upon the system attributes, with the pillar height and disc diameter being particularly important parameters. The magnitude of the local field around the disc was found to oscillate as the pillar height was varied in qualitative agreement with the experimental EFs reported in Table 4.1. The calculations predicted that a similar sized disc would generate the largest enhancement factor when the pillar was slightly taller than determined here experimentally; however, the general trends are consistent. The shift can be quite reasonably attributed to slight differences between the model of the nanopillar structure and the true experimental geometry.

4.3.2 DOP substrate optimization

After optimizing pillar height, the next step was to test other parameters to continue tuning the pillars to best match the Raman system. Preliminary modeling suggested that the initial feature to alter was the diameter of the nanodisc. Several different pillar diameters were tested ranging from 100-300 nm (See Figure 4.2a) with the pillar height being the optimal 175 nm. The various DOP diameters were each evaluated in the same raster method as previously used. As shown, the 100 nm diameter DOP performed ~2 times better than the previous diameter of 150 nm. This is consistent with our modeling studies, which showed that the combination of a smaller disc and decreased pillar diameter generated a larger local field by impeding the flow of electromagnetic energy away from the plasmonic nanoparticle [129]. While the 100 nm diameter DOP is

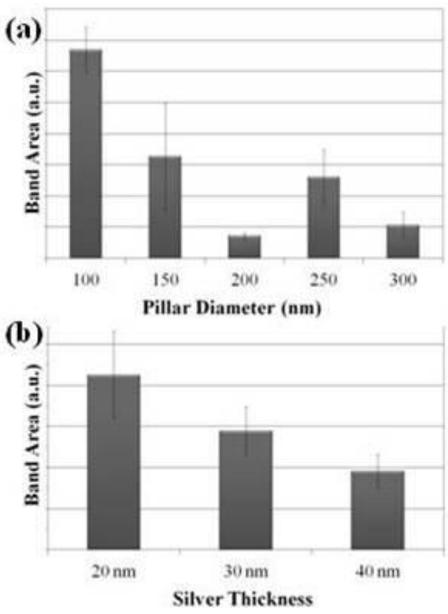

Figure 4.2: Based on the optimum pillar height of 175 nm, (a) various pillar diameters are examined, and (b) three different silver deposition thicknesses are compared for the 100 nm diameter pillars.

only slightly more SERS active based on raw signal, the smaller size leads to a significant increase in overall enhancement. A value of 4×10^9 was found for DOP substrates with both optimal height and diameter using the same procedure to calculate EF as before. Also, these 100 nm diameter DOPs had better reproducibility (18% RSD) than was seen with the previous trials focusing on optimal height with 150 nm diameter DOPs (25% RSD, see above).

Another parameter tested was the thickness of silver deposited onto the surface of the substrates (See Figure 4.2b). Previous work in the group suggested that a thinner film gave a stronger signal response for our experimental conditions [98]. As seen in Figure 4.2b, the results from this study followed previous reports. However, as one of the elements focused on is reproducibility, the slightly thicker films had fewer alterations, presumably because a smoother film is created. While taking this situation into account, it was decided that future experiments would remain with 25 nm of silver as it provided strong signal and reasonable reproducibility.

4.3.3 DOP Arrays

All above work focused on single DOP substrates with 20 µm of free space surrounding every pillar to avoid any near or long-range effects. While this system provides fairly strong raw signal and extremely high enhancement, the ability to produce an array of similar DOPs has merit as well. The first is an overall increase in signal strength coming from the multiple pillars. There could also be potential for improved reproducibility from array to array compared to single pillars as any pillar abnormality would be averaged out over the entirety of the array.

Each array pattern was laid out similarly to the single pillar system with 20 µm of space between each array and another. Every array had a known number of features and was formed into a square of N-by-N pillars (i.e.: 2-by-2, 3-by-3, etc.). In each individual array, the given number of pillars was placed into the square with 220 nm between each feature to eliminate any DOP spacing variations among the arrays. As seen in Figure 4.3a, there was a consistent increase in signal as more pillars were added to the DOP array. However, the increase is not in direct proportion to the number of pillars (the raw signal for the 25 pillar 5-by-5 array is 18-times that of the single DOP). In addition there appears to be a feature at the middle sized array that stands out more clearly when the normalized data is considered, as seen in the Figure 4.3b. The arrays also show the ability to improve reproducibility. The 2-by-2 array in Figure 4.3a has a RSD of 23% and it continues to improve to 9% for the 5-by-5 array.

To understand the experimental measurements, our collaborator has performed numerical simulations for the series of pillar arrays. CST Microwave Studio, which implements a Finite Integration Technique [131] to solve Maxwell's equations on a numeric grid, was used to model the N-by-N pillar nanosurfaces. The calculations have been performed in time domain with a mesh of 2 nm. Perfectly Matching Layer (PML) boundary conditions have been applied at the grid edges to appropriately truncate the simulation volume. The geometry used in the simulations incorporated all of the same features as the experimental samples discussed above and shown in Figure 4.1c. The pillar is modeled as a Si rod with refractive index $n_{Si} = 3.875+ i0.018$ and diameter 150 nm. It is positioned on a macroscopic Si slab, which is assumed infinite in the simulations. A 20 nm thick SiO_2 layer ($n = 1.45$) covers the Si slab and top of the pillar.

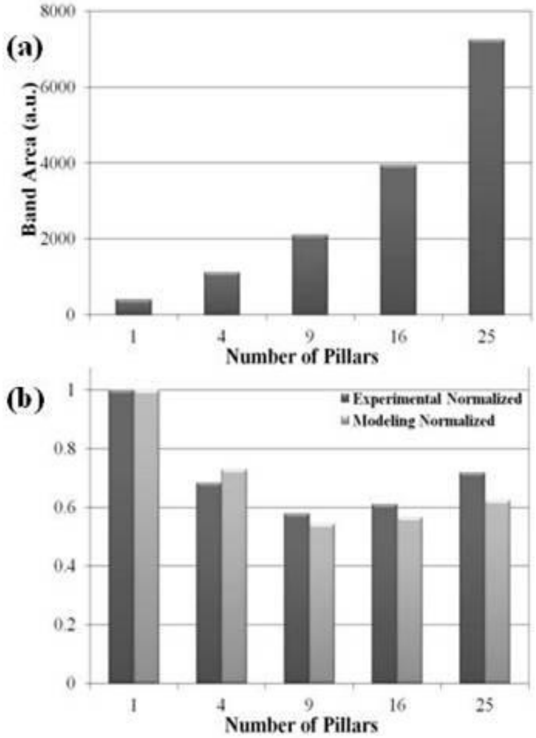

Figure 4.3: (a) Average band area for the 1060 cm^{-1} band of BT for varying numbers of pillar ranging from a single pillar system to a 5-by-5 array of pillars. All arrays have a gap of 220 nm between each pillar in a row and column and have a height of 250 nm while also having 20 µm of space surrounding to avoid long range effects. (b) The average experimental areas normalized to account for the number of pillars present (i.e., band area (25 / #pillars) and the numerically simulated normalized volume integrated electric field (see figure of merit described in text).

Above the SiO_2, there is a 25nm thick Ag layer, and its dispersion has been incorporated via experimentally determined values of the optical constants [132]. The diameter of the disc is taken to be 180 nm. No SiO_2 or Ag resides directly under the overhang of the disc to approximate the shadow effect in the fabrication. In the array configuration, the unit cell has a gap dimension of 220 nm as in the experiment.

In order to quantify the local field around the plasmonic discs, we report the volume-integrated field normalized by the total volume, which is the absolute value of the electric field integrated over a defined volume normalized by the total volume. The total volume is taken as a rectangular prism with boundaries 10 nm from the top and bottom disc surfaces and 20 nm from the outermost disc edges. This volume includes all space between pillar elements and includes ~100% of the field enhanced by the Ag discs. Figure 4.3b shows how the integrated field varies as the number of pillars in the array increases. A single pillar generates the largest integrated field per unit volume; there is also minimum predicted for the 3-by-3 array in agreement with the normalized SERS signal measured experimentally (Figure 3b). The distribution of the field provides some insight as to why the minimum exists. Figure 4.4 shows contour plots of the electric field in a plane containing the top surface of the pillars for all of the arrays. The incident field is propagating down on the structure and polarized in the y direction.

It is clear from the field distribution that certain spatial regions are favored and localize more of the energy. Note that if the arrays were infinite, then the field distribution would be identical in each unit cell containing a pillar and repeat over the whole area. However for the arrays, asymmetries arise from the truncation of the periodic grating created by the pillars, which is the origin of the nonlinear behavior of the

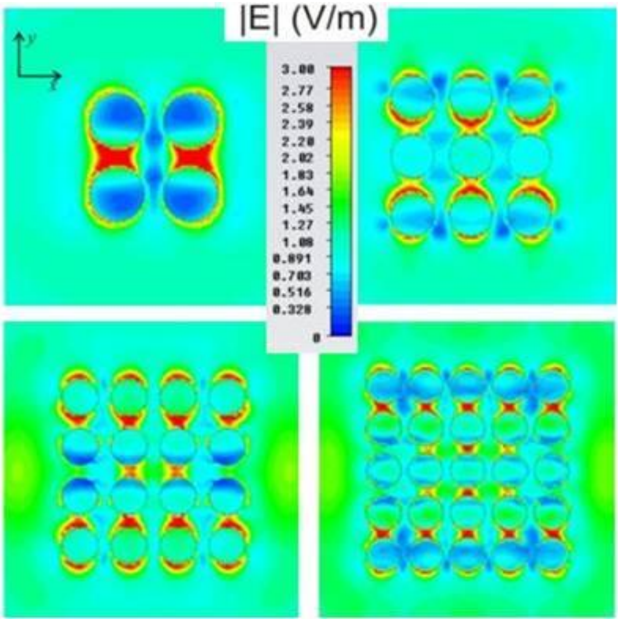

Figure 4.4: Color maps of the electric field modulus in a plane on top of the discs for several clusters. The incident field is propagating down into the page, and the incident polarization is along y.

integrated field with respect to the number of pillars in the array. The diffracted field from the array truncation sums up coherently with the local electric field to create a quasi-stationary optical wave over the entire array area. Along the polarization direction of the incident field (y), there is strong coupling between discs, while along x, the inter-pillar coupling is weak. In all arrays, the exterior pillar rows parallel to x localize significant field density, while the interior pillar rows parallel to y tend to localize density. The latter effect becomes more pronounced as the arrays get larger. The 2-by-2 and 3-by-3 arrays lack strong coupling in the center along y. In addition, the total volume more than doubles going from four to nine pillars and as a result, the 3-by-3 array produces the smallest volume integrated field. In general, the field distribution is affected by the diffraction effects in a complex manner that does not have a linear dependence on the number of pillars. Our collaborator has expanded this topic recently with an in depth study that has been published in the *Journal of Physical Chemistry C* [133].

4.3.4 Analytical Impacts of DOP Systems

SERS has potential for sensitive and selective analysis with many applications. However, many substrates have practical drawbacks that limit analytical utility. Random substrates, such as colloids, often offer strong signal and enhancement, but have poor uniformity, hence reproducibility. Engineered substrates, on the other hand, generally have controlled, reproducible features, but they often yield signal intensities adequate enough to be of significant use for moderately polarizable analytes. The DOP system is unique in that is has a strong overall signal, an EF of 10^9 or higher, and high reproducibility from pillar to pillar. Furthermore, since the DOP features are etched into the Si wafer, they are a relatively robust structure. Many types of SERS substrates can only withstand irradiation once for a fraction of a second before it begins to diminish [113]. The DOP pillars can withstand multiple irradiations without losing signal. When looking at an optimized (100 nm diameter and 175 nm height) single DOP repeatedly for more than 10 one second acquisitions, the pillar gave consistently strong signal with an RSD of better than 7%.

This DOP system also offers certain practical advantages over other systems. One benefit is the ability to reuse the system months after it has initially been fabricated and used. Using aqua regia, array chips were cleaned for approximately 5 minutes. This removed the old oxidized silver, allowing the deposition of a new 25 nm film onto the chip. Figure 4.5a compares a 5-by-5 pillar array looked at initially (left) with the array once cleaned and deposited on a second time for analysis (right). The inset shows that after approximately 5 minutes of cleaning that almost all of the silver was removed from the array. These extra features could contribute to the signal intensity being almost four-times greater than initially found. More significantly, the deposition of Ag and Raman spectrometer alignment are different for this reusability comparison performed over a period of months. These chips could also be reused with other analytes than BT. Using a chip that had been previously analyzed with BT, it was cleaned and re-deposited on as mentioned above, and 1x10^{-3} M thiolated single strand DNA was attached to the surface and a single DOP was analyzed. The DNA gave a signal similar to that of other work [134], particularly the bands around 1200, 1300, and 1500 cm^{-1}, and appear without any contamination from previous use (see Figure 4.5b). The DOP system also has high sensitivity. In Figure 4.6a, R6G was used at several concentrations in the flow cell setup

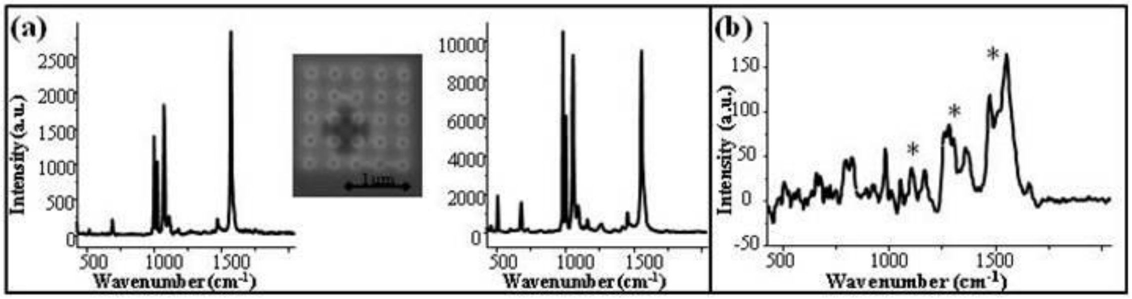

Figure 4.5: Reusability: (a) The initial response of a 5-by-5 array to BT (left) and several months later (right) after aqua regia cleaning and re-deposition of Ag. The insert is an SEM of the cleaned array. (b) A single DOP after cleaning and re-deposition showing signal response to a single stranded thiol -5'-terminated oligonucleotide (see text). Certain bands (denoted by *) correlate to those seen from single stranded DNA in other published work [134].

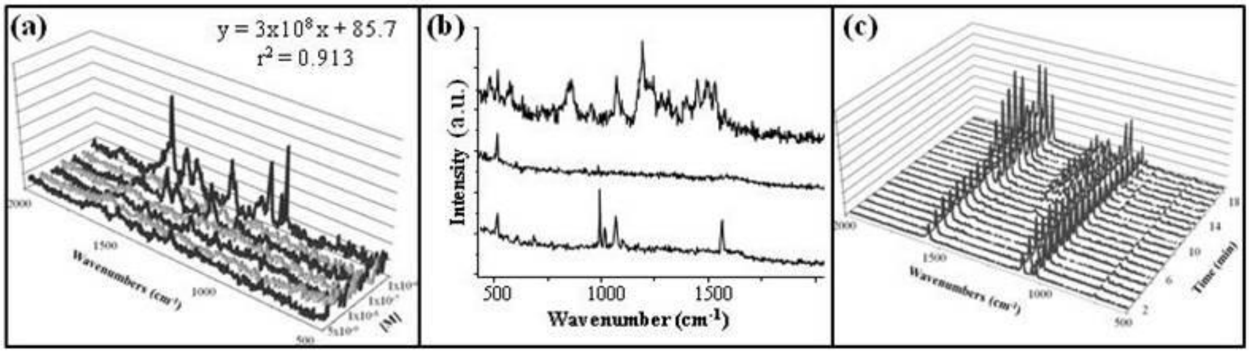

Figure 4.6: (a) Spectra for R6G at given concentrations, on a single DOP, where the analyte is rinsed off in between trials using methanol followed by water. Calibration plot data is shown. (b) Microfluidic dynamic study showing multiple analyte reversibility of a single DOP with 10-10 M MIT (top), rinsing with water (middle), followed by exposure to 10-5 M BT (bottom). (c) A time lapsed view of a single DOP with BT binding to the surface. A spectrum was taken every minute with the thiol flowing through a cell. The appearance of additional spectral features at about 10 minutes is attributed to either an impurity or photodegradation.

mentioned earlier. Beginning with 5x10^{-9} M solution of R6G, a single pillar was examined and found to give a discernable signal. The pillar was then rinsed with methanol followed by water and then found to no longer show signal. 1x10^{-8} M R6G was then added to the system and the pillar was analyzed again and found to have a slightly higher signal than previously observed. This process continued for other concentrations as well, showing the DOP system in not only sensitive enough for low concentrations but that the DOP is reversible and can generate calibration plots with subsequent analysis of unknowns.

While reversibility with a single analyte is important, the DOP structures can show reversibility with various analytes as well. Figure 4.6b shows a single pillar exposed to 1x10^{-10} M MIT (note: MIT is resonance enhanced). After irradiation to verify the activity of the pillar, the flow cell system was flushed with water for a couple of minutes. A spectrum was then obtained of the same pillar which showed that the MIT had been removed. 1x10^{-5} M BT was then added to the flow cell and another set of spectra were obtained showing that the BT had bound to the pillar and produced a strong signal.

Moreover, this substrate also has the ability to analyze chemical reactions in real-time. Figure 4.6c shows an experiment where 1x10^{-5} M BT was passed through a flow cell containing a single DOP. As seen, the BT began to bind and show signal around the 2 minute mark and continued to strengthen for the next few minutes. Around the 10 minute point, some unusual bands began to appear in the 1100 - 1200 cm^{-1} spectral region. The additional bands may be due to photo degradation [101], although the other known BT bands do not appear to be appreciably altered. It is also possible that the additional bands occur as impurities begin to interact with the developing SAM of BT. These experiments demonstrate the DOP would be useful to monitor unique surface chemical reactions and interactions in a micro- or nano-fluidic system.

4.4 Conclusions:

In summary, we demonstrate that DOP hybrid nanostructures, singularly or in N-by-N arrays, can be tuned to provide exceptional SERS enhancements that correlate with numerical simulations. These pillars also represent SERS substrates that have good reproducibility (better than 7% for a single pillar) without sacrificing enhancement. Once optimized to the 632 nm laser, a single DOP nanostructure was able to obtain an EF of $4x10^9$ for BT. Also, raw signal can be increased to lower the detection limit for analytes by fabricating compact DOP arrays.

Aside from good reproducibility and sensitivity, DOP systems offer other analytical benefits. Silicon DOPs are robust structures that have the ability to be cleaned and reused with various analytes. The pillars also boast reversibility, allowing for potential use in other applications such as nano-fluidics. The DOPs have already shown progress in tracking chemical reactions in real-time flow cell environments; future work will focus on continuing to use these structures in flow experiments to determine the full extent of these capabilities.

4.5 Acknowledgements

Nanofabricated substrates were created at Oak Ridge National Laboratory's Center for Nanophase Material Sciences (CNMS), sponsored by the Scientific User Facilities Division, Office of Basic Energy Sciences, U.S. Department of Energy. Additional support provided by the University of Tennessee-Oak Ridge National Laboratory, Joint Directors Research and Development Program. K.L.S. thanks Drexel University for start-up funding.

Chapter 5

Silicon nanopillars for field enhanced surface spectroscopy

Chapter 5 is adapted from a research article that has been recently submitted to *ACS Nano*. This article focuses on developing nanopillar structures that behave similarly to the DOP structures presented earlier. The main difference is the lack of a metal surface on these new nanopillars. Nickolay Lavrick is the principal coauthor with this work and added the theoretical modeling discussed throughout the article. The only major revisions that have been made from the submitted form include moving the Experimental section prior to the Results and Discussion.

5.1 Introduction

Semiconductor nanowire and nanopillar structures have been a subject of significantly increased attention in recent years, largely due to the renewed interest in their unique properties that can be utilized in photon detection and solar energy applications [135-142]. Although semiconductor nanostructures with characteristic sizes of the order of 100 nm are generally too large for quantum confinement effects to take place [143-145], optical properties of such nanostructures tend to deviate substantially from those of bulk semiconductors [137, 139, 146-150]. Such optical phenomena beyond the quantum confinement regime can be explained by the fact that optical resonators with sizes (diameters) approximately an order of magnitude smaller than the wavelength of light in vacuum can be implemented in semiconductors. Indeed, several semiconductor materials, in particular silicon, possess very high refractive indices (>3.5) combined with low extinction coefficients in a portion of the visible spectrum and in the near infrared. These properties make them uniquely suitable for creating low loss optical resonators with characteristic sizes of approximately 100 nm.

The complex and nontrivial nature of optical resonances in semiconductor nanowires and nanopillars clearly follows from a number of very recent studies in this area [137, 139, 147-150]. In particular, a series of recent studies by Brongersma's group [137, 139, 148] demonstrated that leaky mode resonances in semiconductor nanowires provide a powerful and elegant means to engineer light absorption in optoelectronic devices [139, 151] and tune the color of silicon nanostructures [148]. Muskens *et al.* [152] showed that strong Mie-type internal resonances in vertically aligned semiconductor nanowire arrays lead to record levels of light scattering that can be tuned over a wide spectral range. Furthermore, the guided mode properties of individual silicon nanopillars can give rise to a palette of surprisingly vivid colors readily visible in bright field microscopy [150]. Although this recent study has unambiguously demonstrated that individual silicon nanopillars exhibit a certain type of resonance due to the fundamental HE_{11} guided mode, a remaining open question is whether significant enhancements of local field can be associated with this phenomenon and utilized in analytical optical techniques in analogy to localized surface plasmon resonance. To our best knowledge, the possibility of strong field enhancement associated with the fundamental guided mode in vertical silicon nanopillars has not been evaluated. Here, we point to conditions when enhancement of local field in the vicinity of an individual silicon nanopillar is maximized and demonstrate experimentally that such conditions associated with HE_{11} mode provide a new pathway to spectroscopic analytical techniques, including surface enhanced fluorescence (SEF) and Raman scattering (SERS), which do not involve plasmons.

Although studies of semiconductor nanowires and nanopillars often take advantage of “bottom-up” technological strategies, such as vapor-liquid-solid (VLS) growth [153-155], a deterministic technological strategy based on lithographic patterning is better suited for creating sparsely spaced silicon nanopillars with more flexible control over their shapes and dimensions. Consistent with our goals and our previous positive experience with nano and micro fabrication [81, 156, 157], we relied on electron beam lithography (EBL) and anisotropic reactive ion etching (RIE) to create silicon nanopillars analogous to the ones studied by Seo *et al.* [150], however, with various shapes (Figure 5.1). Our rationale behind exploring nanopillars with distinct sidewall profiles was three-fold: (i) tapered shapes are known to improve coupling of HE_{11} mode in cylindrical dielectric antennas [158], (ii) nanopillars with variable cross-sections exhibit resonances in a wider or multiple spectral regions, and (iii) while anisotropic RIE of silicon offer good control over sidewall profile, it rarely yields perfectly vertical sidewalls. Previous work in our group focused on using EBL and RIE to create silicon nanopillar structures, metalized for plasmonic effects, to perform SERS with high sensitivity [156]. Relatively short pillars were found to maximize plasmonic and optical cavity contributions to the observed overall fields [157] and exhibited enhancement factors (EFs) of $>10^9$ with high reproducibility. Here, we utilize similar technological approaches and demonstrate the

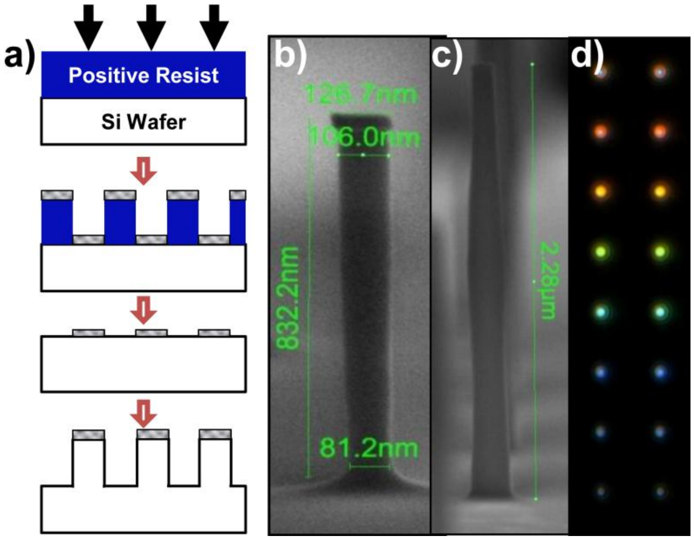

Figure 5.1: **(**a) Fabrication sequence used for creating silicon nanopillars; (b) SEM image of a nanopillar type #3 with slightly undercut sidewalls; (c) SEM image of the tallest tapered nanopillar used in this study (Table 5.1, type #7); (d) dark field optical microscopy of nanopillars type #3 with average diameters ranging from 95-180 nm.

potential of relatively long, narrow silicon nanopillars for achieving substantial non-plasmonic field enhancements.

5.2 Experimental

5.2.1 Silicon Nanopillar fabrication

We used a fabrication sequence that relied on EBL, metal mask lift-off patterning, and anisotropic RIE of silicon as described previously and can be seen in Figure 5.1a [127]. Detailed steps of this sequence are as follows. A 300 nm film of ZEP 520A, a high resolution positive tone resist suspended in anisole, was applied to the wafer using spin coating at 6000 rpm for 45 seconds onto a 4" silicon <100> wafer. Once coated, the wafer was then baked at 180˚C for 2 minutes and placed under vacuum in the Jeol JBX-9300 FS/E EBL system (100 keV thermal field emission gun).

Individual features were exposed to a 420 $\mu C/cm^2$ dose for writing, yielding circles and ellipses with targeted diameters ranging from 50-150 nm. Each circle or ellipse had 5 µm of space between other features and was laid out in ascending diameter from left to right while duplicating each row for a total of six of each diameter (See Figure 5.1c for small sample). Following beam exposure, the wafer was developed in xylene and then introduced to an O_2 plasma (Oxford Reactive Ion Etcher).

In order to create a masking layer for the RIE of silicon, a 20 nm chromium layer was deposited onto the surface of the wafer using an Electron-beam dual gun evaporation chamber (Thermonics Laboratory, VE- 240). The excess resist and chromium were then removed *via* liftoff using an acetone bath followed by isopropyl alcohol and deionized water rinses. Anisotropic RIE of silicon was then performed using a combination of inductively coupled plasma (ICP) and capacitively coupled plasma (CCP) conditions. ICP power, CCP power, pressure, substrate temperature, and a chemical composition of the plasma were adjusted to achieve the targeted nanopillar with close to vertical sidewalls. Plasma composition was varied by changing flow rates of the three processing gases: argon, sulfur hexafluoride, and octafluorocyclobutane. Different nanopillar heights were obtained by varying etch times. To determine exact dimensions of each pillar with a given etch recipe, scanning electron microscope (SEM) images.

5.2.2 FDTD analysis

Finite Difference Time Domain (FDTD) Solutions software package (Lumerical Inc.) was used in our simulations of the fabricated structures in order investigate their optical behaviors, in particular their ability to enhance the local field. In order to take into account effects of various components of our experimental system, we compiled a series of 3-D FDTD models that were comprised of an individual silicon nanopillar, a silicon substrate and a Gaussian light source impinging on the pillar coaxially (Figure 5.2a) Perfectly matching layer (PML) boundary conditions with 36 layers were used on all sides. The sizes of the simulated volume were 10 μm x 10 μm x 4.5 μm (X x Y x Z), large enough to accommodate a converging Gaussian source without truncating the beam. The Gaussian beam source was set to have propagation direction opposite to the Z axis (*i.e.* top to bottom) and linear polarization parallel to X-axis. The source parameters were selected to span wavelength region of 475 to 675 nm. Throughout the simulated volume outside the nanopillar region we used a variable mesh size with a maximum size of

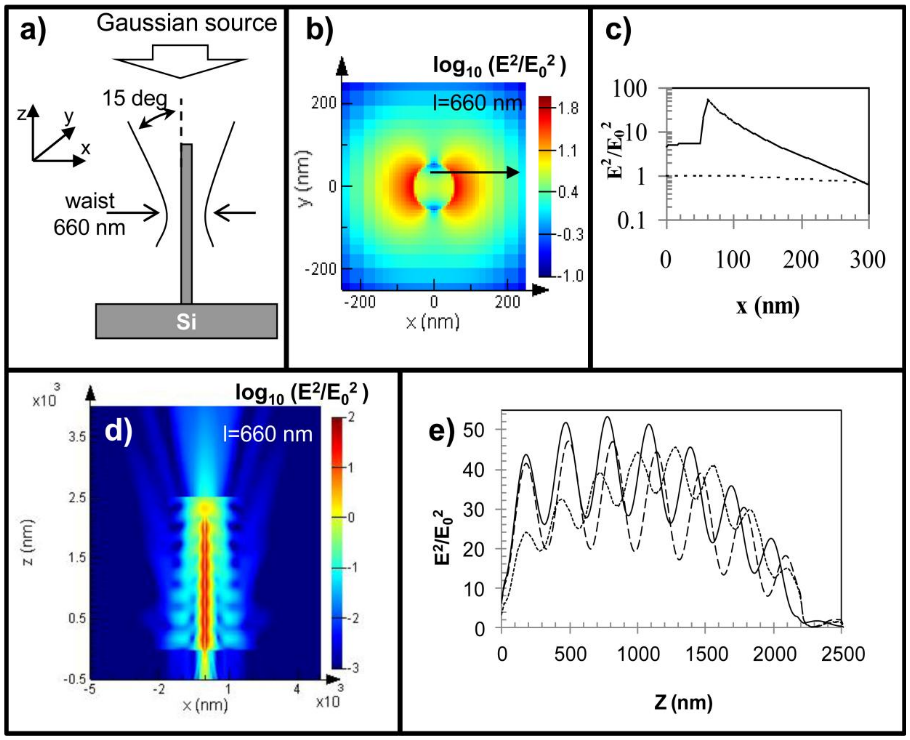

Figure 5.2: FDTD simulations of a vertical Si nanopillar on a silicon substrate coaxially illuminated by a Gaussian beam: (a) schematic representation of the X-Z intersection of the 3D FDTD model used in this study; (b) normalized field intensity in the X-Y plane at z=800 nm; (c) normalized field intensity along the x-axis at x=800 nm in the region shown by the arrow in Panel b in vicinity of the pillar (solid curve) and without pillar (dotted curve); (d) normalized field intensity in the X-Z plane intersecting the pillar axis; (e) normalized field intensity along the z-axis in vicinity of the pillar at x=60 nm y=0 nm calculated for 645 nm (dotted curve), 660 nm (solid curve) and 675 nm (dashed curve). All simulation data shown here are obtained for pillar height and diameter of, respectively, 2,200 nm and 110 nm. Local field distributions in panels (b-d) are calculated for a wavelength of 660 nm and displayed on a logarithmic scale.

50 nm x 50 nm x 20 nm (X x Y x Z). A refined mesh with a constant step of 5 nm x 5 nm x 2 nm (X x Y x Z) was used in the region that included the pillar plus at least 20 nm margins outside the nanopillar along each axis. The main variable parameters of our simulations included: (i) pillar diameter, (ii) pillar height, and (iii) Gaussian beam convergence. The results of the performed simulations were analyzed by evaluating local field intensity in the following planes: (ii) perpendicular to Y-axis at X = 0, (ii) perpendicular to X-axis at Y = 0, perpendicular to Z- axis at Z = 200 nm (for shorter pillars) and Z = 800 nm.

5.2.3 Raman Spectroscopy

All Raman spectra were collected using a JY-Horiba LabRam microscope. Details of the instrument setup have been described previously [101, 127]. A 50X (0.45 NA, ∞) microscope objective was used to deliver 0.67 mW of the 633 nm line of a thermoelectrically stabilized HeNe laser with a spot size of approximately 2.5 µm. All spectra were collected with a 180° scattering geometry. Sample acquisition times were generally set to 3 seconds. Silicon Raman signal was optimized by fine-focusing the microscope objective, and the maps of Raman spectroscopic signals were collected while rastering the laser beam across each pattern at 0.5 µm intervals (1 spectral acquisition per step) over a single pillar (See Figure 5.3). Normally SERS spectra are manually corrected for the broad background scatter using the LabSpec 4.12 software of our Raman system.

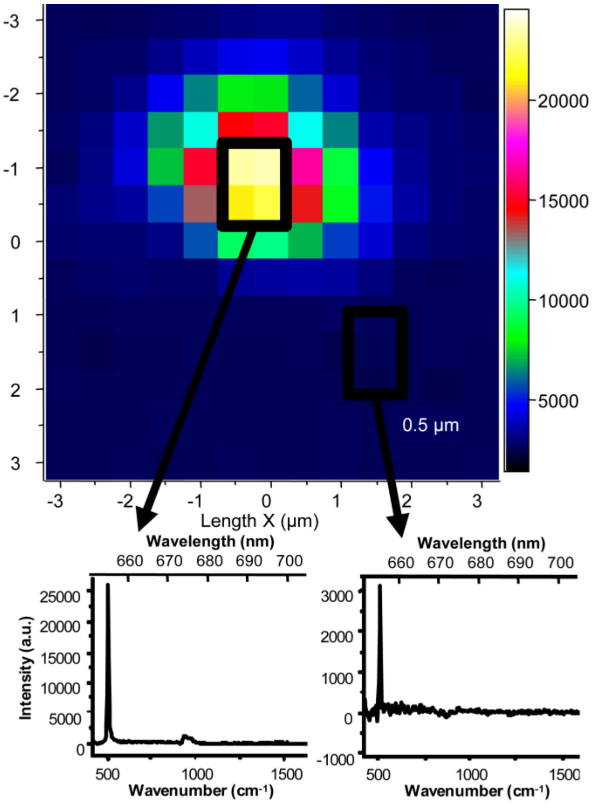

Figure 5.3: Raman map (top) shows enhanced intensity of the silicon phonon line due to presence of a silicon nanopillar of type #4 with an average diameter of 95 nm. Also shown are complete Raman spectra measured on (bottom left) and off (bottom right) the nanopillar.

Raman enhancement factors (*EFs*) were computed using Equation 5.1:

$$\boldsymbol{EF = \frac{RSI}{\Delta An}} \tag{5.1}$$

where *RSI* is the raw signal increase (*i.e.* the ratio of the areas of the silicon 500 cm^{-1} band, Raman zinc pthalocyanine (ZnPc) 1500 cm^{-1} band, or the fluorescence NHS-rhodamine signal) on-versus-off the single nanopillar under investigation. The *RSI* values in more detail throughout the various parts of the discussion section. *ΔAn* is the fractional increase in analyte amount (computed as volume or area) due to the presence of the nanopillar (approximated as a cylinder for EF estimates). The fractional increase can be calculated using the equation:

$$\boldsymbol{\Delta An = \frac{\pi Dht_1}{\pi W^2 t_2}} \tag{5.2}$$

where the diameter (*D*), height (*h*), and focused laser beam of spot size waist (*W=1,250 nm).* Also, *t* is the analyte thickness on the pillar (t_1) and Si floor (t_2). For determining volumes the depth of the analyte material was taken as the thickness of the vapor deposited ZnPc film or estimated to be 100 nm when considering the Si base material. In the case of the fluorescence of NHS-rhodamine, an ultra thin layer was assumed due to the APTES linker and, thus, areas (rather than volumes) were used. In this case a pixel of the microscope area detector (1 μm^2) and the nanopillar surface area were used. The calculated EF in each case is also reported as the average for the entire nanopillar structure; localized values can be significantly higher.

5.2.4 Microscopy

Scanning electron microscope (SEM) images were collected with an FEI Dual Beam SEM/FIB microscope with a field-emission gun operating at approximately 5.00

kV, altered slightly depending on the angle of imaging. Sample damage and charge build-up were reduced under these conditions yielding moderate-resolution images of the Si pillar substrates. All optical microscopic images were obtained using a Nikon Eclipse 100 microscope using a 100x microscope objective. The microscope was equipped with a high pressure broad band Hg light source, a multicolor fluorescence cube (DAPI-FITC-TRITC) [159], and a Digital sight CCD camera (DS-2M, Nikon, Inc) controlled by NIS-Elements software.

5.2.5 Substrate Preparation

After fabrication, some pillars were fluorescently labeled for imaging. Using a method described previously [160], each piece of silicon wafer containing nanopillars was placed in a vial with anhydrous toluene with the addition of 3-aminopropyltriethoxysilane (APTES) to create a 10% solution by volume. The chips soaked in the APTES solution for one hour at room temperature before being rinsed sequentially with toluene, methanol, and 18 MΩ deionized water (Barnstead, E-Pure). This process has been shown to yield a smooth, thin, uniform layer of APTES. From that point, one of two fluorescent dyes was used. 30 µL of a 1 mM solution of either NHS-rhodamine dye or fluorescein isothiocyanate (FITC) dye was spotted onto the pillars and allowed to bond to the chip (15 minutes for NHS-rhodamine and 45 minutes for FITC) before excess dye was removed.

Some of the fabricated nanopillars were coated with a thin layer of ZnPc. ZnPc was thermally evaporated onto the silicon chips with the pillars in a Cooke CVE 301 physical vapor deposition (PVD) system. In order to deposit comparable amounts of ZnPc on the nanopillar sidewalls and surrounding silicon substrate, the chips were mounted at 45° angle with respect to the line of sight between the substrate and the evaporation source. After depositing 12 nm of ZnPc, the substrate was rotated 180° and another 12 nm were deposited. The nominal thickness of the deposited ZnPc was monitored with a QCM mounted in the PVD. As a result of this procedure, approximately 24 nm of ZnPc was deposited on the silicon wafer surrounding the pillars while the thickness of ZnPc layer on the pillar sidewalls had a crescent distribution with estimated maximum and average values of, respectively, 12 nm and 8 nm.

5.3 Results and Discussion

To identify the boundaries of the nanopillar design space and to drive successive iterations of our fabrication sequence, we carried out numerical simulations of our experimental system using the FDTD method. Our FDTD model closely resembled our experimental system and included an individual silicon nanopillar, a silicon wafer substrate and a Gaussian light source impinging on the pillar coaxially (Figure 5.2a, further details of the FDTD model are given in Experimental section). Our evaluation of the FDTD model indicates that a wavelength-dependent enhancement of the local field intensity on the surface and in the immediate vicinity of a sufficiently long silicon nanopillar can reach more than two orders of magnitude. Our FDTD simulations conducted for nanopillars of different diameters revealed that 110 nm is the pillar diameter that corresponds to the strongest field enhancement at approximately 650 nm. This finding correlates well with the reflectivity minimum at approximately 630 nm reported previously for arrays of silicon nanopillars with 110 nm diameter [150]. We also found that maximum enhancement of the local field intensity increases significantly when pillar heights increase and also when the angular convergence of the incident beam decreases.

We conducted more detailed FDTD analysis for a pillar height of 2200 nm and beam divergence of 15 deg (Figure 5.2). These values correspond, respectively, to the longest nanopillars that we could reproducibly fabricate and to the smallest convergence angle that we could achieve in our experiments when illuminating nanopillars through a high-magnification (100x) microscope objective. The wavelength dependent changes in the distribution of the electric component of the local field intensity in the plane perpendicular to the nanopillar axis are indicative of the fundamental, HE_{11}, mode (Figure 5.2b) and consistent with the results reported previously [150]. Importantly, a strongly enhanced field concentrates in extremely small areas in the nanopillar vicinity. As can be seen in Figure 5.2c, normalized field intensity, E^2/E_0^2, decays from approximately 50 to 10 within less than 50 nm from the nanopillar surface. Evaluation of the local field intensity in the Y-Z plane intersecting the nanopillar axis and parallel to the polarization plane (Figure 5.2d and e) provides additional insights into the magnitude and mechanisms of the observed enhancement. As expected, a periodic pattern superimposed over the local intensity distribution is formed due to standing waves at the reflecting surface of the silicon substrate (Figure 5.2d and e). The maximum field intensity is observed at $Z \approx 800$ nm, *i.e.* shifted slightly along Z-axis with respect to the beam waist (centered at $Z=1000$ nm) towards the substrate. We analyzed the wavelength dependent nature of this enhancement and used it for guidance in selecting nanopillar diameters for our experiments in various spectral regions.

Consistent with the guidance obtained from our FDTD analysis, we fabricated a series of silicon structures with nanopillars of various heights and shapes and average diameters in the range of 95 to 165 nm. In order to evaluate the ability of such structures to enhance Raman scattering and fluorescence signals and to demonstrate their versatility in these potential applications, we devised and conducted three types of experiments that focused on (i) analysis of the enhanced Raman scattering in silicon, (ii) fluorescent microscopy of nanopillar structures labeled with NHS-rhodamine and FITC, and (iii) Raman spectroscopy of a thin layer of ZnPc deposited onto the nanopillar and surrounding area. Results of these experiments provide the first experimental evidence that individual silicon nanopillars can be used as versatile and highly efficient enhancers of local field intensity with utility in analytical optical techniques.

5.3.1 Nanopillar Fabrication

A fabrication sequence similar to the ones reported in our own previous studies [156] and by other groups [149, 150] was used to create silicon nanopillar structures. In brief, EBL was used initially to create discs in the Cr masking layer on top of a Si wafer before RIE was used to etch the pillars to specific parameters (see Figure 5.1a). A more detailed description of the fabrication process can be found in the Materials and Methods Section. An important feature of our structures that differentiates them from the majority of previously implemented silicon nanopillars was a large area surrounding each individual nanopillar devoid of additional features so as to allow for optical interrogation without interference from other structures. By varying the etch time, plasma composition and plasma power during the RIE etch, we performed a series of fabrication iterations. In addition to the guidance from our numerical modeling, each iteration accounted for the feedback from the structural analysis of the best performing nanopillars fabricated in the preceding iteration. As a result, several pillar "types" were created (Table 5.1). As can be seen in the table, the two main variable parameters of the fabricated pillars are height and diameter. It should be noted that diameters of the structures can be described in two ways. The first description is according to the diameter of the circular CAD feature used to pattern the Cr mask. It is important to emphasize that this diameter tends to deviate from the actual size of the fabricated nanopillar since the sidewall produced by the RIE is rarely perfectly vertical. The other way to describe pillar diameter is to calculate the average diameter of each nanopillar based on the analysis of its scanning electron microscope (SEM) images. While this parameter is more directly related to the actual pillar size, relying on structural metrology based on SEM imaging has its own disadvantages. In particular, the accuracy of SEM quantitative measurements is known to vary depending on the type of sample, accelerating voltage, *etc.* and typically is not better than 10%.

Using the same RIE recipe as was used for creating SERS active substrates in our previous studies [156], we fabricated pillar types #1 and #2 with slightly undercut sidewalls (Table 5.1). Subsequent modification of the RIE recipes allowed us to create slightly conical shapes also bottle shaped nanopillars (see Table 5.1).

5.3.2 Enhancement of Intrinsic Silicon Raman Scattering

Once a variety of silicon nanopillar structures had been fabricated, a series of optical probing experiments were conducted. In our initial screening tests, we used dark field optical microscopy, which could clearly visualize each individual nanopillar as a

Table 5.1: Ability of silicon nanopillars with various shapes and heights to enhance intrinsic Raman scattering. In each series of nanopillars of the same type, the optimum diameters correspond to a nanopillar that exhibited strongest enhancement of the silicon Raman line. Note that Si line ratio is calculated as a raw signal enhancement and reflects presence of a strong background Raman signal from the silicon substrate.

Type	**Height**	**Optimum Diameter**		**Shape**	**Si Line Ratio**
		CAD	**Average**		
#1	300 nm	120 nm	120 nm	Cylindrical	1.32
#2	700 nm	90 nm	100 nm	Slightly conical throughout length	2.47
#3	825 nm	130 nm	105 nm	Slightly undercut	1.65
#4	800 nm	120 nm	Not Available	Cylindrical with slight cone on top	4.91
#5	975 nm	80 nm	95 nm	Slightly conical, close to cylindrical	8.04
#6	1300 nm	115 nm	165 nm	Bottle shaped, slightly conical at top	6.76
#7	2300 nm	120 nm	185 nm	Elongated bottle, slight undercutting below neck	12.00

bright light-scattering spot, often characterized by a vivid color (Figure 5.1d). Defective and missing nanopillar structures could be readily identified in dark field optical microscopy observations. Subsequently, Raman spectroscopy mapping of our samples was performed using a confocal Raman microscope with a 633 nm HeNe laser excitation. In these experiments we mapped the intensity of the silicon line (phonon line of the single crystal silicon) at 500 cm^{-1} over the 5μm x 5μm areas surrounding each nanopillar. As seen in Figure 5.3, the intensity map of the silicon line has a maximum that coincides with the nanopillar position. The amplified silicon Raman signal due to the presence of the pillar can also be clearly seen in the spectra shown in Figure 5.3 below the intensity map. Ratios of the silicon band areas for on-pillar and off-pillar laser spot positions are given in Table 5.1. This ratio was used to judge the *relative* enhancement of the Raman scattering by various nanopillar types in analogy to the methodology described previously [161]. It should be emphasized, however, that our Raman spectroscopic measurements of silicon nanopillar structures on silicon substrates always included a significant background signal from the substrate.

Several notable trends can be seen in Table 5.1. The most readily recognizable trend is that taller nanopillars exhibited higher signal enhancement (*i.e.* compare type #6 with type #7). However, an explanation of this trend based on the larger surface area of taller pillars can be completely ruled out since enhancements of the silicon Raman line also depended dramatically on the pillar shape. In particular, enhancements of Raman scattering by type #3 nanopillars with undercut (negatively sloped) sidewalls were generally significantly lower compared to the other nanopillar types characterized by tapered (conical) shapes. While a more extensive FDTD analysis of nanopillar models with various shapes could provide valuable insights in understanding this difference, it is reasonable to assume that the tapered region improves coupling of the scattered light into the collecting optics in analogy to the tapered regions of dielectric rod antennas [158]. The strongest enhancement of the silicon line Raman scattering was observed in the case of tallest pillars (type #7, shown in Figure 5.1b): the raw signal ratio was found to be 12. This value was used for calculations of the enhancement factor EF (see below).

Figure 5.4 shows analysis of the raw Raman signal enhancement for nanopillars with two different shapes (Figures 5.4a-c) with average pillar diameters in the range of 95-210 nm. The values in Figure 5.4 are the averages of measurements on three separate nanopillars of the given diameter, with the RSD for each average better than 10%. It is worthy to note that in case of a perfectly cylindrical nanopillar, FDTD analysis predicts a straightforward relationship between the pillar diameter and the wavelength at which the local field undergoes maximum enhancement. In particular, our FDTD simulations predict that the nanopillar diameter needs to be approximately 110 nm for the strongest local field enhancement to be achieved at 660 nm (see Figure 5.2e). Taking into account the Stokes shift of approximately 20 nm for the Raman silicon line in our measurements (*i.e.* wavelengths of probing and scattered light are, respectively, 632 nm and 652 nm) this prediction correlates well with the trend shown in Figure 5.4b for nanopillars type #5. It appears, however, that optimum average diameters experimentally determined for other nanopillar shapes, such as type #6 with noticeably narrower top and wider bottom may deviate from this prediction. This deviation is most likely a complicating consequence of the cylindrical nanopillar shapes with variable cross-sections. On the other hand,

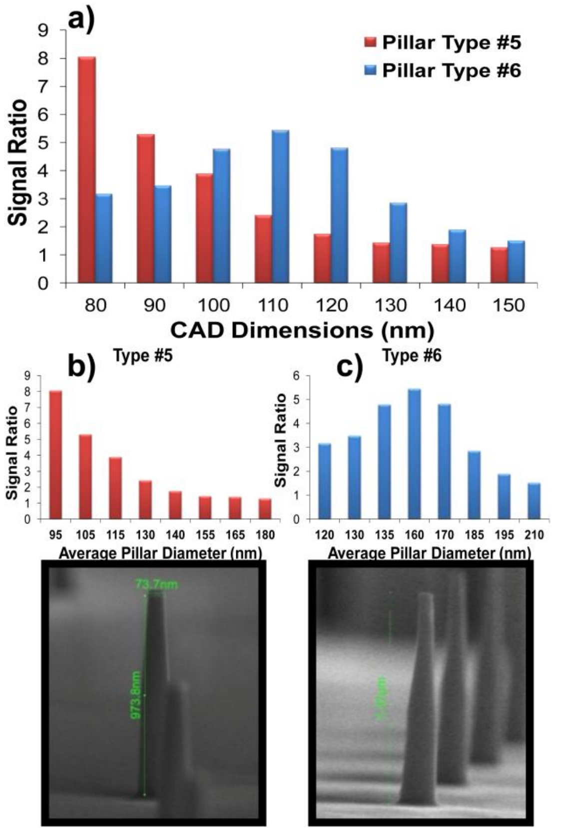

Figure 5.4: **(**a) Silicon Raman signal ratio (on-versus-off nanopillar, 500 cm^{-1}) trend of two different types and heights of nanopillars based on the CAD (Cr mask diameter at the top of the structure). (b) Trend with average pillar diameter of pillar type #5 (see Table 5.1) with correlating SEM image below. (c) Trend with average pillar diameter of pillar type #6 with correlating SEM image below.

nanopillars type #5 and type #6 fabricated using the same CAD dimensions had significantly different average diameters (Figure 5.4). An important practical implication of these observations is that a pattern with same CAD diameter can be used to fabricate nanopillars optimized for different wavelengths.

5.3.3 Enhanced Fluorescence

Strong enhancements of the Raman silicon line generated by type #5 and #7 nanopillars encouraged us to use them in subsequent fluorescent microscopy experiments and additional Raman scattering measurements. Our hypothesis was that local field enhancement in vicinity of silicon nanopillars should enable enhanced fluorescence measurements in analogy to enhanced fluorescence in vicinity of plasmonic nanostructures and metal surfaces [162-167]. Such systems enabling enhanced fluorescence are of great interest in chemical and biological analysis [15, 168]. They have recently become a subject of more extensive studies due to advances in nanotechnology and chip level fluidic systems [169, 170]. A common feature of many previously implemented systems that exhibit enhanced fluorescence is the presence of a plasmonic metal feature. By contrast to these studies, here we demonstrate that practically significant enhanced fluorescence can be achieved in a metal-free system by taking advantage of strong local field enhancement in vicinity of an appropriately designed silicon nanopillar.

Type #5 nanopillar structures were labeled with NHS-rhodamine dye using techniques described in the Materials and Methods Section. The fluorescent image in Figure 5.5 shows a set of NHS-rhodamine labeled nanopillars with average diameters ranging from 95-165 nm (left to right). Each column of nanopillars in Figure 5.5

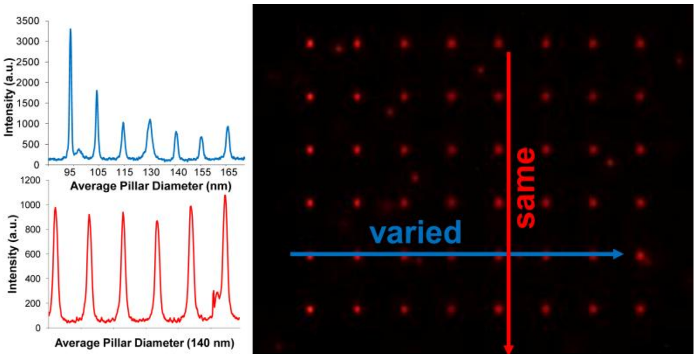

Figure 5.5: Fluorescence image of nanopillars ranging from 95-165 nm in average diameters and coated with NHS-rhodamine. The corresponding intensity plot (blue) correlates well with the trend seen in Figure 5.4. The intensity is also reproducible for a given average diameter (red).

corresponds to the same nominal size. Dramatically increased fluorescence intensity in the regions corresponding to each nanopillar is clearly seen in Figure 5.5. The red fluorescence intensity maximizes in the region occupied by the smallest pillars with an average diameter of 95 nm. Note that an examination of a blank sample with no fluorescent dye was conducted and produced negligible signal (no pillar versus non-pillar difference). The excitation band used to acquire these images is centered at approximately 540 nm. Notably, the 95 nm diameter correlates reasonably well with the results of our FDTD analysis that predicts local field enhancement to maximize at 580 nm for this nanopillar diameter. The fluorescence intensity profile measured across a series of nanopillars with the same targeted diameter of 140 nm indicates excellent reproducibility of the observed enhancement (a relative standard deviation of 7%). The type #5 nanopillar structures produced a raw fluorescence signal enhancement of approximately 35 for each individual pillar (see Figure 5.5). This value compares favorably with many previously demonstrated SEF systems, such as metal nanocomposites [171], silver nanoparticles [172, 173], and thin metal films [174, 175]. While these systems have been proposed for a variety of applications, including protein binding and immunoassays, the observed raw enhancement is generally 10-15 times in the best performing systems [176] with an exception of plasmonic nanostructures similar to SERS-active “hot spots”. Strongest fluorescent enhancement, up to two orders of magnitude, has been achieved by placing a fluorescently labeled sample on a SERS-active substrate in vicinity of a “hot spot” [163].

In order to further demonstrate versatility our approach and its potential for a variety of analytical fluorescence techniques, we prepared a series of nanopillars structures characterized by elliptical cross-sections and labeled them with FITC. In order to fabricate this series of nanopillars, elliptical CAD patterns with two different dimensions and the major axis oriented at incrementally rotated angles were created (depiction at top of Figure 5.6). These elliptical nanopillars were etched using the same RIE recipe as the one used to etch pillars type #5. In addition to demonstrating SEF using another dye, the goal of these experiments was to take advantage of polarization depended resonances in elliptical dielectric resonators. Our hypothesis was that, in case of polarized incident light, effective diameters of elliptical nanopillars will depend on the relative orientation of the polarization plane with respect to the ellipse major axis. This hypothesis was indeed confirmed by our experimental observations. When illuminated by non-polarized light, the fluorescence intensity of individual elliptical pillars was fairly uniform across the array with the incrementally rotated major axis. Under polarized light, however, fluorescence intensity depended noticeably on the major axis orientation. As can be seen in the intensity plots for b and c in Figure 5.6, the horizontal orientation (major axis coinciding with the polarization plane) gave a stronger signal compared to nanopillars with the major axis oriented at arbitrary angles or vertically. Note that both the polarized and non-polarized light yield similar trends in the intensity plots for the circular pillars.

5.3.4 Enhanced Raman of a Thin Sample Layer on Nanopillars

The key strength of Raman spectroscopy is that it provides chemical information about analyzed samples. However, due to extremely small cross-sections of inelastic scattering interactions, Raman spectroscopy is not a sensitive technique unless enhancement of Raman signal is achieved *via* the use of appropriately designed surfaces.

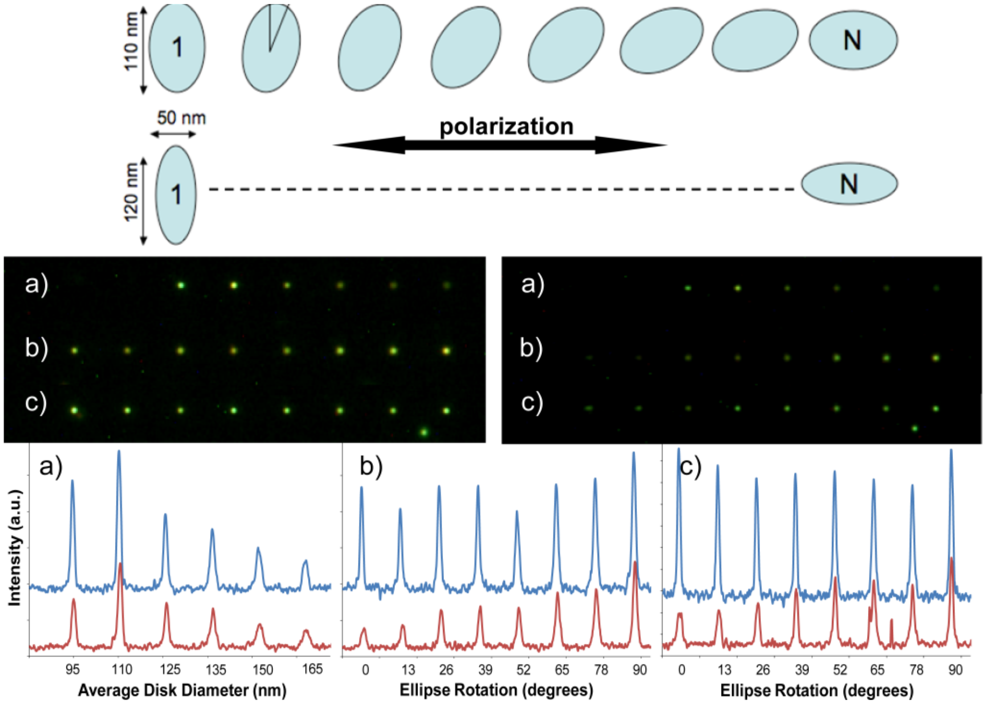

Figure 5.6: Fluorescence images of FITC coated type # 5 nanopillars and two sets of elliptical nanopillars etched using the same RIE recipe. Fluorescence intensity in non-polarized (left image) and polarized (right image) light are shown for (a) type #5 circular pillars with average pillar diameters in the range of 95-165 nm, (b) 110:70 nm elliptical pillars with the incrementally rotated major axis, and (c) 120:50 nm elliptical pillars with the incrementally rotated major axis. The intensity profiles for non-polarized (top blue) and polarized (bottom red) light are shown in the respective a-c panels at bottom.

As such, SERS has become more popular for both chemical and bioanalysis due to the enhanced sensitivity [169]. While SERS is a well established approach that takes advantage of the localized surface plasmon resonance in noble metal nanoparticles and on rough surfaces of noble metals [16, 21], recent theoretical study has indicated that plasmonless SERS may also be possible [177]. The question arises whether the same optical phenomena responsible for enhancement of the silicon Raman line in silicon nanopillars, nanowires and nanocones [178-180] can be utilized to implement this concept and enhance Raman scattering of a thin sample layer on the surface of such silicon nanostructures. In order to address this question, a thin layer of ZnPc was vapor deposited onto chips with nanopillars (type #7) and used as a model analyte with relatively strong Raman scattering. As a result of two deposition steps (see details in the Methods section), approximately 24 nm of ZnPc was deposited on the silicon wafer surrounding the pillars while the thickness of ZnPc layer on the pillar sidewalls had a crescent distribution with estimated maximum and average values of, respectively, 12 and 8 nm.

Figure 5.7 shows a Raman map of the area around a single pillar. Acquisition time of 10 seconds was used for each point. The left side of Figure 5.7 shows the Raman spectrum of ZnPc when the probing beam was focused on the nanopillar while the spectrum on the right shows the off-pillar signal. When the polarization of the probing beam was parallel to the line connecting parts of the nanopillar sidewalls with thickest ZnPc deposits, the on-pillar to off-pillar Raman signal ratio was approximately 20. When the polarization was perpendicular to the deposition direction, the signal ratio was only about 5. The different ratios are consistent with the directional nature of the vapor

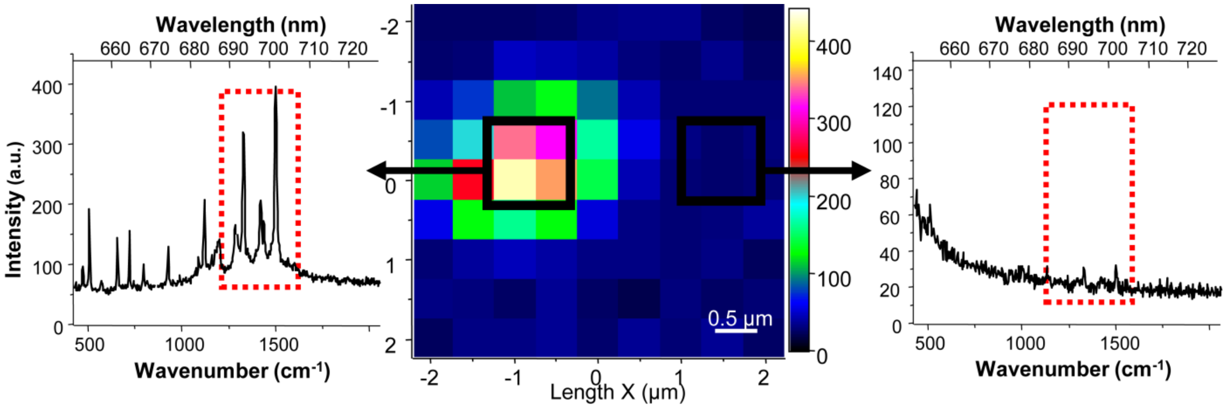

Figure 5.7: Raster experiment is shown at center for the Si pillar type #7 (see SEM in Figure 5.1c and Table 5.1 data) with ~12 nm of ZnPc deposited at 45°, sample rotated 180°, then a second deposition of ~12 nm. Significant bands are highlighted in the Raman spectra for the off-pillar case on the right and the on-pillar case on the left. The ratios of the areas of the on-to-off-pillar 1500 cm^{-1} bands for polarizations that is parallel (shown here) and perpendicular (not shown) to the source-substrate line-of-sight are, respectively, 19.3 and 4.4.

deposition process and presence of crescent-shaped ZnPc deposits on the nanopillar sidewalls.

5.3.5 Enhancement Factor Determination

A nanopillar, area-corrected enhancement factor from the nanopillar structure was determined to assess the analytical utility of this system when scaled-up. As such, EFs were determined for three representative cases: 1) Raman (phonon line of the single crystal Si), 2) SERS (ZnPc), and 3) SEF (NHS-rhodamine). Initially, the average enhancement for the entire pillar structure (type #5) was looked at based on the results from the first silicon Raman line nanopillar trials. Using Equation (5.1), seen in the Experimental section, that compares the raw signal increase (*RSI*), based on the on-versus-off nanopillar signal ratio, and the fractional change in analyte amount due to the nanopillar (ΔAn), the overall EF for the pillar was calculated. Average pillar diameter was used in determining ΔAn. The *RSI* for pillar type #5 was found to be 8.04 (see Table 1) while the ΔAn is based around the assumption that the analyte (silicon material) that is optically probed is approximately 100 nm thick. For this particular pillar set, the EF was found to be ~580. This is a strong enhancement and comparable with that obtained by others [161].

The next set of calculations was based on the nanopillar being an appropriate structure to perform enhanced Raman analysis of a sample layer, in analogy to thin films on SERS active substrates. The known amount of ZnPc deposited onto the surface of the pillar (type #7) made a strong test case. Equation (5.1) was used again and this time the *RSI* was found to be 19.3 at the 1500 cm^{-1} Raman band (Figure 5.7), while the ΔAn is based on the ZnPc thickness on the pillar as well as on the silicon wafer floor. The EF for the pillar type #7, with respect to ZnPc, is found to be ~330. While this is a modest level of enhancement when compared to plasmonic SERS active structures, it is the first convincing demonstration of true non-plasmonic SERS using the light focusing properties of vertical silicon nanopillars without metal. Furthermore, the enhancement reported is averaged over the entire nanopillar structure; EF can be significantly greater when defined specifically for a very small fraction of the nanopillar surface where local field reaches maximum values.

Finally, even though calculating enhancement for SEF is usually conducted as a comparison between signal on and off of the structure, an alternative calculation similar to that of SERS enhancement can also be made with Equation (5.1). For this calculation, the pillar type #5 system with NHS-rhodamine was considered. The *RSI* was found to be approximately 35 as discussed earlier (Figure 5.5). The ΔAn was determined with the assumption that the APTES was coated in an ultra thin layer, basing the calculations on areas for the on-pillar and off-pillar cases. The EF was found to be ~140.

5.4 Conclusions

Using FDTD numerical analysis, we predicted approximately two orders of magnitude enhancements of the local field intensity in the vicinity of appropriately designed and coaxially illuminated individual silicon nanopillars. We implemented such a nanopillar structure using a deterministic, wafer level nanofabrication sequence and for the first time experimentally measured enhanced Raman and fluorescence signals generated in this system in presence of several different model sample materials. The magnitudes of the measured enhanced Raman and SEF signals as well the dependencies of these signals on the nanopillar geometry are generally consistent with our theoretical predictions. The enhancement factors derived from analysis of the acquired fluorescence microscopy images indicate that silicon nanopillar structures can provide enhancement comparable or even stronger than those typically achieved using plasmonic SEF structures. It is anticipated that properly designed and scaled up arrays of silicon nanopillars will enable SEF assays with extremely high sensitivity while also addressing problems, such as oxidation and sulfur poisoning, present in plasmon based SEF systems. However, more detailed theoretical analysis and further experiments are needed in order to gain more comprehensive understanding of the fundamental mechanisms responsible for the observed behaviors.

5.5 Acknowledgements:

A portion of this research was conducted at the Center for Nanophase Materials Sciences, which is sponsored at Oak Ridge National Laboratory by the Office of Basic Energy Sciences, U.S. Department of Energy.

Chapter 6

Concluding remarks

SERS is based on analyte signal enhancement at or near a metallic nanostructured surface. The best performing SERS substrates can generate signal enhancements of better than 10^{11}, generally at highly localized spots ("hot spots"). However, the use of SERS for routine chemical analysis is uncommon. Through a combined effort from a variety of research groups, the potential for broader use as an analytical technique is becoming stronger. A large amount of research focuses on altering the physical characteristics of the substrates since EM enhancement is largely responsible for the SERS effect. Even with the increased attention to substrate development, there remain several qualitative and quantitative limitations to using SERS as a viable analytical tool.

Inhomogeneity of the substrate surface leads to problems with reproducible enhancement. The lack of reproducibility occurs both at the various sites on the surface as well as between different individual substrates. Another common problem is the quick rate of oxidation when the samples are exposed to environmental factors such as air and water. Finally, SERS substrates are often prone to degradation from photolytic or thermal effects. The degradation results in a loss of sensitivity and, potentially, a damaged substrate. Improving these figures of merit has been the focus of Chapters 3 and 4 while focusing on the rational design of SERS substrates. Chapter 5 applied these principles to a plasmonless substrate so as to exploit the signal enhancements present with properly designed silicon structures.

Initial studies altered variables such as size and shape through the use of nanolithographic techniques. However, our current work aimed to create deterministically ordered SERS substrates through rational design. Chapter 3 showed an EBL process combined with RIE to fabricate “random” LDNAs mimicking the features frequently found in metal colloid SERS substrates, the most common substrates for high enhancement. Furthermore, a combinatorial-like procedure was used to help identify areas of enhanced signal.

The controlled nanofabrication method allowed for reproducible creation (“cloning”) of these areas to create large surfaces of large enhancement. It was determined that the surface had enhancement of better than 10^8 over the substrate surface with high reproducibility over the surface. When the system was analyzed with STT [101], the large area was found to give reproducibility of better than 7% RSD. The sensitivity of the sample was also increased due to the robust nature of the substrate. The acquisition time was able to be increased greatly without degradation to either the substrate or the analyte. This increased sample acquisition time allows for an improved LOD as the specific type of sample can withstand greater irradiation than many other types of SERS substrates.

The combinatorial-like approach to SERS substrate fabrication also showed that initial assumptions about particle density as it relates to overall signal enhancement were not always correct. The different sizes and shapes of LDNAs also looked at signal enhancement as it relates to overall density. Contrary to the commonly held belief, the substrates with less than 15% surface coverage from nanoparticles possessed a much stronger raw SERS signal than any of the more densely packed patterns; the signal enhancement, moreover, was even greater as the density of the system was significantly reduced. One of the best ways to understand this unexpected result was through modeling. Unfortunately, the LDNA systems involved a wide range of shapes and features making modeling these systems problematic. A simple, single nanopillar was then created using the same liftoff-RIE process as with the LDNA systems to allow for simple theoretical studies without ions brought on by morphological complexities.

The DOP structures discussed in Chapter 4 were initially based on the best performing LDNA systems with approximately 150 nm diameters. Individual DOP structures were created with more than 20 µm of space surrounding each feature to avoid any long range effects. Furthermore, the experimental goal for this SERS system was to tune the DOP structures to produce the largest EF with the 633 nm LabRam system. The first parameter tested was the height of the DOPs. The overall signal as well as enhancement was strongly tied to the height of the DOP. A large range of enhancement was found depending on the particular pillar height; the strongest enhancement was found to be better than $1x10^9$ at the 175 nm with an RSD of about 25% between individual pillars. The theoretical modeling also showed a similar enhancement disparity between the various DOP heights. Simulations found the optimum height and optical cavity effects to be in line with the experimental results as well.

Additional tuning involved altering DOP diameter while maintaining the appropriate pillar height. The optimum diameter was found to be 100 nm with a Ag thickness of 25 nm on the surface of the substrate. The 100 nm diameter DOP showed a raw signal strength increase of approximately 2 times and reproducibility of better than 18% RSD. The 100 nm diameter pillars also have an overall decrease in size compared to the 150 nm diameter DOPs leading to an improved EF of 4×10^9. The calculated EF for these structures is extremely high for a lithographically fabricated SERS substrate, particularly when reproducibility between individual samples is considered.

Preliminary findings also demonstrated that the LOD could be improved by increasing the number of DOP substrates in a sampling area. A consistent increase in the overall raw signal was observed as the number of pillars increased, but it is anticipated there are limits as high particle density has been shown to be undesirable. Also, the reproducibility improved to better than 10% for the 5x5 DOP arrays. Our collaborators also confirmed that the experimental signals (when normalized) correlated extremely well with the numerically simulated normalized data based on the size of the pillars and the gap between each feature. This means that modeling could be used in the future to better predict how various DOP arrays will react in a given situation and help tune the system to match experimental conditions without the need for trial and error.

Other information gleaned from the DOP trials involved the feasibility of DOP structures for use in a variety of analytical situations. As the DOP structures were etched into the wafer, the potential for photo and thermal degradation was limited. A single pillar was shown to maintain a reproducible spectrum through multiple irradiations without damage to the sample. Furthermore, the DOP system was robust enough to endure removal of Ag with aqua regia and, following a new deposition, produce a strong signal, even if the second analyte was different than the initial test. The DOP system also shows promise for nano-fluidic applications as the substrate has demonstrated the capability for both reversibility and real-time analysis.

Future studies with DOP structures will center on expanding the array work to develop more sensitive substrates. The optimal spacing between features must be determined to create the system that provides the greatest signal strength. This work will also look at extended arrays for larger scale analysis. Still, the larger goal is to develop these DOP arrays into nano-fluidic systems for SERS detection.

Chapter 5 used the information gained from the DOP work to begin creating silicon nanopillars for analysis without plasmonic properties. FDTD analysis from collaborators predicted enhancements in localized fields near optimized silicon nanopillars of approximately 2 orders of magnitude. As such, high aspect ratio nanopillars of various shapes, sizes, and heights were created. Analysis of the silicon Raman phonon line demonstrated that the silicon nanopillars produced field enhancements consistent with those predictions.

These silicon nanopillar structures also demonstrated the ability to improve Raman analysis without plasmonic particles. A single nanopillar produced an increased Raman spectrum yielding enhancement of better than 300 with a thin layer of ZnPc deposited onto the surface. While this is not close to the potential EF of SERS substrates, the silicon nanopillars demonstrate the ability to improve Raman signal without many of the limitations of SERS, namely inhomogeneity and rapid oxidation. These silicon nanopillars were also labeled with various fluorophors for potential SEF capabilities. Not only was it observed that every silicon nanopillar was able to be fluorescently labeled, but the calculated EF was comparable or stronger than those often achieved with plasmonic SEF systems. Fluorescence detection is the most likely area of detection for this type of silicon nanopillar system.

Future work in this area will focus on further developing silicon nanopillars and creating arrays of these structures. It is anticipated that arrays will behave similarly in an array form as the DOP arrays did by increasing overall signal. We will also try to identify the optimum etching protocol and pillar spacing for these arrays to achieve the greatest enhancement. From here, continued projects will probably focus on fluorescence detection. A sandwich fluroamino assay approach may be attempted to detect labeled biomolecules. Lastly, a passive flow fluidics system for fluorescence detection could be fabricated to detect a variety of analytes in low concentrations.

Bibliography

[1] Kahl, M., Voges, E., Kostrewa, S., Viets, C. and Hill, W. Periodically structured metallic substrates for SERS. *Sensors and Actuators B-Chemical*, 51, 1-3 (Aug 31 1998), 285-291.

[2] Vo-Dinh, T. Surface-enhanced Raman spectroscopy using metallic nanostructures. *Trac-Trends in Analytical Chemistry*, 17, 8-9 (Sep-Oct 1998), 557-582.

[3] Smekal, A. Zur Quantentheorie der Dispersion. *Die Naturwissenschaften*, 43(1923 1923), 873-875.

[4] Raman, C. V. and Krishnan, K. S. A new type of secondary radiation. *Nature*, 121(Jan-Jun 1928), 501-502.

[5] Raman, C. V. A New Radiation. *Indian Journal of Physics*, 2(1928 1928), 388-398.

[6] Placzek, G. *Rayleigh-Streuung und Raman-Effekt*. Akademische Verlagsgesellschaft, Lezpig, 1934.

[7] Dennis Strommen, K. N. *Laboratory Raman Spectroscopy*. Wiley-Interscience, New York, 1984.

[8] Szymanski, H. A. *Raman Spectroscopy: Theory and Practice*. Plenum Press, Buffalo, NY, 1967.

[9] D.A. Skoog, F. J. H., S.R. Crouch *Principles of Instrumental Analysis*. Thompson higher Education, Belmont, CA, 2007.

[10] Hendra, J. P. *Raman Instrumentation and Sampling*. Heyden, London, 1972.

[11] Bowie, B. T., Chase, D. B. and Griffiths, P. R. Factors affecting the performance of bench-top Raman spectrometers. Part I: Instrumental effects. *Applied Spectroscopy*, 54, 5 (May 2000), 164A-173A.

[12] Pitt, G. D., Batchelder, D. N., Bennett, R., Bormett, R. W., Hayward, I. P., Smith, B. J. E., Williams, K. P. J., Yang, Y. Y., Baldwin, K. J. and Webster, S. Engineering aspects and applications of the new Raman instrumentation. *Iee Proceedings-Science Measurement and Technology*, 152, 6 (Nov 2005), 241-318.

[13] Laplant, F. and Benamotz, D. DESIGN AND CONSTRUCTION OF A MICROSCOPE-BASED RAMAN SYSTEM. *Review of Scientific Instruments*, 66, 6 (Jun 1995), 3537-3544.

[14] Shorygin, P. P. and Krushinskij, L. L. Early days and later development of resonance Raman spectroscopy. *Journal of Raman Spectroscopy*, 28, 6 (Jun 1997), 383-388.

[15] Nicholas Pieczonka, P. G., Ricardo Aroca *Applications of the Enhancement of Resonance Raman Scattering and Fluorescence by Strongly Coupled Metallic Nanostructures*. Springer, Berlin, Germany, 2006.

[16] George Schatz, M. Y., Richard Van Duyne *Electromagnetic Mechanism of SERS*. Springer, Berlin, Germany, 2006.

[17] Campion, A. and Kambhampati, P. Surface-enhanced Raman scattering. *Chemical Society Reviews*, 27, 4 (Jul 1998), 241-250.

[18] Fleischm.M, Hendra, P. J. and McQuilla.Aj RAMAN-SPECTRA OF PYRIDINE ADSORBED AT A SILVER ELECTRODE. *Chemical Physics Letters*, 26, 2 (1974 1974), 163-166.

[19] Jeanmaire, D. L. and Vanduyne, R. P. SURFACE RAMAN SPECTROELECTROCHEMISTRY .1. HETEROCYCLIC, AROMATIC, AND ALIPHATIC-AMINES ADSORBED ON ANODIZED SILVER ELECTRODE. *Journal of Electroanalytical Chemistry*, 84, 1 (1977 1977), 1-20.

[20] Albrecht, M. G. and Creighton, J. A. ANOMALOUSLY INTENSE RAMAN-SPECTRA OF PYRIDINE AT A SILVER ELECTRODE. *Journal of the American Chemical Society*, 99, 15 (1977 1977), 5215-5217.

[21] Moskovits, M. SURFACE-ENHANCED SPECTROSCOPY. *Reviews of Modern Physics*, 57, 3 (1985 1985), 783-826.

[22] Schatz, G. C. THEORETICAL-STUDIES OF SURFACE ENHANCED RAMAN-SCATTERING. *Accounts of Chemical Research*, 17, 10 (1984 1984), 370-376.

[23] Kambhampati, P., Child, C. M., Foster, M. C. and Campion, A. On the chemical mechanism of surface enhanced Raman scattering: Experiment and theory. *Journal of Chemical Physics*, 108, 12 (Mar 22 1998), 5013-5026.

[24] Xu, H. X., Aizpurua, J., Kall, M. and Apell, P. Electromagnetic contributions to single-molecule sensitivity in surface-enhanced Raman scattering. *Physical Review E*, 62, 3 (Sep 2000), 4318-4324.

[25] Li, K. R., Li, X. T., Stockman, M. I. and Bergman, D. J. Surface plasmon amplification by stimulated emission in nanolenses. *Physical Review B*, 71, 11 (Mar 2005).

[26] Bello, J. M. and Vodinh, T. SURFACE-ENHANCED RAMAN-SCATTERING FIBEROPTIC SENSOR. *Applied Spectroscopy*, 44, 1 (Jan 1990), 63-69.

[27] GarciaVidal, F. J. and Pendry, J. B. Collective theory for surface enhanced Raman scattering. *Physical Review Letters*, 77, 6 (Aug 5 1996), 1163-1166.

[28] Oubre, C. and Nordlander, P. Finite-difference time-domain studies of the optical properties of nanoshell dimers. *Journal of Physical Chemistry B*, 109, 20 (May 26 2005), 10042-10051.

[29] Knoll, W. Interfaces and thin films as seen by bound electromagnetic waves. *Annual Review of Physical Chemistry*, 49(1998 1998), 569-638.

[30] Kelly, K. L., Coronado, E., Zhao, L. L. and Schatz, G. C. The optical properties of metal nanoparticles: The influence of size, shape, and dielectric environment. *Journal of Physical Chemistry B*, 107, 3 (Jan 23 2003), 668-677.

[31] Reilly, T. H., III, Corbman, J. D. and Rowlen, K. L. Vapor deposition method for sensitivity studies on engineered surface-enhanced Raman scattering-active substrates. *Analytical Chemistry*, 79, 13 (Jul 1 2007), 5078-5081.

[32] Pablo Etchegoin, E. L. R. *Basic Electromagnetic Theory of SERS*. Wiley, Weinheim, Germany, 2011.

[33] Etchegoin, P. G. and Le Ru, E. C. A perspective on single molecule SERS: current status and future challenges. *Physical Chemistry Chemical Physics*, 10, 40 2008), 6079-6089.

[34] Anker, J. N., Hall, W. P., Lyandres, O., Shah, N. C., Zhao, J. and Van Duyne, R. P. Biosensing with plasmonic nanosensors. *Nature Materials*, 7, 6 (Jun 2008), 442-453.

[35] Schmidt, H., Ha, N. B., Pfannkuche, J., Amann, H., Kronfeldt, H. D. and Kowalewska, G. Detection of PAHs in seawater using surface-enhanced Raman scattering (SERS). *Marine Pollution Bulletin,* 49, 3 (Aug 2004), 229-234.

[36] Farquharson, S. and Maksymiuk, P. Simultaneous chemical separation and surface-enhanced Raman spectral detection using silver-doped sol-gels. *Applied Spectroscopy*, 57, 4 (Apr 2003), 479-482.

[37] Pavel, I., Cota, S., Cinta-Pinzaru, S. and Kiefer, W. Raman, surface enhanced Raman spectroscopy, and DFT calculations: A powerful approach for the

identification and characterization of 5-fluorouracil anticarcinogenic drug species. *Journal of Physical Chemistry A*, 109, 44 (Nov 10 2005), 9945-9952.

[38] Kranich, A., Naumann, H., Molina-Heredia, F. P., Moore, H. J., Lee, T. R., Lecomte, S., de la Rosa, M. A., Hildebrandt, P. and Murgida, D. H. Gated electron transfer of cytochrome c(6) at biomimetic interfaces: a time-resolved SERR study. *Physical Chemistry Chemical Physics*, 11, 34 (2009 2009), 7390-7397.

[39] Marras, S. A. E., Gold, B., Kramer, F. R., Smith, I. and Tyagi, S. Real-time measurement of in vitro transcription. *Nucleic Acids Research*, 32, 9 (May 2004).

[40] Wang, H.-N. and Vo-Dinh, T. Multiplex detection of breast cancer biomarkers using plasmonic molecular sentinel nanoprobes. *Nanotechnology*, 20, 6 (Feb 11 2009).

[41] E. Le Ru, P. E. *Principles of Surface-Enhanced Raman Spectroscopy and Related Plasmonic Effects*. Elsevier, 2009.

[42] Hao, E. and Schatz, G. C. Electromagnetic fields around silver nanoparticles and dimers. *Journal of Chemical Physics*, 120, 1 2004), 357-366.

[43] Natan, M. J., City, 2006.

[44] Kneipp, K., Wang, Y., Kneipp, H., Perelman, L. T., Itzkan, I., Dasari, R. and Feld, M. S. Single molecule detection using surface-enhanced Raman scattering (SERS). *Physical Review Letters*, 78, 9 (Mar 3 1997), 1667-1670.

[45] Tian, Z. Q., Ren, B. and Wu, D. Y. Surface-enhanced Raman scattering: From noble to transition metals and from rough surfaces to ordered nanostructures. *Journal of Physical Chemistry B*, 106, 37 (Sep 19 2002), 9463-9483.

[46] Vanduyne, R. P., Hulteen, J. C. and Treichel, D. A. ATOMIC-FORCE MICROSCOPY AND SURFACE-ENHANCED RAMAN-SPECTROSCOPY .1.

AG ISLAND FILMS AND AG FILM OVER POLYMER NANOSPHERE SURFACES SUPPORTED ON GLASS. *Journal of Chemical Physics*, 99, 3 (Aug 1 1993), 2101-2115.

[47] Giesfeldt, K. S., Connatser, R. M., De Jesus, M. A., Lavrik, N. V., Dutta, P. and Sepaniak, M. J. Studies of the optical properties of metal-pliable polymer composite materials. *Applied Spectroscopy*, 57, 11 (Nov 2003), 1346-1352.

[48] De Jesus, M. A., Giesfeldt, K. S. and Sepaniak, M. J. Factors affecting the sorption of model environmental pollutants onto silver polydimethylsiloxane nanocomposite Raman substrates. *Applied Spectroscopy*, 58, 10 (Oct 2004), 1157-1164.

[49] Kneipp, K., Kneipp, H., Itzkan, I., Dasari, R. R. and Feld, M. S. Ultrasensitive chemical analysis by Raman spectroscopy. *Chemical Reviews*, 99, 10 (Oct 1999), 2957-+.

[50] Aroca, R. F., Alvarez-Puebla, R. A., Pieczonka, N., Sanchez-Cortez, S. and Garcia-Ramos, J. V. Surface-enhanced Raman scattering on colloidal nanostructures. *Advances in Colloid and Interface Science*, 116, 1-3 (Nov 30 2005), 45-61.

[51] Nie, S. M. and Emery, S. R. Probing single molecules and single nanoparticles by surface-enhanced Raman scattering. *Science*, 275, 5303 (Feb 21 1997), 1102-1106.

[52] Michaels, A. M., Nirmal, M. and Brus, L. E. Surface enhanced Raman spectroscopy of individual rhodamine 6G molecules on large Ag nanocrystals. *Journal of the American Chemical Society*, 121, 43 (Nov 3 1999), 9932-9939.

[53] Weiss, A. and Haran, G. Time-dependent single-molecule Raman scattering as a probe of surface dynamics. *Journal of Physical Chemistry B*, 105, 49 (Dec 13 2001), 12348-12354.

[54] Camden, J. P., Dieringer, J. A., Zhao, J. and Van Duyne, R. P. Controlled Plasmonic Nanostructures for Surface-Enhanced Spectroscopy and Sensing. *Accounts of Chemical Research*, 41, 12 (Dec 2008), 1653-1661.

[55] Khan, I., Cunningham, D., Graham, D., McComb, D. W. and Smith, W. E. Identification and characterization of active and inactive species for surface-enhanced resonance Raman scattering. *Journal of Physical Chemistry B*, 109, 8 (Mar 3 2005), 3454-3459.

[56] Camden, J. P., Dieringer, J. A., Wang, Y., Masiello, D. J., Marks, L. D., Schatz, G. C. and Van Duyne, R. P. Probing the structure of single-molecule surface-enhanced Raman scattering hot spots. *Journal of the American Chemical Society*, 130, 38 (Sep 24 2008), 12616-+.

[57] Fan, M., Andrade, G. F. S. and Brolo, A. G. A review on the fabrication of substrates for surface enhanced Raman spectroscopy and their applications in analytical chemistry. *Analytica Chimica Acta*, 693, 1-2 (May 5 2011), 7-25.

[58] Yang, P., Yan, R. and Fardy, M. Semiconductor Nanowire: What's Next? *Nano Letters*, 10, 5 (May 2010), 1529-1536.

[59] Lin, X.-M., Cui, Y., Xu, Y.-H., Ren, B. and Tian, Z.-Q. Surface-enhanced Raman spectroscopy: substrate-related issues. *Analytical and Bioanalytical Chemistry*, 394, 7 (Aug 2009), 1729-1745.

[60] Grabar, K. C., Smith, P. C., Musick, M. D., Davis, J. A., Walter, D. G., Jackson, M. A., Guthrie, A. P. and Natan, M. J. Kinetic control of interparticle spacing in Au colloid-based surfaces: Rational nanometer-scale architecture. *Journal of the American Chemical Society*, 118, 5 (Feb 7 1996), 1148-1153.

[61] Roberts, G. *Lagnmuir Blodgett Films*. Plenum, New York, 1990.

[62] Mollenstedt, G. *Important problems of the electron microscope*, 1961.

[63] Mulvihill, M., Tao, A., Benjauthrit, K., Arnold, J. and Yang, P. Surface-enhanced Raman spectroscopy for trace arsenic detection in contaminated water. *Angewandte Chemie-International Edition*, 47, 34 (2008 2008), 6456-6460.

[64] Hulteen, J. C. and Vanduyne, R. P. NANOSPHERE LITHOGRAPHY - A MATERIALS GENERAL FABRICATION PROCESS FOR PERIODIC PARTICLE ARRAY SURFACES. *Journal of Vacuum Science & Technology a-Vacuum Surfaces and Films*, 13, 3 (May-Jun 1995), 1553-1558.

[65] Willets, K. A. and Van Duyne, R. P. *Localized surface plasmon resonance spectroscopy and sensing*. City, 2007.

[66] Tennant, D. M. *Limits of Conventional Lithography*. Springer, New York, 1999.

[67] Howard, R. E., Craighead, H. G., Jackel, L. D., Mankiewich, P. M. and Feldman, M. ELECTRON-BEAM LITHOGRAPHY FROM 20 TO 120 KEV WITH A HIGH-QUALITY BEAM. *Journal of Vacuum Science & Technology B*, 1, 4 (1983 1983), 1101-1104.

[68] Tseng, A. A. Recent developments in nanofabrication using focused ion beams. *Small*, 1, 10 (Sep 2005), 924-939.

[69] Brolo, A. G., Gordon, R., Leathem, B. and Kavanagh, K. L. Surface plasmon sensor based on the enhanced light transmission through arrays of nanoholes in gold films. *Langmuir*, 20, 12 (Jun 8 2004), 4813-4815.

[70] Brolo, A. G., Arctander, E., Gordon, R., Leathem, B. and Kavanagh, K. L. Nanohole-enhanced Raman scattering. *Nano Letters*, 4, 10 (Oct 2004), 2015-2018.

[71] Tseng, A. A. and Notargiacomo, A. Nanoscale fabrication by nonconventional approaches. *Journal of Nanoscience and Nanotechnology*, 5, 5 (May 2005), 683-702.

[72] Wilbur, J. L. W., G.M. *Self-assembly and Self-assembled Monolayers in Micro and Nanofabrication*. Springer, New York, 1999.

[73] Yamazake, K. *Electron beam direct writing*. World Scientific, Hackensack, NJ, 2008.

[74] Pfeiffer, H. C. VARIABLE SPOT SHAPING FOR ELECTRON-BEAM LITHOGRAPHY. *Journal of Vacuum Science & Technology*, 15, 3 (1978 1978), 887-890.

[75] Berger, S. D., Gibson, J. M., Camarda, R. M., Farrow, R. C., Huggins, H. A., Kraus, J. S. and Liddle, J. A. PROJECTION ELECTRON-BEAM LITHOGRAPHY - A NEW APPROACH. *Journal of Vacuum Science & Technology B*, 9, 6 (Nov-Dec 1991), 2996-2999.

[76] Pfeiffer, H. C. and Stickel, W. PREVAIL - AN E-BEAM STEPPER WITH VARIABLE AXIS IMMERSION LENSES. *Microelectronic Engineering*, 27, 1-4 (Feb 1995), 143-146.

[77] Utsumi, T. Low-energy e-beam proximity lithography (LEEPL): Is the simplest the best? *Japanese Journal of Applied Physics Part 1-Regular Papers Short Notes & Review Papers*, 38, 12B (Dec 1999), 7046-7051.

[78] Saitou, N. Electron beam lithography - Present and future. *International Journal of the Japan Society for Precision Engineering*, 30, 2 (Jun 1996), 107-111.

[79] Murata, K., Kyser, D. F. and Ting, C. H. MONTE-CARLO SIMULATION OF FAST SECONDARY-ELECTRON PRODUCTION IN ELECTRON-BEAM RESISTS. *Journal of Applied Physics*, 52, 7 (1981 1981), 4396-4405.

[80] Namatsu, H., Nagase, M., Kurihara, K., Iwadate, K., Furuta, T. and Murase, K. FABRICATION OF SUB-10-NM SILICON LINES WITH MINIMUM

FLUCTUATION. *Journal of Vacuum Science & Technology B*, 13, 4 (Jul-Aug 1995), 1473-1476.

[81] De Jesus, M. A., Giesfeldt, K. S., Oran, J. M., Abu-Hatab, N. A., Lavrik, N. V. and Sepaniak, M. J. Nanofabrication of densely packed metal-polymer arrays for surface-enhanced Raman spectrometry. *Applied Spectroscopy*, 59, 12 (Dec 2005), 1501-1508.

[82] Gunnarsson, L., Bjerneld, E. J., Xu, H., Petronis, S., Kasemo, B. and Kall, M. Interparticle coupling effects in nanofabricated substrates for surface-enhanced Raman scattering. *Applied Physics Letters*, 78, 6 (Feb 5 2001), 802-804.

[83] Yu, Q., Guan, P., Qin, D., Golden, G. and Wallace, P. M. Inverted size-dependence of surface-enhanced Raman scattering on gold nanohole and nanodisk arrays. *Nano Letters*, 8, 7 (Jul 2008), 1923-1928.

[84] Im, H., Bantz, K. C., Lindquist, N. C., Haynes, C. L. and Oh, S.-H. Vertically Oriented Sub-10-nm Plasmonic Nanogap Arrays. *Nano Letters*, 10, 6 (Jun 2010), 2231-2236.

[85] Mack, C. *Introduction to Semiconductor Lithography*. Wiley, Hoboken, NJ, 2007.

[86] Otto, A. *Light Scattering in Solids*, Berlin, 1984.

[87] Otto, A., Mrozek, I., Grabhorn, H. and Akemann, W. SURFACE-ENHANCED RAMAN-SCATTERING. *J. Phys.-Condes. Matter*, 4, 5 (Feb 3 1992), 1143-1212.

[88] Wokaun, A. SURFACE-ENHANCED ELECTROMAGNETIC PROCESSES. *Solid State Physics-Advances in Research and Applications*, 38(1984 1984), 223-294.

[89] Ritchie, R. H. PLASMA LOSSES BY FAST ELECTRONS IN THIN FILMS. *Physical Review*, 106, 5 (1957 1957), 874-881.

[90] Green, M. and Liu, F. M. SERS substrates fabricated by island lithography: The silver/pyridine system. *Journal of Physical Chemistry B*, 107, 47 (Nov 27 2003), 13015-13021.

[91] Kaminska, A., Inya-Agha, O., Forster, R. J. and Keyes, T. E. Chemically bound gold nanoparticle arrays on silicon: assembly, properties and SERS study of protein interactions. *Physical Chemistry Chemical Physics*, 10, 28 2008), 4172-4180.

[92] Yan, B., Thubagere, A., Premasiri, W. R., Ziegler, L. D., Dal Negro, L. and Reinhard, B. M. Engineered SERS Substrates With Multiscale Signal Enhancement: Nanoplarticle Cluster Arrays. *Acs Nano*, 3, 5 (May 2009), 1190-1202.

[93] Emory, S. R. and Nie, S. M. Near-field surface-enhanced Raman spectroscopy on single silver nanoparticles. *Analytical Chemistry*, 69, 14 (Jul 15 1997), 2631-2635.

[94] Michaels, A. M., Jiang, J. and Brus, L. Ag nanocrystal junctions as the site for surface-enhanced Raman scattering of single Rhodamine 6G molecules. *Journal of Physical Chemistry B*, 104, 50 (Dec 21 2000), 11965-11971.

[95] Markel, V. A., Shalaev, V. M., Zhang, P., Huynh, W., Tay, L., Haslett, T. L. and Moskovits, M. Near-field optical spectroscopy of individual surface-plasmon modes in colloid clusters. *Physical Review B*, 59, 16 (Apr 15 1999), 10903-10909.

[96] Li, H. G. and Cullum, B. M. Dual layer and multilayer enhancements from silver film over nanostructured surface-enhanced Raman substrates. *Applied Spectroscopy*, 59, 4 (Apr 2005), 410-417.

[97] Abu Hatab, N. A., Oran, J. M. and Sepaniak, M. J. Surface-enhanced Raman spectroscopy substrates created via electron beam lithography and nanotransfer printing. *Acs Nano*, 2, 2 (Feb 2008), 377-385.

[98] Oran, J. M., Hinde, R. J., Abu Hatab, N., Retterer, S. T. and Sepaniak, M. J. Nanofabricated periodic arrays of silver elliptical discs as SERS substrates. *Journal of Raman Spectroscopy*, 39, 12 2008), 1811-1820.

[99] Alexander, T. A. W., A.E. *Electron-beam lithography (EBL)-engineered nanostructures for biosensing*. City, 2004.

[100] Abu-Hatab, N. A., John, J. F., Oran, J. M. and Sepaniak, M. J. Multiplexed microfluidic surface-enhanced Raman spectroscopy. *Applied Spectroscopy*, 61, 10 (Oct 2007), 1116-1122.

[101] De Jesus, M. A., Giesfeldt, K. S. and Sepaniak, M. J. Use of a Sample Translation Technique to Minimize Adverse Effects of Laser Irradiation in Surface-Enhanced Raman Spectrometry. *Applied Spectroscopy*, 57, 4 2003), 428-438.

[102] Bhandari, D., Walworth, M. J. and Sepaniak, M. J. Dual Function Surface-Enhanced Raman Active Extractor for the Detection of Environmental Contaminants. *Applied Spectroscopy*, 63, 5 (May 2009), 571-578.

[103] Schoenfisch, M. H. and Pemberton, J. E. Air stability of alkanethiol self-assembled monolayers on silver and gold surfaces. *Journal of the American Chemical Society*, 120, 18 (May 13 1998), 4502-4513.

[104] Han, S. W., Lee, S. J. and Kim, K. Self-assembled monolayers of aromatic thiol and selenol on silver: Comparative study of adsorptivity and stability. *Langmuir*, 17, 22 (Oct 30 2001), 6981-6987.

[105] Bijeon, J. L., Royer, P., Goudonnet, J. P., Warmack, R. J. and Ferrell, T. L. EFFECTS OF A SILICON SUBSTRATE ON SURFACE-PLASMON SPECTRA IN SILVER ISLAND FILMS. *Thin Solid Films*, 155, 1 (Dec 15 1987), L1-L3.

[106] Daniels, J. K. and Chumanov, G. Nanoparticle-mirror sandwich substrates for surface-enhanced Raman scattering. *Journal of Physical Chemistry B*, 109, 38 (Sep 29 2005), 17936-17942.

[107] Kinnan, M. K. and Chumanov, G. Surface enhanced Raman scattering from silver nanoparticle arrays on silver mirror films: Plasmon-induced electronic coupling as the enhancement mechanism. *Journal of Physical Chemistry C*, 111, 49 (Dec 13 2007), 18010-18017.

[108] Le Ru, E. C., Blackie, E., Meyer, M. and Etchegoin, P. G. Surface enhanced Raman scattering enhancement factors: a comprehensive study. *Journal of Physical Chemistry C*, 111, 37 (Sep 20 2007), 13794-13803.

[109] Haynes, C. L. and Van Duyne, R. P. Plasmon-sampled surface-enhanced Raman excitation spectroscopy. *Journal of Physical Chemistry B*, 107, 30 2003), 7426-7433.

[110] Wan, L. J., Terashima, M., Noda, H. and Osawa, M. Molecular orientation and ordered structure of benzenethiol adsorbed on gold(111). *Journal of Physical Chemistry B*, 104, 15 (Apr 20 2000), 3563-3569.

[111] Whelan, C. M., Smyth, M. R. and Barnes, C. J. HREELS, XPS, and electrochemical study of benzenethiol adsorption on Au(111). *Langmuir*, 15, 1 1999), 116-126.

[112] Xu, H. X., Bjerneld, E. J., Kall, M. and Borjesson, L. Spectroscopy of single hemoglobin molecules by surface enhanced Raman scattering. *Physical Review Letters*, 83, 21 (Nov 22 1999), 4357-4360.

[113] Khan, I., Polwart, E., McComb, D. W. and Smith, W. E. Correlation of optical properties with structure of immoblised nanoparticles - a method for probing the mechanism of SERRS. *Analyst*, 129, 10 (2004 2004), 950-955.

[114] McFarland, A. D., Young, M. A., Dieringer, J. A. and Van Duyne, R. P. Wavelength-scanned surface-enhanced Raman excitation spectroscopy. *Journal of Physical Chemistry B*, 109, 22 (Jun 9 2005), 11279-11285.

[115] Dick, L. A., McFarland, A. D., Haynes, C. L. and Van Duyne, R. P. Metal film over nanosphere (MFON) electrodes for surface-enhanced Raman spectroscopy (SERS): Improvements in surface nanostructure stability and suppression of irreversible loss. *Journal of Physical Chemistry B*, 106, 4 (Jan 31 2002), 853-860.

[116] Oubre, C. and Nordlander, P. Finite-difference time-domain studies of the optical properties of nanoshell dimers. *Journal of Physical Chemistry B*, 1092005), 10042-10051.

[117] Shuford, K. L., Lee, J., Odom, T. W. and Schatz, G. C. Optical properties of gold pyramidal shells. *Journal of Physical Chemistry C*, 112, 17 2008), 6662-6666.

[118] Gopinath, A., Boriskina, S. V., Reinhard, B. M. and Dal Negro, L. Deterministic aperiodic arrays of metal nanoparticles for surface-enhanced Raman scattering (SERS). *Optics Express*, 17, 5 2009), 3741-3753.

[119] Murphy, C. J., San, T. K., Gole, A. M., Orendorff, C. J., Gao, J. X., Gou, L., Hunyadi, S. E. and Li, T. Anisotropic metal nanoparticles: Synthesis, assembly, and optical applications. *Journal of Physical Chemistry B*, 109, 29 2005), 13857-13870.

[120] Doering, W. E. and Nie, S. M. Single-molecule and single-nanoparticle SERS: Examining the roles of surface active sites and chemical enhancement. *Journal of Physical Chemistry B*, 106, 2 2002), 311-317.

[121] Fang, Y., Seong, N. H. and Dlott, D. D. Measurement of the distribution of site enhancements in surface-enhanced Raman scattering. *Science*, 321, 5887 (Jul 2008), 388-392.

[122] Chen, C. Y. and Burstein, E. GIANT RAMAN-SCATTERING BY MOLECULES AT METAL-ISLAND FILMS. *Phys. Rev. Lett.*, 45, 15 1980), 1287-1291.

[123] Yu, Q. M., Guan, P., Qin, D., Golden, G. and Wallace, P. M. Inverted size-dependence of surface-enhanced Raman scattering on gold nanohole and nanodisk arrays. *Nano Letters*, 8, 7 2008), 1923-1928.

[124] Hu, E. L., Tennant, D. M., Howard, R. E., Jackel, L. D. and Grabbe, P. VERTICAL SILICON MEMBRANE ARRAYS PATTERNED WITH TRI-LEVEL E-BEAM RESIST. *Journal of Electronic Materials*, 11, 5 1982), 883-888.

[125] Haynes, C. L., McFarland, A. D. and Van Duyne, R. P. Surface-enhanced Raman spectroscopy. *Analytical Chemistry*, 77, 17 2005), 338A-346A.

[126] De Jesus, M. A., Giesfeldt, K. S., Oran, J. M., Abu-Hatab, N. A., Lavrik, N. V. and Sepaniak, M. J. Nanofabrication of densely packed metal-polymer arrays for surface-enhanced Raman spectrometry. *Applied Spectroscopy*, 592005), 1501-1508.

[127] Wells, S. M., Retterer, S. D., Oran, J. M. and Sepaniak, M. J. Controllable Nanotabrication of Aggregate-like Nanoparticle Substrates and Evaluation for Surface-Enhanced Raman Spectroscopy. *Acs Nano*, 3, 12 (Dec 2009), 3845-3853.

[128] Xu, H. X. and Kall, M. Estimating SERS properties of silver-particle aggregates through generalized Mie theory. *Surface-Enhanced Raman Scattering: Physics and Applications*, 1032006), 87-103.

[129] Polemi, A. W., S.M.; Lavrik, N.V.; Sepaniak, M.J.; Shuford, K.L. Local Field Enhancement of Pillar Nanosurfaces for SERS. *Journal of Physical Chemistry C,* 114, 42 2010), 18096-18102.

[130] Gopinath, A., Boriskina, S. V., Premasiri, W. R., Ziegler, L., Reinhard, B. M. and Dal Negro, L. Plasmonic Nanogalaxies: Multiscale Aperiodic Arrays for Surface-Enhanced Raman Sensing. *Nano Letters*, 9, 11 2009), 3922-3929.

[131] Weiland, T. DISCRETIZATION METHOD FOR SOLUTION OF MAXWELLS EQUATIONS FOR 6-COMPONENT FIELDS. *Aeu-International Journal of Electronics and Communications*, 31, 3 1977), 116-120.

[132] Palik, E. *Handbook of Optical Constraint of Solids*. Academic Press, Orlando, 1985.

[133] Polemi, A., Wells, S. M., Lavrik, N. V., Sepaniak, M. J. and Shuford, K. L. Dispersion Characteristics in Disk-on-Pillar Array Nanostructures for Surface-Enhanced Raman Spectroscopy. *Journal of Physical Chemistry C*, 115, 28 (Jul 21 2011), 13624-13629.

[134] Barhoumi, A., Zhang, D., Tam, F. and Halas, N. J. Surface-enhanced Raman spectroscopy of DNA. *Journal of the American Chemical Society*, 130, 16 2008), 5523-5529.

[135] Garnett, E. C., Brongersma, M. L., Cui, Y. and McGehee, M. D. Nanowire Solar Cells. *Annual Review of Materials Research*, 41, 1 2011), 269-295.

[136] Fan, Z. Y., Kapadia, R., Leu, P. W., Zhang, X. B., Chueh, Y. L., Takei, K., Yu, K., Jamshidi, A., Rathore, A. A., Ruebusch, D. J., Wu, M. and Javey, A. Ordered Arrays of Dual-Diameter Nanopillars for Maximized Optical Absorption. *Nano Letters*, 10, 10 (Oct 2010), 3823-3827.

[137] Cao, L. Y., Fan, P. Y., Vasudev, A. P., White, J. S., Yu, Z. F., Cai, W. S., Schuller, J. A., Fan, S. H. and Brongersma, M. L. Semiconductor Nanowire Optical Antenna Solar Absorbers. *Nano Letters*, 10, 2 (Feb 2010), 439-445.

[138] Sivakov, V., Andrae, G., Gawlik, A., Berger, A., Plentz, J., Falk, F. and Christiansen, S. H. Silicon Nanowire-Based Solar Cells on Glass: Synthesis, Optical Properties, and Cell Parameters. *Nano Letters*, 9, 4 (Apr 2009), 1549-1554.

[139] Cao, L. Y., White, J. S., Park, J. S., Schuller, J. A., Clemens, B. M. and Brongersma, M. L. Engineering Light Absorption in Semiconductor Nanowire Devices. *Nature Materials*, 8, 8 (Aug 2009), 643-647.

[140] Tian, B., Zheng, X., Kempa, T. J., Fang, Y., Yu, N., Yu, G., Huang, J. and Lieber, C. M. Coaxial Silicon Nanowires as Solar Cells and Nanoelectronic Power Sources. *Nature*, 449, 7164 (Oct 18 2007), 885-U888.

[141] Servati, P., Colli, A., Hofmann, S., Fu, Y. Q., Beecher, P., Durrani, Z. A. K., Ferrari, A. C., Flewitt, A. J., Robertson, J. and Milne, W. I. Scalable Silicon Nanowire Photodetectors. *Physica E-Low-Dimensional Systems & Nanostructures*, 38, 1-2 (Apr 2007), 64-66.

[142] Yang, C., Barrelet, C. J., Capasso, F. and Lieber, C. M. Single P-Type/Intrinsic/N-Type Silicon Nanowires as Nanoscale Avalanche Photodetectors. *Nano Letters*, 6, 12 (Dec 13 2006), 2929-2934.

[143] Canham, L. T. Silicon Quantum Wire Array Fabrication by Electrochemical and Chemical Dissolution of Wafers. *Applied Physics Letters*, 57, 10 (Sep 3 1990), 1046-1048.

[144] Hu, J. T., Odom, T. W. and Lieber, C. M. Chemistry and Physics in One Dimension: Synthesis and Properties of Nanowires and Nanotubes. *Accounts of Chemical Research*, 32, 5 (May 1999), 435-445.

[145] Hafaiedh, A. and Bouarissa, N. Quantum Confinement Effects on Energy Gaps and Electron and Hole Effective Masses of Quantum Well AlN. *Physica E-Low-Dimensional Systems & Nanostructures*, 43, 9 (Jul 2011), 1638-1641.

[146] Yan, R., Gargas, D. and Yang, P. Nanowire Photonics. *Nature Photonics*, 3, 10 (Oct 2009), 569-576.

[147] Bronstrup, G., Jahr, N., Leiterer, C., Csaki, A., Fritzsche, W. and Christiansen, S. Optical Properties of Individual Silicon Nanowires for Photonic Devices. *Acs Nano*, 4, 12 (Dec 2010), 7113-7122.

[148] Cao, L. Y., Fan, P. Y., Barnard, E. S., Brown, A. M. and Brongersma, M. L. Tuning the Color of Silicon Nanostructures. *Nano Letters*, 10, 7 (Jul 2010), 2649-2654.

[149] Walker, B. N., Stolee, J. A., Pickel, D. L., Retterer, S. T. and Vertes, A. Tailored Silicon Nanopost Arrays for Resonant Nanophotonic Ion Production. *Journal of Physical Chemistry C*, 114, 11 (Mar 2010), 4835-4840.

[150] Seo, K., Wober, M., Steinvurzel, P., Schonbrun, E., Dan, Y., Ellenbogen, T. and Crozier, K. B. Multicolored Vertical Silicon Nanowires. *Nano Letters*, 11, 4 (Apr 2011), 1851-1856.

[151] Cao, L. Y., Park, J. S., Fan, P. Y., Clemens, B. and Brongersma, M. L. Resonant Germanium Nanoantenna Photodetectors. *Nano Letters*, 10, 4 (Apr 2010), 1229-1233.

[152] Muskens, O. L., Diedenhofen, S. L., Kaas, B. C., Algra, R. E., Bakkers, E., Rivas, J. G. and Lagendijk, A. Large Photonic Strength of Highly Tunable Resonant Nanowire Materials. *Nano Letters*, 9, 3 (Mar 2009), 930-934.

[153] Schmidt, V., Senz, S. and Gosele, U. Diameter-Dependent Growth Direction of Epitaxial Silicon Nanowires. *Nano Letters*, 5, 5 (May 2005), 931-935.

[154] Taraci, J. L., Dailey, J. W., Clement, T., Smith, D. J., Drucker, J. and Picraux, S. T. Nanopillar Growth Mode by Vapor-Liquid-Solid Epitaxy. *Applied Physics Letters*, 84, 26 (Jun 28 2004), 5302-5304.

[155] Ergen, O., Ruebusch, D. J., Fang, H., Rathore, A. A., Kapadia, R., Fan, Z., Takei, K., Jamshidi, A., Wu, M. and Javey, A. Shape-Controlled Synthesis of Single-Crystalline Nanopillar Arrays by Template-Assisted Vapor-Liquid-Solid Process. *Journal of the American Chemical Society*, 132, 40 (Oct 13 2010), 13972-13974.

[156] Wells, S. M., Polemi, A., Lavrik, N. V., Shuford, K. L. and Sepaniak, M. J. Efficient Disc on Pillar Substrates for Surface Enhanced Raman Spectroscopy. *Chemical Communications*, 47, 13 (2011 2011), 3814-3816.

[157] Polemi, A., Wells, S. M., Lavrik, N. V., Sepaniak, M. J. and Shuford, K. L. Local Field Enhancement of Pillar Nanosurfaces for SERS. *Journal of Physical Chemistry C*, 114, 42 (Oct 28 2010), 18096-18102.

[158] Blech, M. D. and Eibert, T. F. A Dipole Excited Ultrawideband Dielectric Rod Antenna with Reflector. *Ieee Transactions on Antennas and Propagation*, 55, 7 (Jul 2007), 1948-1954.

[159] Scordata, A. and Schwartz, S. *Triple Band Excitation: EAPI-FITC-TRITC*. Nikon Instruments, Inc., City, 2010.

[160] Howarter, J. A. and Youngblood, J. P. Optimization of Silica Silanization by 3-Aminopropyltriethoxysilane. *Langmuir*, 22, 26 2006), 11142-11147.

[161] Cao, L. Y., Nabet, B. and Spanier, J. E. Enhanced Raman Scattering from Individual Semiconductor Nanocones and Nanowires. *Physical Review Letters*, 96, 15 (Apr 21 2006).

[162] Luu, Q. N., Doorn, J. M., Berry, M. T., Jiang, C. Y., Lin, C. K. and May, P. S. Preparation and Optical Properties of Silver Nanowires and Silver-Nanowire Thin Films. *J. Colloid Interface Sci.*, 356, 1 (Apr 2011), 151-158.

[163] Shtoyko, T., Matveeva, E. G., Chang, I. F., Gryczynski, Z., Goldys, E. and Gryczynski, I. Enhanced Fluorescent Immunoassays on Silver Fractal-Like Structures. *Analytical Chemistry*, 80, 6 (Mar 15 2008), 1962-1966.

[164] Hossain, M. K., Huang, G. G., Kaneko, T. and Ozaki, Y. Characteristics of Surface-Enhanced Raman Scattering and Surface-Enhanced Fluorescence Using a Single and a Double Layer Gold Nanostructure. *Physical Chemistry Chemical Physics*, 11, 34 (2009 2009), 7484-7490.

[165] Medintz, I. L., Uyeda, H. T., Goldman, E. R. and Mattoussi, H. Quantum Dot Bioconjugates for Imaging, Labelling and Sensing. *Nature Materials*, 4, 6 (Jun 2005), 435-446.

[166] Howarth, M., Liu, W., Puthenveetil, S., Zheng, Y., Marshall, L. F., Schmidt, M. M., Wittrup, K. D., Bawendi, M. G. and Ting, A. Y. Monovalent, Reduced-Size Quantum Dots for Imaging Receptors on Living Cells. *Nature Methods*, 5, 5 (May 2008), 397-399.

[167] Xie, C., Hanson, L., Cui, Y. and Cui, B. Vertical nanopillars for highly localized fluorescence imaging. *Proceedings of the National Academy of Sciences of the United States of America*, 108, 10 (Mar 8 2011), 3894-3899.

[168] Aslan, K., Gryczynski, I., Malicka, J., Matveeva, E., Lakowicz, J. R. and Geddes, C. D. Metal-Enhanced Fluorescence: An Emerging Tool in Biotechnology. *Current Opinion in Biotechnology*, 16, 1 (Feb 2005), 55-62.

[169] Larmour, I. A. and Graham, D. Surface Enhanced Optical Spectroscopies for Bioanalysis. *Analyst*, 136, 19 (2011 2011), 3831-3853.

[170] Lavrik, N. V., Taylor, L. T. and Sepaniak, M. J. Nanotechnology and Chip Level Systems for Pressure Driven Liquid Chromatography and Emerging Analytical Separation Techniques: A Review. *Analytica Chimica Acta*, 694, 1-2 (May 23 2011), 6-20.

[171] Lakowicz, J. R., Geddes, C. D., Gryczynski, I., Malicka, J., Gryczynski, Z., Aslan, K., Lukomska, J., Matveeva, E., Zhang, J. A., Badugu, R. and Huang, J. Advances in Surface-Enhanced Fluorescence. *Journal of Fluorescence*, 14, 4 (Jul 2004), 425-441.

[172] Corrigan, T. D., Guo, S., Phaneuf, R. J. and Szmacinski, H. Enhanced Fluorescence from Periodic Arrays of Silver Nanoparticles. *Journal of Fluorescence*, 15, 5 (Sep 2005), 777-784.

[173] Geddes, C. D., Parfenov, A., Roll, D., Fang, J. Y. and Lakowicz, J. R. Electrochemical and Laser Deposition of Silver for Use in Metal-Enhanced Fluorescence. *Langmuir*, 19, 15 (Jul 22 2003), 6236-6241.

[174] Geddes, C. D., Parfenov, A., Roll, D., Gryezynski, I., Malicka, J. and Lakowicz, J. R. Roughened Silver Electrodes for Use in Metal-Enhanced Fluorescence. *Spectrochimica Acta Part a-Molecular and Biomolecular Spectroscopy*, 60, 8-9 (Jul 2004), 1977-1983.

[175] Matveeva, E., Gryczynski, Z., Malicka, J., Gryczynski, I. and Lakowicz, J. R. Metal-Enhanced Fluorescence Immunoassays Using Total Internal Reflection and Silver Island-Coated Surfaces. *Analytical Biochemistry*, 334, 2 (Nov 15 2004), 303-311.

[176] Fort, E. and Gresillon, S. Surface Enhanced Fluorescence. *Journal of Physics D-Applied Physics*, 41, 1 (Jan 7 2008).

[177] Ausman, L. K. and Schatz, G. C. Whispering-Gallery Mode Resonators: Surface Enhanced Raman Scattering Without Plasmons. *Journal of Chemical Physics*, 129, 5 (Aug 7 2008).

[178] Claps, R., Dimitropoulos, D., Han, Y. and Jalali, B. Observation of Raman Emission in Silicon Waveguides at 1.54 mu m. *Optics Express*, 10, 22 (Nov 04 2002), 1305-1313.

[179] Boyraz, O. and Jalali, B. Demonstration of a Silicon Raman Laser. *Optics Express*, 12, 21 (Oct 18 2004), 5269-5273.

[180] Rong, H. S., Jones, R., Liu, A. S., Cohen, O., Hak, D., Fang, A. and Paniccia, M. A Continuous-Wave Raman Silicon Laser. *Nature*, 433, 7027 (Feb 17 2005), 725-728.

Vita

Sabrina was born in Independence, Missouri in October, 1984. Her family stayed in the Kansas City area for the entirety of her childhood and still resides there. After graduating from Raytown High School in 2003, she went on to study Chemistry at Truman State University. After earning her bachelor's degree in 2007, Sabrina went to graduate school at the University of Tennessee- Knoxville to continue her education. Under the direction of Professor Michael Sepaniak, she will graduate with a Ph.D. in Analytical Chemistry in May, 2012.